Signal Processing Techniques for Landmine Detection Using Impulse Ground Penetrating Radar (ImGPR)

Vom Fachbereich 18
Elektrotechnik und Informationstechnik
der Technischen Universität Darmstadt
zur Erlangung der Würde eines
Doktor-Ingenieurs (Dr.-Ing.)
genehmigte Dissertation

von
Gebremichael Te-ame Tesfamariam, M.Sc.
geboren am 08.02.1978 in Enticho (Äthopien)

Referent:	Prof. Dr.-Ing. Abdelhak M. Zoubir
Korreferent:	Prof. Dr. Dilip S. Mali
Tag der Einreichung:	15.04.2013
Tag der mündlichen Prüfung:	15.07.2013

D 17
Darmstadt, 2013

Acknowledgments

I would like to thank all the people who have helped me during my doctoral study.

First of all, I would like to express my sincere gratitude to my supervisor, Prof. Dr.-Ing. Abdelhak Zoubir, for his invaluable guidance and continuous encouragement. I could not have imagined having a better supervisor and mentor for my PhD study who can show such a high degree of enthusiasm and motivation.

I wish to thank Prof. Dr. Dilip S. Mali for his supervision, guidance and support when I went back to Mekelle University, Ethiopia. I benefited greatly from our interactions, and I am delighted to have such a renowned researcher as my co-advisor.

I also want to thank Prof. Dr.-Ing Hans Eveking, Prof. Dr.-Ing. Rolf Jakoby and Prof. Dr.-Ing Harald Klingbeil, who acted as chair and examiners in the PhD committee.

I need to thank Engineering Capacity Building Program (ECBP) and Deutscher Akademischer Austausch Dienst (DAAD) for financing and managing my scholarship.

I would like to thank my colleagues at the Signal Processing Group at TU Darmstadt. I treasure my memories of those joyous days. Thanks to Sara Al-Sayed, Mouhammad Alhumaidi, Nevine Demitri, Michael Fauss, Gökhan Gül, Jürgen Hahn, Sahar Khawatmi, Stefan Leier, Michael Leigsnering, Michael Muma, Wassim Suleiman, Fiky Suratman, Christian Weiss, Feng Yin, Michael Lang, and Tim Schäck, as well as Renate Koschella and Hauke Fath. I would also like to thank the former PhD students Raquel Fandos, Christian Debes, Weaam Alkhaldi, Marco Moebus, Uli Hammes, Yacine Chakhchoukh, Waqas Sharif, Ahmed Mostafa, Philipp Heidenreich, and Zhihua Lu.

A special thanks is due to everybody at Mekelle University and Ethiopian Institute of Technology for fruitful discussions and great hospitality. Thanks to Dr. Gebremeskel, Dr.-Tech Medhanye, Dr. Tensay, Alem, Zenachew, Girmay, Helen and Maernet.

I wish to thank my parents Te-ame and Kebedech, sisters Tifto, Almaz, Azeb and Helen, brothers Ghedamu, Welday, Gebrekidan and Ambaye for their unconditional love and support throughout my life. I would also like to thank my friends, Rafi, Getachew, Dr.-Ing Teklay, Dr.-Ing Yoseph, Mustefa, Amanuel and Selamawit.

Finally, I am most grateful to my wife Werki, my sons Nahom and Yohann for their understanding, love, encouragement, support and joy.

Darmstadt, 30.07.2013

Kurzfassung

Landminen und Blindgänger (UXO) werden während eines militärischen Konflikts gegen feindliche Kräfte vergraben. Allerdings töten oder verstümmeln sie Zivilisten Jahrzehnte nachdem der Konflikt beendet ist. Es gibt mehr als 110 Millionen aktive Landminen, die in der ganzen Welt verteilt sind. Jedes Jahr werden mehr als 26.000 unschuldige Zivilisten getötet oder verstümmelt. Die meisten modernen Landminen sind hauptsächlich nichtmetallisch bzw. aus Kunststoff, was eine Detektion mit herkömmlichen Metalldetektoren erschwert. Detektion mit in der Hand gehalten Stäben ist ein langsamer und teurer Prozess. Impuls Bodenradar (ImGPR) ist eine nicht-explosive Methode zum Aufspüren von flach begraben nichtmetallischen Anti-Personenminen (AP) und Anti-Panzer (AT) Landminen. In dieser Doktorarbeit wird ImGPR als ein Werkzeug betrachtet, um Landminen und Blindgänger zu erkennen. Das Vorhandensein starker Bodenechos und Rauschen, verringern die Leistung von GPR Geräten. Daher ist eine GPR-Sensor Benutzung fast unmöglich, ohne die Anwendung von geeigneter Signalverarbeitung.

In dieser Arbeit wird die Übertragung elektromagnetischer Wellen modelliert durch eine mehrschichtige Übertragungsleitung. Dieses Modell beinhaltet verschiedene Bodenarten mit unterschiedlicher Feuchtigkeit. Kunststoff Ziele unterschiedlichen Durchmessers werden in unterschiedlichen Tiefen vergraben. Das modellierte Signal wird dann verwendet, um die Parameter des Bodens und des vergrabenen Zieles zu schätzen. Zur Parameterschätzung wird die Oberflächenreflexion-Parameter-Methode (SRPM) angewandt.

Signalverarbeitungsmethoden zur Bodenechounterdrückung und Entscheidungsfindung wurden implementiert. Es wurde vor allem auf die Entwicklung von Techniken Wert gelegt, die für Echtzeit-Landminendetektion geeignet sind. Fortgeschrittene Methoden werden durch elementare Vorverarbeitungstechniken unterstützt, die nützlich für die Signal-Korrektur und Rauschreduzierung sind. Hintergrundsubtraktionstechniken, basierend auf Multilayer-Modellierung, räumliche Filterung und adaptive Hintergrundsubtraktion wurden implementiert. Außerdem wurden Dekorrelation und Symmetrie Filtertechniken behandelt.

In der korrelierten Entscheidungsfusion werden lokale Entscheidungen zum Fusionszentrum übertragen, um eine globale Entscheidung zu treffen. In diesem Fall ist das Konzept der Vertrauensinformationen der lokalen Entscheidungen entscheidend um annehmbare Ergebnisse zu erhalten. Die Bahadur-Lazarfeld und Chow Erweiterungen

werden verwendet, um die gemeinsamen Wahrscheinlichkeitsdichtefunktion der korrelierten Entscheidungen zu schätzen. Ebenfalls wurde Fuzzy-Set-basierte Entscheidungsfusion implementiert.

Alle vorgeschlagenen Methoden wurden sowohl mit simulierten als auch mit echt gemessenen GPR Daten in vielen Szenarien evaluiert. Die Datenerhebungskampagne wurde in Griesheim am alten Flughafen und im Botanischen Garten, Darmstadt, Deutschland im Juli 2011, durchgeführt.

Abstract

Landmines and unexploded ordinance (UXO) are laid during a conflict against enemy forces. However, they kill or maim civilians decades after the conflict has ended. There are more than 110 million landmines actively lodged in the globe. Every year more than 26,000 innocent civilians are killed or maimed. Most modern landmines are mainly nonmetallic or plastic, which are difficult to be detected using conventional metal detectors. Detection using hand-held prodding is a slow and expensive process. Impulse Ground Penetrating Radar (ImGPR) is a nondestructive technique capable of detecting shallowly buried nonmetallic anti-personnel (AP) and anti-tank (AT) landmines. In this PhD thesis, ImGPR is considered as a tool to detect landmines and UXO. The presence of strong ground clutter and noise degrade the performance of GPR. Hence, using a GPR sensor is almost impossible without the application of sophisticated signal processing.

In electromagnetic wave propagation modeling, a multilayer transmission line technique is applied. It considers different soil types at different moisture levels. Plastic targets of different diameters are buried at different depths. The modeled signal is then used to estimate the ground and buried target parameters. In a parameter estimation procedure, a surface reflection parameter method (SRPM) is applied.

Signal processing algorithms are implemented for clutter reduction and decision making purposes. Attention is mainly given to the development of techniques, that are applicable to real-time landmine detection. Advanced techniques are preceded by elementary preprocessing techniques, which are useful for signal correction and noise reduction. Background subtraction techniques based on multilayer modeling, spatial filtering and adaptive background subtraction are implemented. In addition to that, decorrelation and symmetry filtering techniques are also investigated.

In the correlated decision fusion framework, local decisions are transmitted to the fusion center so as to compute a global decision. In this case, the concept of confidence information of local decisions is crucial to obtain acceptable detection results. The Bahadur-Lazarsfeld and Chow expansions are used to estimate the joint probability density function of the correlated decisions. Furthermore, a decision fusion based on fuzzy set is implemented.

All proposed methods are evaluated using simulated as well as real GPR data measurements of many scenarios. The real data collection campaign took place at the Griesheim old airport and Botanischer Garten, Darmstadt, Germany in July 2011.

Contents

Chapter 1
Introduction and Motivation

1.1 Introduction

Landmines and unexplored ordinance (UXO) emplaced during a conflict against enemy forces can still kill or injure civilians decades after the war has ended [1–4]. Landmines are weapons that indiscriminately kill or maim whoever triggers them, whether a child, a woman or a soldier. Mines can be found anywhere: in fields, along rivers, in urban areas, on transport routes and in surrounding villages [5–7]. Globally, more than 110 million landmines are actively lodged in nearly 70 countries. The casualty rates are correspondingly very high. Every week more than 500 innocent civilians are killed or maimed and about 26,000 every year [8, 9]. Moreover, landmine casualties, threats and rumors are humanitarian challenges that hinder humanitarian mobility and economic development [5, 6, 8–13].

Ground penetrating radar (GPR) is an emerging technology that provides centimeter resolution to locate even targets that are too small [9]. It is an electromagnetic technique that is designed primarily to investigate roads, bridges and subsurface objects. In the last three decades, impulse GPR (ImGPR) has been considered as a viable technology for the detection of buried landmines without affecting the environment where the targets are. GPR senses electrical inhomogeneities caused by dielectrics of buried objects in the presence of less-conducting ground soil [14, 15].

Modern landmines are mainly plastic or less metallic that the dielectric contrast between the landmine and the background is very weak. The existence of large contrast between the air and the soil medium causes a strong bounce that returns from the interface which usually obscures the weak signature caused by the buried plastic landmine [10, 16, 17].

The signal reflected from buried plastic landmines is subjected to strong background clutter, noise and distortions. Hence, one of the main challenges of using GPR for landmine detection is to remove the ground bounce as completely as possible without altering the landmine return. Model-based online signal processing algorithms for clutter reduction and target discrimination are important in this area.

The aim of this thesis is to develop signal processing algorithms for clutter reduction and landmine detection, and schemes to fuse the decisions made by the signal processing

detectors. The techniques should be able to adapt to the changes in environmental conditions such as surface roughness, soil inhomogeneities and presence of high moisture level.

1.2 Motivation

Because of many internal conflicts and international wars, landmines have been laid against enemy soldiers. Contamination by landmines and UXO is a global problem with an enormous humanitarian impact. In 1997, the Convention of Ottawa Treaty on the Prohibition of the Use, Stockpiling, Production and Transfer of Anti-Personnel Mines and on Their Destruction, was signed and entered into force in 1999. The Treaty mandating that all stockpiles of mines should be destroyed within 4 years and all minefields lifted in 10 years [4, 7, 15, 18].

Despite the political willingness of the world community to end the suffering and landmine casualties in a short term, the situation on the ground is not changing fast. This is due to the limited performance of the detection technologies available for operational deminers, like prodding sticks, animals, and electromagnetic induction (EMI). The use of these demining technologies results in a high number of false alarms and missing rates. Hence, the humanitarian demining process is slow, expensive and dangerous, without using reliable high-tech tools [17]. New technologies with sophisticated sensors and signal processing could assist deminers so as to achieve faster and reliable demining.

In the last three decades, a lot of attention has been paid to the application of GPR as viable landmine and UXO sensor. GPR allows detection of shallowly buried, less-metallic antipersonnel (AP) and antitank (AT) mines. However, GPR also performs inadequately due to the presence of strong clutter [14,15,19,20]. Clutter arises from the strong air-ground interface, measurement and process noise, and direct communication between transmitter and receiver antennas [16,21]. Signal processing techniques play a great role in reducing the clutter and improving the probability of detection of mines.

Performance of different signal processing techniques depends on the type of the buried target, type of the soil environment and the amount of moisture level of the soil [9, 15]. There is no universal signal processing technique that performs the best in all scenarios. Fusion of the decisions made by the signal processing algorithms improves the performance of GPR by increasing the detection probability of GPR and reducing the false alarm rate greatly.

1.3 State-of-the-Art

Landmine detection is a cross-disciplinary research in electromagnetic propagation [22–24], antenna and waveform design ([25, 26] and references therein), clutter reduction ([9, 27–31] and references therein), target identification and classification [28, 32], multi-sensor fusion [33–36], multi-expert data fusion [37,38], and sensor technology [15] among others.

Most contributions in landmine detection are based on the use of metal detectors, prodding sticks and dogs [9, 15]. Some contributions in this area deal with the use of only GPR where online and offline clutter reduction techniques are applied. Others deal with the use of many sensors, such as GPR, EMI and IR, where multi-sensor fusion is applied [15, 33–36]. To the best of our knowledge there is no contribution, except [39], that uses a single GPR sensor and employs many experts to reduce clutter, and implements fusion of decisions made by the experts.

There are few contributions in model-based clutter reduction, such as polynomial phase [5] and ARMA model based deconvolution [31, 40]. However, to the best of our knowledge, there is no contribution on inverse multilayer target and subsurface parameter estimation except in [41].

The presence of clutter makes GPR-based landmine detection difficult. Most contributions in this area deal with clutter reduction techniques. Commonly used clutter reduction techniques are based on background subtraction ([9, 27, 28, 40, 42, 43] and their references therein), Kalman filtering [9, 29, 41, 44], wavelet packet decomposition [9,45–47], time-frequency analysis [48–51], independent component analysis [52,53] and particle filtering [54]. To the best of our knowledge, the contributions besides ours are that by Li *et al.* who applied symmetry filtering in the presence of a single target [55], and Park *et al.* who applied offline symmetry filtering for the discrimination of landmines from mine-like targets [56]. Only [25] and our contribution [41] have used adaptive background techniques and to the best of our knowledge no one has considered reverse multi-layer modeling based background subtraction techniques.

In decision fusion applications, Zayda *et al.* [37] and Kovalenko *et al.* [38] used polarimetric data fusion as applied to GPR based landmine detection. To the best of our knowledge, there is no contribution except [39] which deals with the fusion of correlated local decision where a single sensor and many signal processing algorithms are employed.

1.4 Contributions

- **Electromagnetic Propagation Modeling:** An electromagnetic wave propagation modeling of GPR, based on a time-domain transmission line (TL) approach, is developed. A TL multilayer modeling principle that suits plastic landmine detection is designed. The model considers each subsurface and buried landmines as layers with different electrical properties. Different types of landmines buried in different soil types and with varying moisture levels are considered in the course of the modeling process.

- **Subsurface and target parameter estimation:** Estimation of subsurface and target parameters, such as the reflection coefficient of an interface, intrinsic impedance and relative permittivity of each layer are tackled. A reverse multilayer modeling and surface reflection parameter methods (SPRM) are used for the estimation of the parameters. A two-layer inverse model is assumed, where the first layer corresponds to the ground surface and the second layer to the buried target.

- **Advanced Signal Processing:** On-line, causal, real-time and adaptive signal processing techniques are developed. By using these techniques, clutter components are suppressed and target components are enhanced. Most existing techniques use offline and noncausal processing techniques.

    1. Moving window background estimation techniques are applied for background subtraction applications. These techniques are also used as a reference to advanced techniques. In addition to moving window, multilayer model based background modeling is also applied. Moreover, an adaptive background subtraction method, which adapts to changes in the soil roughness and inhomogeneity, is also tackled. The estimation begins with some target free measurements and modifications are introduced to dynamically adjust to environmental changes.
    2. A symmetry filtering approach, which classifies targets and non-target clutter based on their geometry, is developed. The method assumes that AP and AT have symmetrical geometry and a symmetry difference is employed to classify mines and mine-like objects. Besides, decorrelation based on Karhunen-Loéve transform (KLT) and subtract and weight (SaW) of the residue of the measured data and arbitrary ground signal by its variance is proposed.

- **Decision Fusion:** A decision fusion framework, which fuses the correlated local decisions, is implemented. Two of the techniques are based on Bahadur-

Lazarsfeld and Chow expansions, and they require knowledge of the prior probabilities of the local decision makers. However, the third technique is based on the fuzzy set and does not require the knowledge of the prior probabilities. The proposed correlated decision fusion techniques are compared with classical fusion techniques.

1.5 Publications

The following publications have been produced during the period of PhD candidacy.

Internationally Refereed Journal Articles

- Gebremichael T. Tesfamariam, Dilip S. Mali. Review of GPR Technologies for Landmine Detection, International Journal of Computing and Communication Technologies, vol. 5, No. 1, July 2012, ISSN 0974-3375
- Gebremichael T. Tesfamariam, Abdelhak M. Zoubir, Multilayer modeling based detection of buried landmine using Ground Penetrating radar, IEEE Sensors Journal, submitted

Internationally Refereed Conference Articles

- Gebremichael T. Tesfamariam, Dilip S. Mali, Abdelhak M. Zoubir, Clutter reduction techniques for GPR based landmine detection, IEEE Proceedings of International Conference on Signal Processing, Communication, Computing and Networking technologies (ICSCCN), CN.2011.6024540, 2011.
- Gebremichael T. Tesfamariam, Dilip S. Mali, Abdelhak M. Zoubir, Fusion of correlated local decisions for GPR based landmine detection, IEEE Proceedings of 14th International Conference on Ground Penetrating Radar (GPR2012), DOI: 10.1109/ICGPR.2012.6254983, 2012.
- Gebremichael T. Tesfamariam, Abdelhak M.Zoubir, Proceedings of 7th Radar Conference, Advanced background subtraction techniques for GPR based landmine detection, accepted, April, 2013

1.6 Thesis Outline

This thesis is written as a partial fulfillment of the requirements for the degree of Doctor Engineer (Dr.-Ing). The broad objective of this research was to study, develop and compare signal processing techniques so as to improve the detectability of buried AP and AT landmines using impulse ground penetrating radar (ImGPR).

The thesis is organized in seven chapters and its outline is as follows:

Chapter 2 of this thesis provides a background on landmines and detection technologies. The nature, casualty rate, types, spread and environments where landmine can be found are discussed in detail. Moreover, the GPR system that has been used to collect the measured data in this thesis is presented. Technologies, that are currently being used for landmine detection applications are also covered.

Chapter 3 is concerned with the electromagnetic propagation modeling of GPR based on a transmission line (TL) approach. The electromagnetic propagation in dielectric media, the analogy of the subsurface ground with TL and techniques to generate synthetic data are also addressed.

Chapter 4 deals with parameter estimation techniques based on reverse multilayer modeling. Subsurface parameters, such as interface reflection coefficients, intrinsic impedance and relative permittivity of each layer, are estimated using measurements of the reflected electric fields from each layer.

Chapter 5 presents advanced signal processing techniques applied to GPR data. A number of detection methods, that are currently being used with GPR are summarized. Moreover, new advanced signal processing techniques, such as adaptive and model based background subtraction, subtract and weight method, KLT based decorrelation and symmetry filtering are proposed.

Chapter 6 covers the topics related to correlated decision fusion using optimal fusion techniques and fuzzy set based fusion strategies. These techniques are compared with classical decision fusion and majority voting techniques.

Chapter 7 draws conclusions and gives future directions in this research area.

Chapter 2

Landmines and Detection Technologies

In this chapter, the background problem of landmines and landmine detection technologies will be discussed. Next, the nature, the distribution and the casualty rates of landmines will be covered. Moreover, we will present the feasibility and the current status of the mine detection technologies. Further more, we will compare mine detection technologies in terms of maturity, cost and complexity. Finally, we will present the working principles of GPR and its application to landmine detection.

2.1 Landmines and Humanitarian Problems

Landmines are used for warfare to deny enemy forces from accessing some areas. However, they have a very long life-span, that they remain active after the war has ended [5, 7]. Each day, these mines are triggered accidentally by civilian activities. Consequently, they ravage the land and kill or maim innocent civilians. Minefields can be found everywhere like on agricultural fields, transport routes, urban areas, rivers and surrounding villages [16].

2.1.1 Some Properties of Landmines

Landmines are usually simple devices, readily manufactured anywhere, easy to lay and yet so difficult to detect. Landmines, since the First World War, have proved to be an effective and cheap military weapons. They have been used in many war zones to deny access to roads, bridges, water sources, trenches and other strategic areas. They are also used to deflect, delay or destroy enemy forces [5, 7]. Modern wars are often characterized by the widespread use of landmines [57]. As a result, there are more than 110 million landmines in nearly 70 countries all over the world [9, 12]. One-fourth of these mines are found in Afghanistan, Iraq, Croatia, Egypt, Cambodia, Angola and Mozambique [15, 57].

There are two classes of landmines: anti-personnel (AP) mines and anti-tank (AT) mines. The functions of both forms of these landmines are to disable and kill. AP mines are munitions designed to explode from the proximity or contact of a person.

AT mines are typically larger in size and contain more explosive material than AP mines. AT mines are munitions designed to immobilize or destroy military or civilian vehicles and their occupants. They explode from the proximity or contact of a vehicle as opposed to a person [1–3, 10].

All kinds of mines consist of an explosive, detonator, spring, casing and void [15]. In general, explosives are composed of Carbon (C), Hydrogen (H), Nitrogen (N), Oxygen (O) and many other organic compounds. The explosive materials for AT mines are usually trinitrotoluene (TNT), cyclotrimethylenenitramine (royal demolition explosive (RDX)) and composition-B (Comp B). However, TNT, Tetryl and Comp B are the common explosives in AP mines [7]. The firing pin and the spring typically contains several metal parts, but there are exceptions with no metal parts at all. The low metal cases, in which the firing pin contains 5 g metal and can be as low as 2 g [17, 20, 21].

Landmines come in different shapes and sizes. Most mines have a shape of cylinders or box-like with dimensions: for AT mines, diameter 150 to 350 mm and thickness 50 to 90 mm and for AP mines, diameter 55 to 150 mm and thickness 50 to 100 mm [7, 15]. They can be encased in wood, sheet metal, ceramic, glass, plastic or nothing at all [7, 18].

Landmines come with different kinds of fusing mechanisms. Many of them are pressure triggered, trip wired or tilt rods. However, there are also seismically or magnetically influenced fuses [7,10,15,18,20,57]. AP mines can detonate with a pressure as small as 6 kg but, AT mines need more than 100 kg to detonate [11, 13]. The burial depth has a relationship with the triggering pressure, for example, AT mines are usually buried at a depth between 15 cm and 30 cm. AP mines can be laid on the surface or buried flush at a maximum depth of 10 cm [7, 10, 13].

Landmines are cheap to produce and to lay. A single AP mine costs 3 USD and an AT mine costs up to 75 USD. They can be laid quickly in a great quantity by low skilled personnel. In contrast, removal must be done by highly skilled personnel and costs, on average, 300 USD to 500 USD for a single mine [7, 20, 21, 57]. Even with highly trained deminers, UN statistics indicate a loss of one or two deminers per 1000 mines removed [12, 57]. As an example, Nicaragua cleared almost 12 sq. km of mined areas, destroying in the process almost 180,000 mines at an estimated total cost of 82 million USD, an average of 455.6 USD per mine [3].

2.1.2 Landmine Contamination and Effects

Landmines can be found everywhere either buried flush in the ground or laid on the surface. They may be emplaced by soldiers, thrown by vehicles, helicopters or lowly flying planes in an ordered or disordered manner [5, 7, 10, 15, 16, 18, 20]. Mines are encountered in a variety of environmental conditions. For example, in desert regions (Somalia, Kuwait, Egypt), mountains (Afghanistan, El Salvador), jungles (Cambodia, Vietnam) as well as urban areas (Beirut, Former Yugoslavia) [10, 16]. They can be embedded in a field cluttered with various materials and objects, buried underground at various depths, scattered on the surface, planted within buildings, or covered by plant overgrowth [5, 7, 10, 16].

Contamination by landmines and all other types of UXO is a worldwide problem with enormous humanitarian impact [5,17]. Landmines are victim activated weapons, which indiscriminately kill or maim a civilian or a soldier [1–4]. The number of casualties are also high, more than 500 innocent civilians killed or maimed weekly [7, 9, 11, 13, 16, 21]. It is found that one in three victims die according to a survey done in Afghanistan, Mozambique, Bosnia and Cambodia [15].

Many social and economic problems arise due to the presence of landmines. Arable land is rendered unusable, trade routes become closed, communities and villages are isolated and families are forced to separate [1,5]. As an example, there were five to ten market places used by the nearby dwellers living around the border villages of Eritrea and Ethiopia. After the border war broke out in 1998, the market places were totally closed and the villages close to the border were abandoned due to the rumors and the threat of landmines laid during the two-year long war.

To put it in a nutshell, mine detection equipment has to be designed to work in a wide range of physical environments and climatic conditions which range from arid desert, hillside scree to overgrown jungles. Ambient operating temperatures can range from -20 °C to 60 °C [10, 16]. Rain, dust and humidity must be considered in the design and operation of the equipment.

2.2 Demining Techniques

2.2.1 Demining

Demining is the process of removing either landmines or naval mines from an area [6]. Minefields and other areas contaminated with explosives have been treated as one of

Very heavy contamination ($> 100\ km^2$)	Heavy contamination ($10-100\ km^2$)
Country	Country
Afghanistan	Algeria
Angola	Colombia
Bosnia & Herzegovina	Chile
Cambodia	Democratic Republic of Congo
Chad	Egypt
Croatia	Eritrea
Iran	Lao PDR
Iraq	Libya
Western Sahara	Mauritania
Thailand	Mozambique
Turkey	Myanmar
	Russia
	Somalia
	South Sudan
	Sudan
	Sri Lanka
	Vietnam
	Yemen
	Zimbabwe

Table 2.1. Estimated extent of mine contamination (in km^2) in highly affected states as of October 2012 [4].

the consequences of war left to the host nation to resolve. Landmines and explosive remnants of war (ERW), which include UXO and abandoned explosive ordnance, represent a major threat to civilians [6, 13, 20]. To help stop destruction of the environment and threat of humanity, researchers must develop effective and optimized demining devices.

The goal of humanitarian demining is to clear all mines and UXO that affect the places and lives of people. The safety of the people living in these areas must be guaranteed [13]. Therefore, it demands a complete return of the land for civilian use (construction or agriculture). Humanitarian demining, hence, demands a destruction rate of nearly perfection: UN specifications require a clearance rate better than 99.6% [26].

The military programs are, in contrast, largely based on the requirement of maintaining the pace of military operations and clearing a path for crossing, typically one vehicle wide. Therefore, it has different requirements in terms of speed and detection performance compared to civil or humanitarian programs [10, 13, 16, 18, 58]. Military demining usually requires mine destruction rates of 70 - 80% [13].

2.2.2 Landmine Detection Technologies

According to the Ottawa Treaty, all stockpiles of mines should be destroyed within 4 years and all minefields lifted in 10 years [1–3,7,15,17]. However, the demining process is very slow because of limited performance of the detection devices for operational deminers. The most commonly used detection devices include prodding sticks, animals, and metal detectors (MD) [17,18,57].

Being the most sophisticated demining tool until recent times, the metal detector suffers from problems such as insufficient penetration depth and high false-alarm rate. Traditional demining technologies were the best demining tools for military applications. However, they could not guarantee humanitarian demining due to the requirement of the high clearance rate. In order to assist deminers and facilitate the demining process, a range of advanced sensor technologies are being investigated and tested. These technologies include:

1. Metal Detectors (MD): Measure the disturbance of an emitted electromagnetic field caused by the presence of metallic objects in the soil. MD is capable of detecting even low-metal content mines in mineralized soils [7,9,18,20]. However, MDs cannot differentiate a mine or UXO from other debris, which leads to false alarms: 100 - 1000 false alarms for each real mine detected [18]. MD is a matured technology, but cannot detect plastic or nonmetallic landmines, although most modern landmines have no metallic content except the striker pin. Increasing the sensitivity of detecting small metallic objects makes it susceptible to high false alarm rates [7,20].

2. Thermal Imaging (TI): Mines retain or release heat at a rate different from their surroundings. Infrared (IR) cameras create images that reveal the thermal contrast between the soil immediately surrounding a buried mine and the top layer of the soil [9]. If the contrast is from a mine, it shows a volume effect, however, if the contrast is due to disturbed soil, it shows a surface effect [18]. TI requires highly sensitive IR cameras and the detection depends on the environmental conditions [9,20].

3. Biological: Trained dogs, rats, pigs, bees and birds can smell the explosive within the mines. Dogs can reliably detect 10^{-12} to 10^{-13} g of explosives [18]. Even though they detect small explosives, they are hindered by inclement weather, terrain, tiredness and health issues. Moreover, they do not detect the actual location of the mine [9,15,20].

4. Nuclear Quadrupole Resonance (NQR): Induces radio frequency pulses that cause the chemical bonds in explosives to resonate [15]. The detection is limited to TNT, liquid explosives, radio frequency interference, quartz-bearing and magnetic soils.

5. Electrochemical: Confirms the presence of explosives by measuring the changes in polymer electrical resistance upon exposure to explosive vapors and works well in dry environments [15].

6. Piezoelectric: Measures shift in resonant frequency of various materials upon exposure to explosive vapors. This technique also confirms the presence of explosives and works well in dry environments [15].

7. Chemical Sensors: Sensors such as thermal fluorescence and chromatographic techniques detect airborne and water borne presence of explosive vapors [9].

8. Ground Penetrating Radar: GPR is a matured technology, which has been used in civil engineering, geology and archeology since 1970s. GPR detects the dielectric contrasts in the soil that allows to locate even nonmetallic mines. This ultra-wide band (UWB) radar provides centimeter resolution to locate even a small target [9]. GPR has rapid survey capability and near-real time data interpretation in many cases. Unfortunately, this technology can suffer from false alarms as high as that of metal detectors [10, 15, 18, 20, 59].

The demining technologies can also be compared in terms of the maturity of the technology, cost and complexity to produce and use. Table 2.2 summarizes the comparison of the sensor technologies discussed above.

Sensor technology	Maturity	Cost & complexity
Prodding sticks	Available	Low
Metal detector	Near	Low
Thermal Imaging	Far	High
Biological(Dogs)	Available	Medium
Nuclear Quadrapole Resonance	Far	High
Chemical sensors	Mid	High
Piezoelectric	Far	High
GPR	Near	Medium

Table 2.2. Comparison of demining technologies based on maturity, cost and complexity [18].

2.3 GPR Antenna System Overview

GPR is one of the technologies that has been extensively researched as a means of improving mine detection efficiency. In this section, we will provide background and the working principles of GPR as applied to civilian landmine detection programs.

GPR is a remote sensing geophysical method that operates in a wide frequency range. It works by detecting discontinuities of the dielectric properties of the subsurface [17]. Data are collected continuously as the system moves over the ground surface. Radar pulses are transmitted downward from an antenna and are reflected back from the subsurface. The reflected signals reach at a receiver and create a continuous graphic profile of the subsurface. Reflection of radar waves occur at interfaces having contrasting electrical properties. The time elapsed by the pulse to return to the antenna system relates to the depth at which the energy was reflected [16]. Thus, interpretation of this reflected energy yields information on the structural variation of the near subsurface.

GPR transmitting antennas operate in the Megahertz range and the waves that propagate tend to have wavelengths on the order of 1.0 m or less. Horizontal and vertical resolution are dependent upon the wavelength, such that the smaller the wavelength, the better the resolution. Although higher frequency sources will yield smaller wavelengths (better resolution), the higher frequency signals will not penetrate as deep as lower frequencies. Thus, a careful choice must be made regarding the GPR antennas to use in a survey based on expected target and the project goals. Once a source antenna is chosen for a particular survey, GPR data can be collected rapidly.

There are two distinct types of GPR: time-domain and frequency-domain. Time-domain or impulse GPR transmits discrete pulses of nanosecond duration and digitizes the returns at GHz sample rates. The time domain radars are relatively simple, cheap and robust. The weak points of the time-domain approach are a low signal-to-noise ratio (SNR) and typically low accuracy of the measured data. The frequency domain GPR system transmits single frequency either uniquely, as a series of frequency steps, or as a chirp [9, 25]. The amplitude and phase of the return signal is measured and the resulting data can be converted to the time domain. The frequency domain has a higher SNR due to a higher and more uniform spectral density of the radiated signal [25]. It allows to use a much larger frequency bandwidth than the time-domain approach. On the other hand, the frequency-domain approach requires more bulky and more expensive equipment and a larger measurement time.

A GPR system primarily consists of a data collection unit, transmitting antenna and receiving antenna as shown in Figure 2.1. If the same antenna functions as a transmit-

ter and receiver, the system is called mono-static, otherwise bi-static. GPR systems having both antennas combined in a single housing represents the bi-static system. The separation of the two antennas is often fixed and the survey method using this system is referred to as common offset method [60].

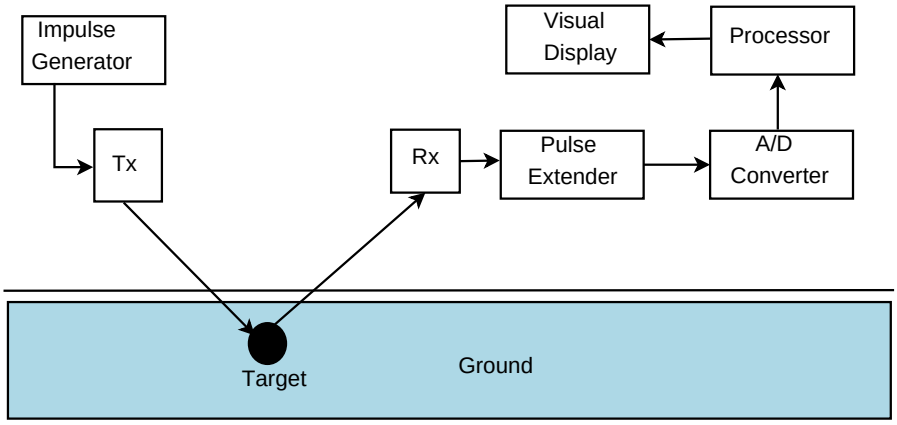

Figure 2.1. Typical GPR system block diagram [9, 43].

GPR systems are either ground-coupled or air-coupled. Ground-coupled antennas are placed directly on the ground surface and then dragged over it. Air-coupled antennas are often mounted on a specially designed cart or vehicle that drives it over the ground. Since the signal from the ground-coupled antenna does not travel through air, the majority of the energy from the antenna is transmitted into the target. This results in more visible subsurface features than the air-coupled system. However, for landmine detection applications, ground-coupled systems are not possible since surface laid landmines can explode though proximity or contact [21].

2.3.1 GPR Data Presentation Types

Based on the surveying dimensions, GPR data can be represented in three different forms: A-scan, B-scan and C-scan.

A-scan is a one-dimensional plot and also called a trace. It is a sequence of sample points collected by the GPR at a fixed antenna position that indicates a time variation of the recorded signal amplitude [16, 21, 27]. The time is related to the depth by propagation velocity through the medium. An A-scan can be represented in the following form:

$$g(t) = D(x_i, y_j, t_k), \text{ where } i = j = \text{constant}, \ 1 \leq k \leq N \tag{2.1}$$

B-scan is a two-dimensional plot representing an ensemble of A-scans as GPR moves in a straight line above the ground surface. The horizontal axis represents the scan length or number of traces, whereas the vertical axis represents the range or the time elapsed for the pulse to return, as shown in Figure 2.2.

$$g(x,t) = D(x_i, y_j, t_k), \text{ where } 1 \leq i \leq P,\ j = \text{constant} \text{ and } 1 \leq k \leq N \tag{2.2}$$

or

$$g(y,t) = D(x_i, y_j, t_k), \text{ where } i = \text{constant} \ , 1 \leq j \leq M \text{ and } 1 \leq k \leq N \tag{2.3}$$

C-scan is a three-dimensional display of GPR data resulting from the side-by-side arrangement of stacked B-scans. It is also represented by a collection of horizontal slices where each slice corresponds to a particular depth or a certain sample point, as shown in Figure 2.3 and Figure 2.4.

$$g(x,y,t) = D(x_i, y_j, t_k), \text{ where } 1 \leq i \leq P,\ 1 \leq j \leq M \text{ and } 1 \leq k \leq N \tag{2.4}$$

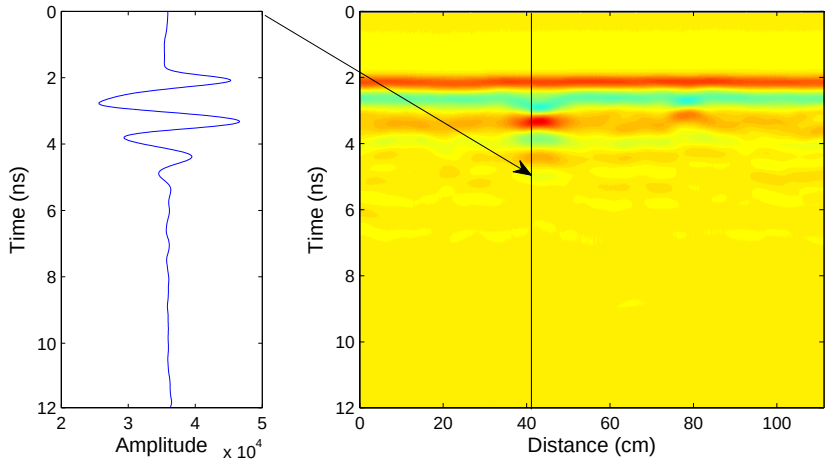

Figure 2.2. Representation of an A-scan and a radargram or B-scan.

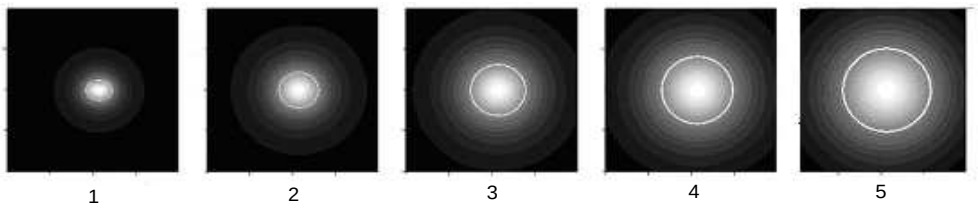

Figure 2.3. Representation of C-scan and numbers indicating orders towards the depth.

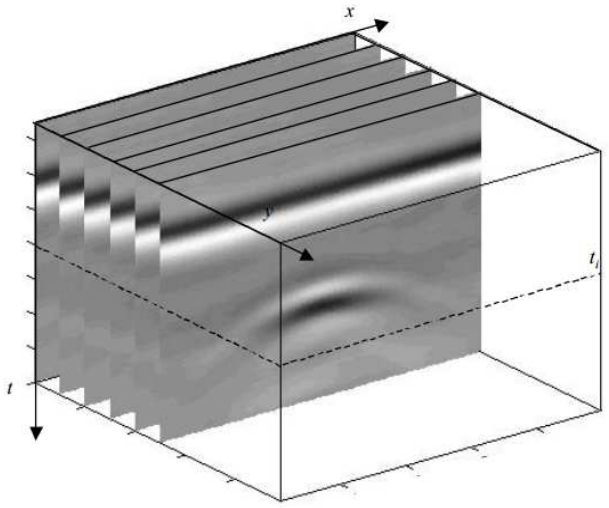

Figure 2.4. Multiple parallel B-scans forming a C-scan.

2.3.2 GPR Surveying Methods

GPR has four surveying modes depending on how the transmitter and receiver antenna moves and the spacing between the antenna set during the survey. These are common source, common offset, common depth and common receiver. Figure 2.5. shows the four common survey modes of GPR.

1. Common source: the transmitter is fixed, however, the receiver moves along the survey direction.
2. Common offset: both antennas move together in the direction of survey with a fixed offset or spacing between the units.
3. Common depth or common point: both, the transmitter and receiver antenna, move away from a common point in opposite direction.
4. Common receiver: the receiver is fixed, while the transmitter moves along the survey direction.

The most common and widely used form of GPR surveying mode deploys a transmitter and a receiver in a fixed geometry (common offset), where the antenna set moves over the surface [16, 17, 60]. With this measurement mode, one can efficiently and quickly obtain information about the near-surface underground structure. The common depth, common source and common receiver survey modes require different signal processing techniques to interpret the data.

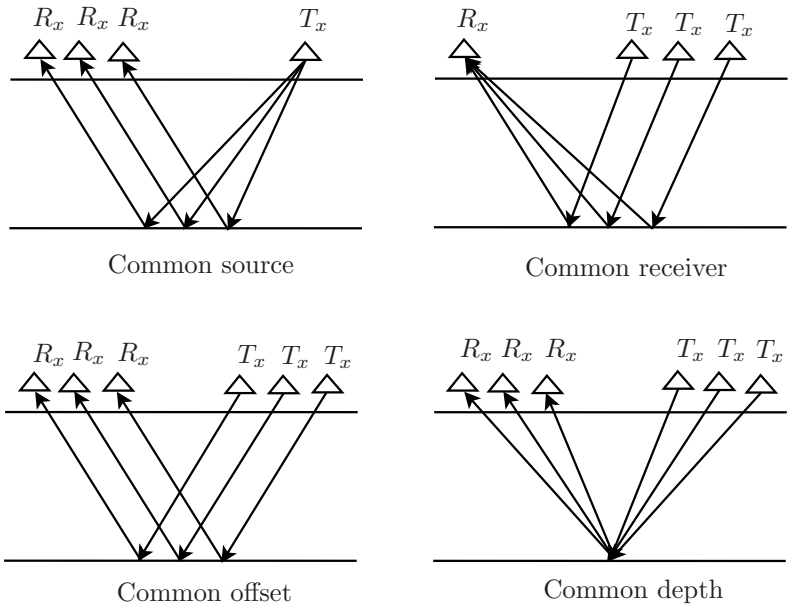

Figure 2.5. GPR geophysical surveying modes.

2.4 GPR for Landmine Detection

GPR has been widely applied to investigate subsurface structures or buried objects in civil engineering, detection of landmine and UXO, environmental engineering, etc. since the 1970s [10, 15–17]. GPR is one of the oldest technologies, probably next to induction sensors, that has been extensively researched as a means of improving mine detection efficiency [15].

2.4.1 GPR Based Landmine Detection Programs

Currently, many national demining programs are under research and development. The programs are being developed either using GPR only or fusion of GPR array or fused with other sensors. The programs are classified as military or civilian based on the detection capacity. Moreover, they are classified as hand held or vehicle mounted based on the operation during the survey. Some of the national programs involving GPR are tabulated in Table 2.3:

2.4.2 GPR Features

Desirable features for a GPR system include broadband operation, good impedance matching and a small size [15]. GPR can also quickly and accurately determine the

Country	Program (M/C)	Type	Maturity
Australia	HILDA (M)	H	medium
	RRMNS (M)	V	high
Belgium	HUDEM (M)	H	low
Canada	ILDP (M)	V	high
EU	GEODE (C)	V	low
	LOTOS (C)	V	low
	DEMINE (C)	H	low
	MINEREC (C)	H	low
	HOPE (C)	H	low
	PICE (C)	H	low
France	SALMANDER (M)	V	medium
Germany	MMSR (M)	V	medium
Israel	ELTA (M)	V	high
Japan	MEXTSENCION (C)	H	high
Sweden	PICE (C)		medium
UK	MINETECT (C)	H	high
	DCMC (M)	H	medium
	MCMC (M)	V	medium
USA	HSTAMIDS (M)	H	high
	GSTAMIDS (M)	V	low

Table 2.3. National programs involving GPR for landmine detection. V → Vehicle mounted, H → Hand held, M → Military program, C → Civilian program.

subsurface structures. It provides shallow subsurface images sharper than any other geophysical technique in the (0 - 5 m) depth. Advances in UWB equipment and dedicated data processing methods have recently improved the performance of GPR and fostered the possibility of using the sensor for landmine and UXO detection [16].

Numerous field trials of different GPR sensors have proven that GPR sensors can achieve desirable detectability level for most ground types. The decrease of the false alarm rate remains the most important task for GPR developers [15]. False alarms in GPR are caused by natural clutter (roots, rocks, water pockets, etc.) and man-made friendly objects (e.g., soft-drink cans). To reduce the former, ground bounce should be subtracted from the return signal. Accurate subtraction of the ground bounce is one of the major challenges in GPR sensors for landmine detection [25, 26].

Unlike other detection technologies, GPR has the ability to detect metallic and non-metallic mines, and explosives of TNT and RDX buried in dry and wet soils [15]. The GPR equipment can easily move on the ground surface but does not have to touch it. Due to these features, many attempts have been made to employ GPR in buried landmine and UXO detection.

At frequencies below 1.0 GHz, attenuation losses in the ground are small [16] and considerable penetration depth can be achieved. However, landmine detection requires down-range resolution in the order of several centimeters, which can be achieved using frequencies above 1.0 GHz [26]. It was found experimentally that 0.8 ns mono-cycle satisfies the penetration and resolution requirements [26].

The most fundamental choice in GPR is the center frequency and bandwidth of the radar. Vertical resolution is governed by the bandwidth and the speed of EM wave in the medium [15]. The vertical and horizontal resolutions are determined, respectively as:

$$V_r = \frac{c}{2B\sqrt{\mu_r \varepsilon_r}} \tag{2.5a}$$

$$H_r = \frac{c}{4f_c\sqrt{\varepsilon_r}} + \frac{D}{\sqrt{\varepsilon_r + 1}} \tag{2.5b}$$

where V_r is the vertical resolution, H_r is the horizontal resolution, B is the bandwidth, $c = 2.997\ 924\ 58 \times 10^8$ m/s is the speed of EM wave in vacuum, ε_r is the relative dielectric permittivity, μ_r is the relative magnetic permeability of the medium, f_c is the center frequency of the antenna and D is the depth to the plane where the two objects are located.

2.5 Field Data Collection

2.5.1 Experimental Setup and System Parameters

In our experimental setup, we used a Geophysical Survey Systems, Inc. (GSSI) GPR bistatic bow-tie antenna system with a center frequency of 1.5 GHz and 80% bandwidth. The receiver and transmitter antennas are shielded, that is, direct coupling and interference from the surrounding systems is negligible. We have used a distance mode of collection with a survey wheel, 10 scans per cm, 16 bit, 512 sample points per scan and a range of 12 ns. The SIR3000 with a blue cable controller set is used for surveying, recording and visualization. The antenna syatem has an equivalent sampling frequency of 42.67 GHz.

The GPR unit is suspended above the ground surface at a height of between 0.5 and 5 cm. Its motion is controlled by a survey cart. Since we have used a distance mode of data collection in a straight track. The scans in the horizontal track correspond to

Model-5100 antenna and model-615 survey cart	
Center frequency:	1500 MHz
Pulse duration:	0.7 ns
Size of sensor:	$1.5 \times 4 \times 6.5$ inches $3.8 \times 10 \times 16.5$ cm
Depth of penetration:	0 - 18" depending on type of soil
Model 615 Survey Cart:	1229 ticks/foot or 4030 ticks/meter
System run mode:	Survey wheel
Range:	6 ns to 12 ns
Number of gain points:	1
Vertical low pass filter:	3000 MHz
Vertical high pass filter:	250 MHz
Horizontal filters	no
Samples per scan:	512
Bits per sample:	16
Scans per second:	Depends on the controller (SIR) system
Scans per meter:	80 scans/meter (24 scans/foot) or more

Table 2.4. 1.5 GHz GPR antenna setup and specification [61].

Surrogate of	Material	Dimensions
M14	PVC casing, paraffin wax filling, small metal parts	52×42 mm
PMN1	PVC casing, paraffin wax filling, small metal parts	120×50 mm
PMN2	PVC casing, paraffin wax	110×55 mm

Table 2.5. Mine-like surrogate targets used for the experiment.

distances from the starting point of the run. The specification and setup of the GPR antenna set used for data collection is given in Table 2.4.

In addition to the surrogate landmines, we also considered false targets, such as a piece of copper wire 50 mm in length, a bullet like metallic object, two irregular shaped rocks, three wood blocks, a soft drink can of 60 mm diameter and 120 mm height and a hollow PVC cylinder with 50 mm diameter and 250 mm length.

2.5.2 Data Collection

The experiment was done at Griesheim old airport and Botanischer Garten, Darmstadt, Germany in July 2011. Three targets, which are surrogates of M14, PMN1 and PMN2, were prepared from PVC cylinders of appropriate size, as given in Table 2.5. The PVC cylinders were filled with wax and a small metal component was placed at the center of the cylinder.

False targets, such as irregular shaped rocks, pieces of wood, hollow PVC cylinder and soft-drink-can have been used in the measurement.

In the Griesheim airport site, pure sand, clay and mixed man-made soils were prepared. However, in the Botanischer Garten site, a naturally clay-loom mixture soil under the vegetation has been used for the experiment.

Chapter 3

GPR Electromagnetic Wave Propagation Modeling

In this chapter, electromagnetic (EM) wave propagation modeling is considered. The aim is, given a set of ground, target and antenna parameters, synthetic data is generated using transmission line (TL) modeling approach.

Section 3.1 motivates the usage and practicality of EM wave propagation approach. Section 3.2 reviews some basic properties of dielectric materials and their effects on an EM wave propagated through them. The main contribution of this chapter is the electromagnetic propagation modeling using transmission line modeling is presented in Section 3.3. Section 3.4 presents the TL modeling steps and the assumptions that should be considered in the modeling. Simulation results and demonstration of the synthetic data using the developed method are provided in Section 3.5 and conclusions are drawn in Section 3.6

3.1 Motivation

The foundations of GPR lie in the electromagnetic (EM) propagation theory. The TL is one of the media through which energy or information can be transferred. There is an analogy between EM wave propagation in soils due to GPR and EM wave propagation in a TL due to the input voltage. In this analogy, the subsurface layers are considered as small sections of TL and this helps to characterize the subsurface ground and other dielectric materials in a suitable way. For this reason, we consider a multilayer modeling based on a TL approach.

3.2 EM Propagation Principles

EM wave propagation deals with the transfer of energy or information from one point to another through a medium such as material space, transmission line, and waveguide [16, 62–66]. EM waves propagate with both electric and magnetic field components which are perpendicular to each other. This is illustrated in Figure 3.1. The propagation of an EM wave in dielectrics, such as in soil, is described using Maxwell's equations.

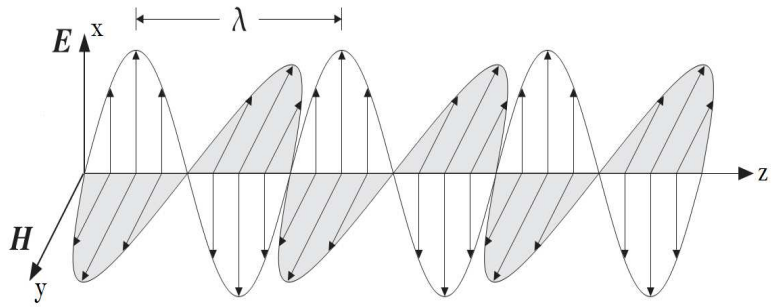

Figure 3.1. Propagation of EM wave in the z-direction.

3.2.1 Maxwell's Equations

Maxwell's equations mathematically describe the physics of EM fields and constitutive relationships quantify EM properties of a material. Combining the two provides the foundations to describe GPR signals quantitatively. Maxwell added modifications and summarized the work of many researchers in a compact form [17, 65, 66]. Analytically, EM field equations and relationships are expressed as follows:

$$\nabla \times \mathbf{E}(\mathbf{r},t) = -\frac{\partial}{\partial t}\mathbf{B}(\mathbf{r},t) \qquad \text{Faraday's law} \tag{3.1}$$

$$\nabla \times \mathbf{H}(\mathbf{r},t) = \frac{\partial}{\partial t}\mathbf{D}(\mathbf{r},t) + \mathbf{J}(\mathbf{r},t) \qquad \text{Ampere's circuit law} \tag{3.2}$$

$$\nabla \cdot \mathbf{D}(\mathbf{r},t) = \rho(\mathbf{r},t) \qquad \text{Gauss's law} \tag{3.3}$$

$$\nabla \cdot \mathbf{B}(\mathbf{r},t) = 0 \qquad \text{Non existent} \tag{3.4}$$

where ∇ is a nabla operator, which is given by the sum of first order partial derivatives of a function. $\mathbf{E}$ and $\mathbf{H}$ are the electric and magnetic field strengths and are measured in units of (V/m) and (A/m), respectively. The quantities $\mathbf{D}$ and $\mathbf{B}$ are the electric and magnetic field displacements and are measured in units (C/m^2) and (Wb/m^2 or T), respectively. The quantities $\mathbf{J}$ and ρ represent the current density and charge density, and are measured in units (A/m^2) and (C/m^3), respectively, and t is the time in (sec).

An auxiliary relationship between the current and charge densities, $\mathbf{J}$ and ρ, is called the continuity equation and is given by:

$$\nabla \cdot \mathbf{J}(\mathbf{r},t) = -\frac{\partial}{\partial t}\rho(\mathbf{r},t) \tag{3.5}$$

The constitutive relationships between the field quantities and electromagnetic displacements provide the additional constraints needed to solve Equations (3.1) and

(3.2). These equations are means of describing materials' response to an EM field in terms of three scalar quantities as:

$$\mathbf{J} = \sigma\mathbf{E} \tag{3.6}$$

$$\mathbf{D} = \varepsilon\mathbf{E} = \varepsilon_0\varepsilon_r\mathbf{E} \tag{3.7}$$

$$\mathbf{B} = \mu\mathbf{H} = \mu_0\mu_r\mathbf{H} \tag{3.8}$$

where σ is the electrical conductivity, ε is dielectric permittivity and μ is the magnetic permeability of the material. The free space permeability, $\mu_0 = 4\pi \times 10^{-7}$ H/m and free space permittivity, $\varepsilon_0 = 8.85 \times 10^{-12}$ F/m. The relative quantities, μ_r and ε_r are unitless quantities that describe the atomic and molecular dipoles of the material and magnetic dipole moments of the atoms constituting the medium [59, 63–65].

E and **H** are functions of time and space. It is possible to simplify the problem by assuming the fields are time harmonic, that is, the fields are varying with a sinusoidal frequency. For

$$\mathbf{E}(x, y, z, t) = \mathbf{E}_0(r)(\cos(\omega t + \phi(r)) \tag{3.9}$$

$$\mathbf{H}(x, y, z, t) = \mathbf{H}_0(r)\cos(\omega t + \phi(r)) \tag{3.10}$$

where $\mathbf{E}_0(r)$ and $\mathbf{H}_0(r)$ are the vector amplitudes of the electric and magnetic fields, respectively, whereas $\phi(r)$ is the initial phase. The electric and magnetic fields are represented in phasor form as:

$$\mathbf{E}(r) = \mathbf{E}_0(r)e^{(j\phi(r))} \tag{3.11}$$

$$\mathbf{H}(r) = \mathbf{H}_0(r)e^{(j\phi(r))} \tag{3.12}$$

The solution of Maxwell's equations in a source free ($\mathbf{J} = 0$ and $\rho = 0$) and a lossy medium is given by:

$$\nabla^2 E - \gamma^2 E = 0 \tag{3.13}$$

$$\nabla^2 H - \gamma^2 H = 0 \tag{3.14}$$

where γ is a complex number representing the propagation constant of a medium.

$$\gamma = \alpha + j\beta = \sqrt{j\omega\mu(\sigma + j\omega\varepsilon)} \tag{3.15}$$

where α is the attenuation constant in (Np/m) and β is the phase constant of the medium measured in (rad/m).

$$\alpha = \omega \sqrt{\frac{\mu\varepsilon}{2}\left[\sqrt{1+\left(\frac{\sigma}{\omega\varepsilon}\right)^2}-1\right]} \tag{3.16}$$

$$\beta = \omega \sqrt{\frac{\mu\varepsilon}{2}\left[\sqrt{1+\left(\frac{\sigma}{\omega\varepsilon}\right)^2}+1\right]} \tag{3.17}$$

where $\omega = 2\pi f$ is the angular frequency of the wave.

If we assume that the wave propagates in the z-direction and the electric field polarizes in the x-direction, solving Equations (3.13) and (3.14), we obtain:

$$E_x(z,t) = E_0 e^{-\alpha z}\cos(\omega t - \beta z) \tag{3.18}$$

From Equation (3.18), we can understand the significance of α and β. The quantity α represents the exponential decay in the electric field intensity and β represents the phase velocity in a medium as the wave travels in the z-direction. In a similar way, the magnetic field intensity in the y-direction is given by:

$$H_y(z,t) = H_0 e^{-\alpha z}\cos(\omega t - \beta z - \phi) \tag{3.19}$$

where the ratio of the amplitudes of the electric field to the magnetic field is defined as an intrinsic impedance $|\eta| = E_0/H_0$, η is $|\eta|e^{j\theta}$. The intrinsic impedance is represented as a function of the angular frequency and the medium parameters as:

$$\eta = \sqrt{\frac{j\omega\mu}{\sigma + j\omega\varepsilon}} = \frac{\sqrt{\mu/\varepsilon}}{\sqrt[4]{1+\left(\frac{\sigma}{\omega\varepsilon}\right)^2}} e^{j\phi} \tag{3.20}$$

where $\phi = \tan^{-1}(\sigma/\omega\varepsilon)/2$ is the angle contributed by the intrinsic impedance and has a value that ranges from 0 to 45 °. The intrinsic impedance of free space η_0 simplifies to

$$\eta_0 = \sqrt{\frac{j\omega\mu_0}{0 + j\omega\varepsilon_0}} = \sqrt{\frac{\mu_0}{\varepsilon_0}} \approx 376.6\Omega \tag{3.21}$$

3.2.2 Electromagnetic Properties of Materials

The behavior of a propagating EM wave depends on the properties of the medium through which it propagates. The velocity of the propagation, the fraction which is bounced back or transmitted, the amount of attenuation and loss are dependent on the electromagnetic properties of the media and frequency of propagation. The most important electromagnetic properties of these materials are: dielectric permittivity, magnetic permeability and electric conductivity. Different dielectric materials have different electromagnetic properties. The nature of dielectric materials affects the propagation behavior of the electromagnetic wave. The significance of the electromagnetic properties of the media is described in the following subsections.

Dielectric permittivity (ε)

The dielectric permittivity or simply permittivity of a medium is a measure of the material's ability to allow the formation of an electric field within it [67]. In other words, it is a measure of how an electric field affects and is affected by a dielectric medium. Absolute permittivity is expressed relative to free space permittivity, which is assumed to be the same as the permittivity of vacuum. The relative permittivity, also called the dielectric constant, ε_r, of a material is, the ratio of its permittivity to that of free space.

Although the permittivity of a material can be frequency dependent, experiments have shown that earth materials at a typical GPR frequency show little variation in permittivity [16]. The solid constituents of most soils and man-made materials have relative dielectric constant in the range from 2 to 9. The measured values of ε_r for soils and building materials lie mainly in the range from 4 to 40 [16, 17, 66, 68]. The permittivity of subsurface materials can vary greatly, for example in the presence of bound water. It is usually a complex and frequency-dependent quantity with real (storage) and imaginary (loss) components, and is given as:

$$\varepsilon = \varepsilon^{'} - j\varepsilon^{''} \tag{3.22}$$

where ε' and ε'' are the real and imaginary parts of the permittivity, respectively. ε' is a measure of the ability of the medium to be polarized under an electric field and ε'' is a measure related to losses of the material associated with the conductivity and the frequency [16]. The relative permittivity of a material governs the velocity of propagation of an EM wave through the medium [17, 66].

Although permittivity is a property associated with dielectric materials, we may still consider an effective permittivity of pure conductors, with real relative permittivity equal to one [65]. So, the complex permittivity of a metal is practically a purely imaginary number expressed in terms of the imaginary unit and a real-valued electrical conductivity [67].

Magnetic Permeability (μ)

Magnetic permeability (μ) is the ability of a material to support the formation of a magnetic field within it. The relative permeability of a material is the ratio of its permeability to that of free space, i.e, $\mu_r = \mu/\mu_0$, and is a unitless quantity [66]. Magnetic permeability has little effect on the propagation of a GPR wave [69] and therefore, the magnetic permeability of subsurface materials is often assumed to be equal to the free space value, μ_0.

Ferromagnetic materials with a relative permeability, $\mu_r \gg 1$, have considerable effect on the EM wave propagation velocity and attenuation [17]. They are also considered to be magnetically lossy and may have a frequency dependent permeability. For ferromagnetic materials, the permeability can have an imaginary component [66]. Soil and subsurface materials are mainly non-ferromagnetic ($\mu_r \approx 1$), therefore, they are assumed to be the same as free space ($\mu_r = 1$). However, some metallic landmines and UXO show ferromagnetic properties.

Conductivity(σ)

In simple terms, conductivity describes the ability of a material to pass free electric charges under the influence of an applied EM field. [16,17,66,69]. Electrical conductivity is a measure of the material's ability to conduct an electric current and is measured in S/m. Conductivity has a significant effect on the attenuation of a radar signal [17].

For soils and ground materials, conductivity is assumed to be isotropic, having the same value in each direction. Metallic landmines have higher conductivity, whereas plastic landmines have low conductivity. Soils have conductivity in the range of 0.0001 to 0.1 (S/m) and free space has zero conductivity. Table 3.1. shows the electromagnetic properties of some common subsurface materials at a frequency of 100 MHz. The complex conductivity of a medium is given by:

$$\sigma = \sigma^{'} - j\sigma^{''} \tag{3.23}$$

where the real component, σ', describes how well the medium conducts electric current. At higher frequencies the response time becomes significant and results in an out-of-phase component. The imaginary part of the conductivity, σ'', is related to the out-of-phase polarization component and is usually small at high radar frequencies. In most cases, conductivity is assumed to be independent of frequency, real valued and is related only to the ionic conductance of the material [17]. However, the total storage and loss effects of the medium is described by the complex effective relative permittivity of the medium.

$$\varepsilon_e^* = \varepsilon^{'} - j(\varepsilon^{''} + \frac{\sigma}{\omega\varepsilon_0}) \tag{3.24}$$

For conductive dielectrics, the macroscopic parameters σ and ε always occur in a combined manner, as:

$$\begin{aligned} \sigma + j\omega\varepsilon &= (\sigma^{'} + \omega\varepsilon^{''}) + j\omega(\varepsilon^{'} - \tfrac{\sigma^{''}}{\omega}) \\ &= \sigma_e + j\omega\varepsilon_e \end{aligned} \tag{3.25}$$

where $\sigma_e = \sigma^{'} + \omega\varepsilon^{''}$ is defined as real effective conductivity and $\varepsilon_e = \omega(\varepsilon^{'} - \frac{\sigma^{''}}{\omega})$ is defined as the real effective permittivity.

Wave Velocity (v)

The propagation velocity of an EM wave in free space is assumed to be the same as in vacuum, c, but depending on the relative permittivity and relative permeability of a medium reduces to $c/\sqrt{\mu_r\varepsilon_r}$ [59]. The velocity at which the wave travels through a medium is proportional to the angular velocity of the wave. For an observer moving along with the same velocity as the wave, an arbitrary point on the wave will appear to be constant. This requires that the argument of the $E(z,t)$ to be constant and is defined by:

$$\omega t - \beta z + \theta = constant \tag{3.26}$$

Taking the derivative with respect to t, we obtain:

$$\frac{dz}{dt} = \frac{\omega}{\beta} = v \tag{3.27}$$

Dielectric medium	Static conductivity σ(S/m)	Relative permittivity ε_r	Attenuation (dB/m)
Air	0	1	0
Clay dry	$10^{-2} - 10^{-1}$	2 - 20	10 - 50
Clay wet	$10^{-1} - 10^{0}$	15 - 40	20 - 100
Freshwater	$10^{-6} - 10^{-2}$	81	0.01
Freshwater ice	$10^{-4} - 10^{-3}$	4	0.1 - 2
Seawater	100	81	100
Seawater ice	$10 - 100$	4 - 8	1 - 30
Limestone dry	$10^{-8} - 10^{-6}$	7	0.5 - 10
Limestone wet	$10^{-4} - 10^{-2}$	5 - 10	1 - 20
Sandstone dry	$10^{-6} - 10^{-5}$	2 - 5	2 - 10
Sandstone wet	$10^{-4} - 10^{-2}$	5 - 10	4 - 20
Sand dry	$10^{-7} - 10^{-3}$	2 - 6	0.01 - 5
Sand wet	$10^{-3} - 10^{-2}$	10 - 30	0.5 - 5
Soil sandy, dry	$10^{-4} - 10^{-3}$	4 - 10	0.1 - 2
Soil sandy, wet	$10^{-2} - 10^{-1}$	10 - 30	1 - 5
Soil loamy, dry	$10^{-4} - 10^{-3}$	4 - 10	0.5 - 3
Soil loamy, wet	$10^{-2} - 10^{-1}$	10 - 30	1 - 6
Soil clayey, dry	$10^{-2} - 10^{-1}$	4 - 10	0.3 - 3
Soil clayey, wet	$10^{-1} - 10^{0}$	10 - 30	5 - 50
PVC	3	0.003	30
TNT	2.86	0.00029	9.75

Table 3.1. Relative permittivity, conductivity and attenuation of some common subsurface materials at 100 MHz and their typical range under natural conditions [16, 17, 60].

where v is defined as phase velocity, which is given by:

$$v = \frac{\omega}{\beta} = \frac{1/\sqrt{\mu\varepsilon}}{\sqrt{\frac{1}{2}\left[\sqrt{1+\left(\frac{\sigma}{\omega\varepsilon}\right)^2}+1\right]}} \tag{3.28}$$

The wave velocity in free space, where ($\sigma = 0$, $\mu = \mu_0$ and $\varepsilon = \varepsilon_0$), is given by:

$$v = \frac{\omega}{\beta} = \frac{1}{\sqrt{\mu_0\varepsilon_0}} = c \tag{3.29}$$

Equivalent Travel Time

Equivalent travel time is the time taken by the wave to travel through a given medium. The travel time is directly proportional to the dielectric constant of the medium and

is given by:

$$t_r(n) = \frac{r_n}{v_n} = r_n \cdot \frac{\sqrt{\varepsilon_{r,n}}}{c} \tag{3.30}$$

where v_n is velocity of EM wave at n^{th} layer, r_n and $\varepsilon_{r,n}$ are the thickness and relative permittivity of the n^{th} media, respectively.

3.3 Transmission Line Modeling Principles

In this modeling approach, the signal reflected from each layer is represented by a time-delta function and additive noise components. The backscattered signal is then calculated as a convolution sum of the delta functions and the driving impulse function.

The useful received GPR signal model at position $x = 1, 2, \ldots, M$ and discrete time $t = 1, 2 \ldots, N$, as used in [42, 43, 70, 71], is given by:

$$\mathbf{y}(t, x) = \mathbf{s}_c(t, x) + \sum_{m=-M}^{M} \mathbf{w}(m)\mathbf{f}(t - m, x) + \mathbf{s}_n(t, x) \tag{3.31}$$

where $\mathbf{w}(m)$ is a driving wavelet function with width of $2M + 1$, M is a temporal support of the two-sided wavelet function, $\mathbf{s}_c$ is the direct pulse measured by the receiver antenna, $\mathbf{s}_n(t, x)$ is additive noise and $\mathbf{f}(t, x)$ is a set of time-delta echoes reflected from the subsurface layers and is defined as:

$$\mathbf{f}(t, x) = \sum_{n=1}^{N_l - 1} P_{tr}(n, x)\delta(t - t_d(n, x)) \tag{3.32}$$

where N_l is the maximum number of layers including air, $t_d(n, x)$ is the pulse echo time delay of the n^{th} interface and $P_{tr}(n, x)$ is the transmission-reflection product of the n^{th} interface and is given by:

$$P_{tr}(n, x) = \begin{cases} \Gamma_{0,1}(x) & n = 1 \\ \Gamma_{n-1,n}(x) \prod_{i=1}^{n-1} T_{i-1,i}(x) T_{i,i-1}(x) & n \geq 2 \end{cases} \tag{3.33}$$

where $\Gamma_{i,j}$ and $T_{i,j}$ are the reflection and transmission coefficients of the $i - j$ interface, respectively.

3.3.1 Transmission Line Modeling Basics

The purpose of this section is to introduce TL modeling as an alternative method to EM propagation modeling. From a mathematical point of view, it has close links to the standard numerical techniques, but it is far superior in terms of its ease of physical interpretation and flexibility. This method relies on circuit variables and concepts to describe the behavior of the medium [23, 24, 72].

A TL is a pair of electrical conductors that carries an electrical signal from one place to another in a fixed time [62–65, 72]. The structure can be analyzed using circuit theory concepts, provided that the problem can be broken down into small parts. A small section, lumped model, of TL equivalent circuit with length dz is shown in Figure 3.2.

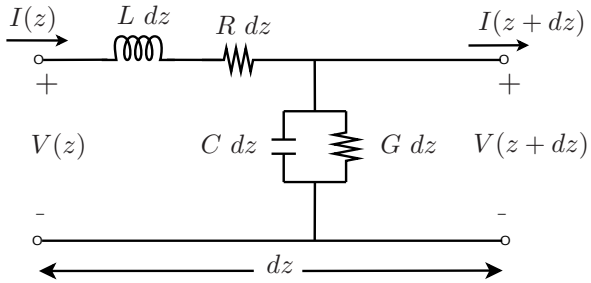

Figure 3.2. Lumped model of TL with length dz.

Using simple circuit analysis, the voltage and current equations of the circuit are:

$$V(z) - V(z+dz) = \frac{\partial I(z)}{\partial t} L dz + I(z) R dz \tag{3.34}$$

$$I(z) - I(z+dz) = \frac{\partial V(z+dz)}{\partial t} C dz + V(z+dz) G dz \tag{3.35}$$

The solution for the voltage and current equations are given as:

$$V(z,t) = V_0 e^{-\gamma z} e^{j\omega t} = V_0 e^{-\alpha z} e^{j(\omega t - \beta z)} \tag{3.36}$$

Similarly the instantaneous current is given by:

$$I(z,t) = I_0 e^{-\gamma z} e^{j\omega t} = I_0 e^{-\alpha z} e^{j(\omega t - \beta z - \theta)} \tag{3.37}$$

where $I_0 = V_0/|Z|$, Z is the characteristic impedance of the lamped circuit and is defined as the ratio of voltage to current in the same direction.

$$Z = \frac{V}{I} = \sqrt{\frac{R + j\omega L}{G + j\omega C}} \tag{3.38}$$

The complex propagation constant of the circuit is defined as:

$$\gamma = \alpha + j\beta = \sqrt{(R + j\omega L)(G + j\omega C)} \tag{3.39}$$

where R, L, G and C represent the per unit length parameters of the circuit resistance, inductance, conductance and capacitance, respectively.

In summary, the EM wave propagation equations in dielectric materials are similar to the EM wave equations in TL. The electric field in Equation (3.9) and the voltage in Equation (3.36) can be used interchangeably. Hence, the equivalence can be achieved using the assumptions, $V \leftrightarrow E$, $I \leftrightarrow H$, $L \leftrightarrow \mu$, $C \leftrightarrow \varepsilon$, $G \leftrightarrow \sigma$, $R \leftrightarrow 0$ and $Z \leftrightarrow \eta$.

The TL equivalent modeling approach is conceptually simple and can be used for the GPR EM wave propagation in subsurface soils. The approach is useful for assessing the time domain signature of a physical phenomenon [16, 22, 23, 72–74].

The TL modeling process begins by choosing the number of layers and specifying the EM parameters for each layer. The parameters include layer thickness, electrical conductivity, relative permittivity, relative magnetic permeability, and the distribution and dispersion parameters. The intrinsic impedance, the equivalent travel time, wave velocity and propagation constant are calculated for each layer. At each interface, reflection coefficient, transmission coefficient, echo pulse function and two way travel time is calculated. For a full system representation, intra-layer multiple reflections should also be considered. A-scan is generated as a convolution of the driving wavelet function and the echo pulse function. The TL multilayer EM propagation modeling steps are depicted in Figure 3.2.

This modeling problem can be very complex without some simplifying assumptions. These assumptions include the incident wavefront and material boundary to be planar surfaces and assuming only uniform plane waves. The polarization effect can be eliminated by considering the problem only in two directions, where the incident wave is linearly polarized along the third dimension.

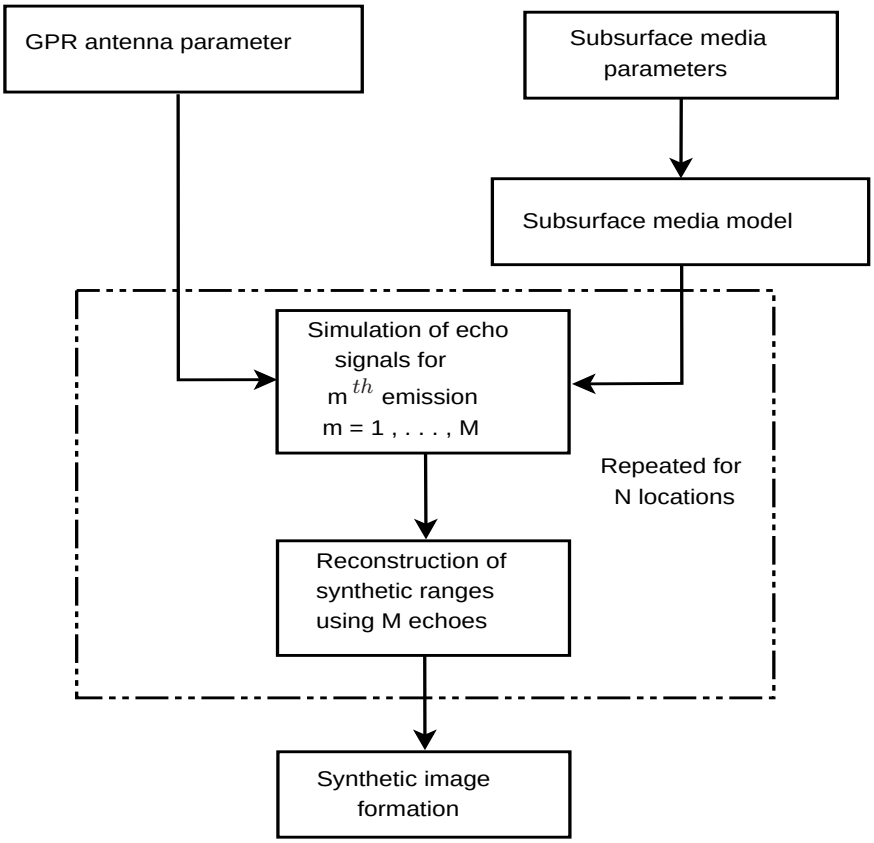

Figure 3.3. TL EM propagation modeling steps.

We consider a multilayer medium consisting of N_l layers with each layer characterized with specific attributes. These attributes are: prescribed layer thickness (r_n), relative electric permittivity ($\varepsilon_{r,n}$), relative magnetic permeability ($\mu_{r,n}$) and conductivity (σ_n) and loss tangent ($\tan(\delta_n)$), where n indicates the layer number. From these attributes the propagation constant, intrinsic impedance, attenuation and phase constants are calculated.

3.3.2 Reflection and Transmission at Interfaces

When an EM wave is incident to a boundary between two adjacent media, some portion of the incident wave is reflected or transmitted from the interface of contrasting dielectric properties [69]. The amplitudes and directions of reflection or transmission mainly depend on the incident wave amplitude, angle of incidence, the radius of curvature of the interface and the difference in dielectric properties of the adjacent media.

These reflections make EM energy propagate back towards the receiving antenna and

are termed as backscattered. A certain amount of energy is also transmitted and will result in further reflections at any other boundaries encountered.

The Fresnel equations describe the relationships between the incident and transmitted, T, or reflected, Γ. For a vertically polarized electromagnetic waves, the reflection and transmission coefficients are given by:

$$\Gamma = \frac{\eta_i \cos\theta_i - \eta_t \cos\theta_t}{\eta_i \cos\theta_i + \eta_t \cos\theta_t} \tag{3.40}$$

$$T = \frac{2\eta_i \cos\theta_i}{\eta_i \cos\theta_i + \eta_t \cos\theta_t} \tag{3.41}$$

where θ_i is the incident angle where as θ_t is the refraction angle. For normal incidence, i.e., $\theta_i = \theta_t = 0\,^\circ$ and Equations (3.40) and (3.41) are simplify to:

$$\Gamma = \frac{\eta_i - \eta_t}{\eta_i + \eta_t} \tag{3.42}$$

$$T = \frac{2\eta_i}{\eta_i + \eta_t} \tag{3.43}$$

At the n^{th} interface of the subsurface, reflection coefficients to the forward and reverse directions are, respectively given as [23]:

$$\Gamma_{fn} = \Gamma_{n-1,n} = \frac{\eta_n - \eta_{n-1}}{\eta_n + \eta_{n-1}}, \text{ for } n \geq 1 \tag{3.44}$$

$$\Gamma_{rn} = \Gamma_{n,n-1} = \frac{\eta_{n-1} - \eta_n}{\eta_{n-1} + \eta_n}, \text{ for } n \geq 1 \tag{3.45}$$

Similarly, transmission coefficients in the forward and reverse directions are, respectively, given by:

$$T_{fn} = \frac{2\eta_{n-1}}{\eta_n + \eta_{n-1}} \tag{3.46}$$

$$T_{rn} = \frac{2\eta_n}{\eta_{n-1} + \eta_n} \tag{3.47}$$

3.3.3 Multiple Reflection Scenario

Reflection and transmission of the GPR signal occurs at the boundaries of two media with contrasting dielectric properties. With each boundary encountered, the amplitude

of the original signal is attenuated and only some fraction of the originally transmitted signal is measured by a receiver.

In a layer bounded between two media of different EM properties, in addition to the primary reflection which occurs at an interface, multiple reflections are generated at the interfaces [16, 75]. The multiple reflections occur when the transmitted signal travels through a layer bounded by two different layers. If a single reflection travel time is considered, it is important to differentiate the primary reflections from multiple reflections since the multiples do not represent true interfaces at a depth. The situation is depicted in Figure 3.4.

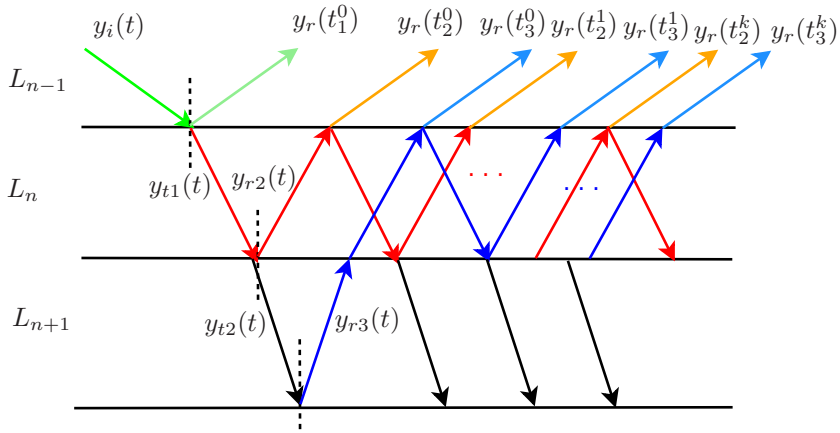

Figure 3.4. Multi-reflection scenario in subsurface layers.

where $y_i(t)$ is the incident signal, $y_r(t_n^k)$ is the k^{th} reflection of the n^{th} interface, $y_{tn}(t)$ is the signal transmitted through the $n-1, n$ interface, $t_n^k = t - 2k \times t_r(n)$ indicates delayed time indexes of the reflected signal. The backscattered signal with multiple reflections is given by:

$$y(t) = \sum_{n=1}^{N_l-1} \sum_{k=0}^{K(n)} y_r(t_n^k) \tag{3.48}$$

where $K(n)$ indicates the maximum allowable number of multiple reflections in the n^{th} layer, $K(n) \leq \frac{t_D - t_d(n-1)}{t_r(n)}$, t_D is the total acceptable time delay or range (ns) of the antenna setup and $t_d(n)$ is the pulse echo time delay of layer n.

Multiple reflections at layer L_n are caused by the signal transmitted from layer L_{n-1} and signal transmitted back from layer L_{n+1}. The number of reflections are infinite, however, only few of the multiple reflections correspond to the true reflections [75]. In our propagation modeling we consider the multiple reflections which occurred only within the travel time of a single pulse.

In each layer, the infinite multiple reflections due to the incident waves are given as a superposition of the reflections due to each incident wave.

$$\Gamma_r(n) = \Gamma_r^f(n) + \Gamma_r^r(n) = (\Gamma_{n,n-1} + 1)\frac{\Gamma_{n,n-1}\Gamma_{n-1,n}}{1 - \Gamma_{n,n-1}\Gamma_{n-1,n}} \tag{3.49}$$

and

$$\Gamma_f(n) = \Gamma_f^f(n) + \Gamma_f^r(n) = (\Gamma_{n-1,n} + 1)\frac{\Gamma_{n,n-1}\Gamma_{n-1,n}}{1 - \Gamma_{n,n-1}\Gamma_{n-1,n}} \tag{3.50}$$

where $\Gamma_f(n)$ and $\Gamma_r(n)$ are the superposed reflected waves in the forward and reverse directions, respectively.

The acceptable number of multiple reflections in a given layer is determined using the following relationships,:

$$\Gamma_f(n) = (\Gamma_{n-1,n} + 1)\sum_{k=0}^{K(n)}(\Gamma_{n,n-1}\Gamma_{n-1,n})^k\delta(t - 2k \times t_r(n)) \tag{3.51}$$

$$\Gamma_r(n) = (\Gamma_{n,n-1} + 1))\sum_{k=0}^{K(n)}(\Gamma_{n,n-1}\Gamma_{n-1,n})^k\delta(t - 2k \times t_r(n)) \tag{3.52}$$

3.3.4 Effect of Moisture

The amount of moisture present in a porous medium affects the permittivity and conductivity characteristics of the medium. In general, the relative permittivity of porous materials increases with increasing water content. The EM wave velocity through the medium decreases as a result of the increase in permittivity [16, 17, 76, 77].

When two porous media are mixed, such as addition of water into a soil medium, the mixture will have relative permittivity value between the two media. The knowledge of individual permittivities and fractional volume percentages of the materials, such as 5%, 10% moisture, the complex permittivity of the mixture is given by the complex refractive index method (CRIM) [17, 77–79], as:

$$\varepsilon_{mix}^e = \left(\sum_{i=1}^{N} f_i\sqrt{\varepsilon_i}\right)^2 \tag{3.53}$$

where, ε_{mix}^e is the effective permittivity of the mixture, f_i are the fractional volume of the respective components and ε_i are the absolute permittivities of the respective components. The summation of the fractional volumes gives unity, i.e.,

$$f_1 + f_2 + \ldots + f_N = 1 \tag{3.54}$$

3.4 Assumptions and Modeling Steps

Multilayer modeling is a useful tool in determining the feasibility of using GPR at a particular site and for a particular application. It also helps to decide what antenna frequency is suitable for detecting layers of varying thickness, and what type of response would be expected for various combinations of conductivity, dielectric permittivity and magnetic permeability. Using multilayer modeling, it is possible to study the behavior of the backscattered signal for different antenna center frequency in the presence of various targets, and in different soil types having varying moisture levels. Moreover, it is possible to generate radargrams of different scenarios and predict the nature of a buried target by comparing the returned signals of measured GPR data.

3.4.1 Assumptions

Horizontally layered media is a reasonable assumption to simplify the wave propagation path and to obtain an initial model response. The absence of electric and magnetic polarization is a direct result of the assumption of the normal incidence and horizontal interface. In reality, the electric field does not maintain its linearity at the interface and becomes polarized in some elliptical form [75]. However, the receiver measures only the component of the field in the same direction as the transmitted field.

The conductivity of the material is a major factor in determining the degree of signal attenuation. The higher the conductivity value, the greater the amount of energy that is absorbed by the medium. Soils having high clay and moisture content can absorb much of the transmitted signal and thus, the GPR will not be able to see below that layer.

The effect of incidence angle on the reflection and transmission coefficients is investigated using Fresnel equations. As a general rule of thumb, the separation between transmitter and receiver should be approximately 20% of the target depth [75]. This corresponds to an incidence angle less than 6 °.

Dispersion occurs when the velocity of the wave in a material varies with frequency. Both dielectric, magnetic and conductive losses cause dispersion. It is often assumed that the velocity in a given layer is constant, although the velocity is frequency dependent.

Scattering is caused by objects dispersed in the media, such as gravel or rocks which scatter the signal in multiple directions. The primary effect of scattering is the reduction of the signal strength. Scattering is not considered in our modeling procedure.

3.4.2 Transmission Line Modeling Steps

The TL based multilayer EM propagation modeling begins by choosing the number of layers in the model and specifying the parameter values for each layer. The parameters include layer thickness, electrical conductivity, relative dielectric permittivity, relative magnetic permeability, and the distribution and dispersion parameters. The intrinsic impedance, the equivalent travel time and propagation constant are calculated for each layer. At each interface, reflection coefficient, transmission coefficient, echo pulse function and two way travel time are calculated. The composite signal reflected from an interface calculated as a convolution of the driving function and the echo pulse function.

The Ricker wavelet waveform, which closely approximates the pulse transmitted by GPR, has been used as the driving function in the literature [16,17,75]. The composite waveform is computed from the convolution sum of the driving function with the delta function. The A-scan is generated as a superposition of all composite waveforms along the depth [75, 80]. For a given antenna center frequency f_c, the second order time-domain Ricker wavelet is given by:

$$\mathbf{w}(t) = (1 - 2\pi^2 f_c^2 t^2) e^{-\pi^2 f_c^2 t^2} \tag{3.55}$$

The second order Ricker wavelet defined in Equation (3.55) is employed as a driving function for all simulations in Chapter 3 and inverse multilayer modeling in Chapter 4 of this report. The modeling steps are tabulated in Table 3.2.

3.5 Simulations and Synthetic Data Generation

We have considered a setup of clay, sand and loom soils with electrical characteristics as listed in Table 3.3 for the TL modeling based synthetic data generation. We consider the subsurface in the presence of ground roughness, inhomogeneities and at different moisture levels. In our simulations, metallic and plastic targets of different size with relative permittivities 1 and 2.95, respectively, and conductivities 250 and 0.00029 S/m, respectively, and unity relative permeability are considered.

Step 1.	For each layer n, obtain EM properties of the layers $\mu_{r,n}$, $\varepsilon_{r,n}$, σ_n and layer thickness r_n, where $r_{N_l} = \infty$.
Step 2.	Obtain amount of moisture added to the media and calculate the effective permittivity for porous layers using Equation (3.53).
Step 3.	Calculate complex effective permittivity ε^* of each layer as given in Equation (3.24).
Step 4.	Compute intrinsic impedance, $\eta_n = \sqrt{j\omega\mu_n/(\sigma_n + j\omega\varepsilon_n^*)}$, and propagation, attenuation and phase constants respectively, as $\gamma_n = \sqrt{j\omega\mu_n(\sigma_n + j\omega\varepsilon_n^*)}$, $\alpha_n = Re(\gamma_n)$ and $\beta_n = Im(\gamma_n)$
Step 5.	Reflection and transmission coefficients of the adjacent layers in the forward and reverse directions are obtained using Equations (3.44) through (3.47) and multi-reflections in each layer is calculated using Equations (3.51) and (3.52).
Step 6.	Compute transmission-reflection products of the n^{th} interface: $P_{tr}(1) = \Gamma_{0,1}$, $P_{tr}(n) = \Gamma_{n-1,n} \prod_{i=1}^{n-1} T_{i-1,i}T_{i,i-1}$ for $n \geq 2$, and due to multiple reflections, $P_{tr}^m(1) = 0$, $P_{tr}^m(n) = (\Gamma_f(n) + \Gamma_r(n)\delta(t - 2t_r(n))) \prod_{i=1}^{n-1} T_{i-1,i}T_{i,i-1}$ for $n \geq 2$.
Step 7.	Calculate EM wave velocity in each layer $v_n = \frac{c}{\sqrt{\varepsilon_{r,n}\mu_{r,n}}}$ and pulse echo delay of each interface $t_d(n) = 2\sum_{i=0}^{n-1} \frac{r_i}{v_i}$, $n \geq 1$ where $n = 0$ corresponds to air.
Step 8.	Calculate pulse echo function for each interface $f(t) = \sum_{n=1}^{N_l-1} (P_{tr}(n) + P_{tr}^m(n))\delta(t - t_d(n))$
Step 9.	A-scan is generated as convolution of Ricker wavelet the pulse echo function $\mathbf{y}(t) = \sum_{m=-M}^{M} \underline{w}(m)\mathbf{f}(t - m)$

Table 3.2. Procedure for time-domain EM propagation modeling of GPR.

Medium	ε_r	σ (S/m)	α (Np/m)	β (rad/m)	η (ohm/m)
Air	1	0	0	20.98	376.6
Sand	3 - 6	0.0001 - 0.01	0.01 - 1.1	36.3 - 53	154 - 218
Clay Soil	2 - 6	0.01 - 0.1	0.77 - 12	29.7 - 54	151 - 266
Dry soil	2.95	0.004	0.4388	36	216
Water	81	0.01	0.209	188.61	41
TNT	2.86	0.00029	0.03231	35.44	223
PVC	3	0.003	0.3254	36.30	215

Table 3.3. EM properties and calculated parameters of materials used in the simulation.

The metallic and plastic targets are placed 5 cm below the ground surface and the GPR antenna set is assumed to scan 2.5 cm above the ground. The effect of antenna center frequency, amount of added moisture and soil type on the reflected EM wave is investigated. Figure 3.5 shows the backscattered signals from metallic and plastic targets.

The results in Figure 3.6 show the return signal of a metallic target in sand soil for dry, 5% and 10% moisture levels. It can be seen from the figure that the received signal strength and propagation velocity decreases as moisture level increases. The effect of center frequency of the antenna set on the backscattered signal is also tested for 500 MHz, 1.0 GHz and 1.5 GHz. As can be seen from the simulation results in Figure 3.7, the penetration depth decreases when a higher frequency antenna is used. However, resolution is improved with higher center frequency.

Figures 3.8 and 3.9 show the synthetic data generated for two objects of specified conductivity and relative permittivity. The radargram in Figure 3.8 illustrates the case when soil with the specified parameters is dry, whereas, Figure 3.9 displays when 10% moisture is added. The effect of moisture is clearly seen where the contrast between the targets and the soil is changed. As a result of the change in contrast, the characteristics of the reflected signal change.

3.6 Conclusion

In this chapter, multilayer subsurface media consisting of N_l layers with prescribed layer parameters have been considered. The propagation modeling in the presence of metallic and plastic targets was studied. The subsurface layers were assumed to contain different soil types of various moisture levels. The effect of soil type and roughness, and level of moisture on the GPR returns was investigated.

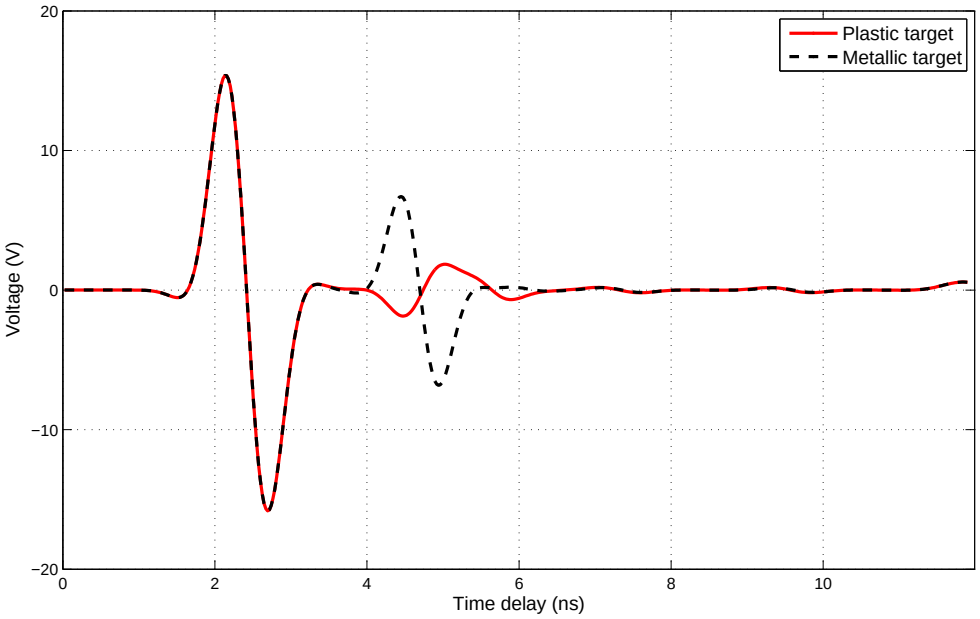

Figure 3.5. Reflections from plastic and metallic objects in sand soil.

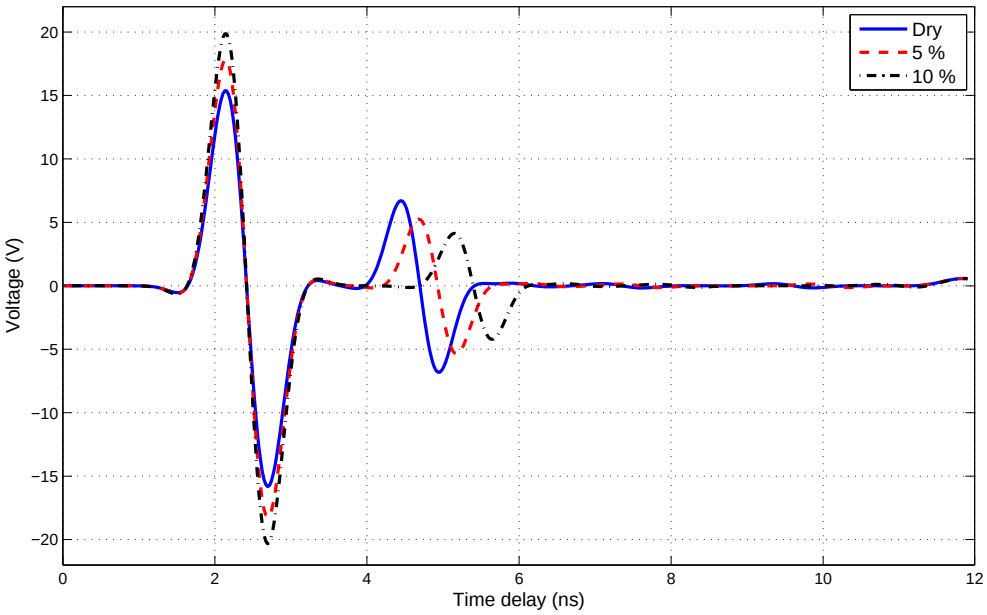

Figure 3.6. Reflections from a metallic target under different moisture levels.

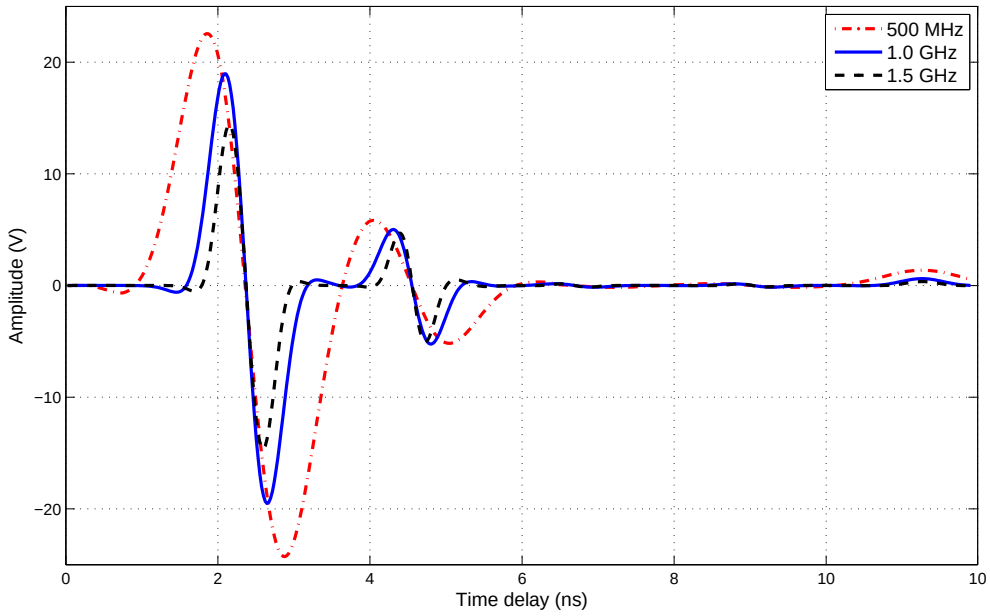

Figure 3.7. Reflections from a plastic target at different center frequencies.

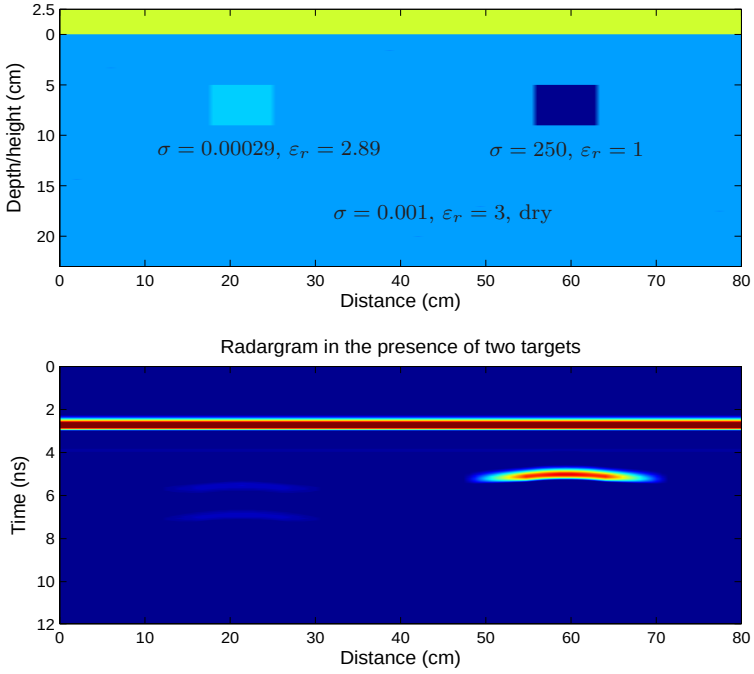

Figure 3.8. Setup and radargram of metallic and plastic targets in dry sand.

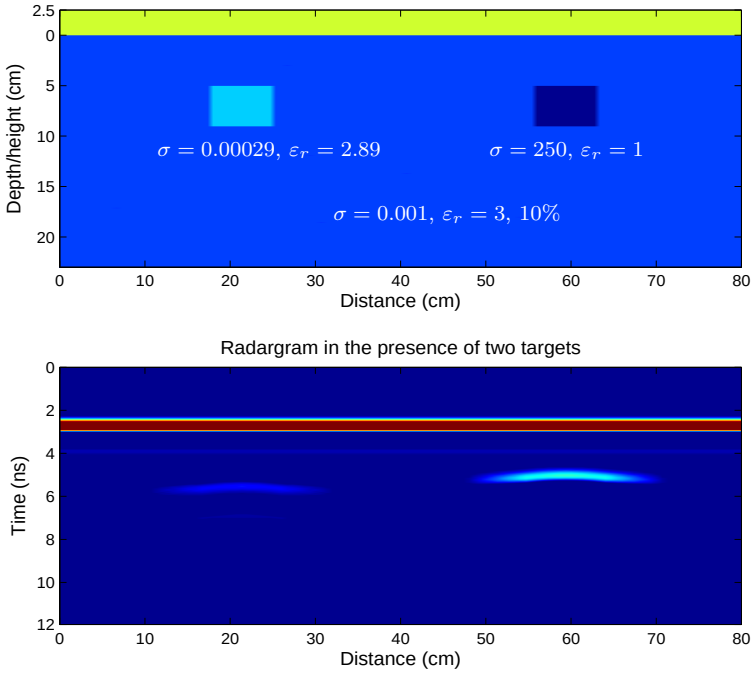

Figure 3.9. Setup and radargram of metallic and plastic targets in wet sand soil.

The TL approach was proposed as an EM propagation modeling technique and it is shown to be the best alternative to the numerical modeling techniques. The proposed modeling approach is computationally easy and is an excellent tool for studying the feasibility of GPR for landmine detection applications in different scenarios. It also helps to choose an antenna with appropriate center frequency, which can be used to detect a certain structure of varying thickness. Moreover, it allows to predict the waveform reflected from media with various combinations of conductivity, dielectric permittivity and magnetic permeability. The simulation results proved the effectiveness of the applied multilayer modeling technique.

Using the reverse multilayer modeling framework, it is possible to determine the electromagnetic properties of the subsurface and buried targets. Subsurface and target parameter estimation techniques based on reverse modeling will be presented in depth in Chapter 4.

Chapter 4

Subsurface and Landmine Parameter Estimation

In this chapter, the estimation of subsurface ground and buried target characteristic parameters is considered. These parameters include the composite electric field reflected from a given interface, reflection coefficient of an interface, intrinsic impedance and relative permittivity of each medium.

Section 4.1 motivates the need and usage of GPR based subsurface and target parameters estimation. The signal model is given in Section 4.2 and the basics of surface reflection method, which is the main contribution of this chapter, is detailed in Section 4.3. Real data analysis results of the parameter estimation approach are shown in Section 4.4 whereas Section 4.5 provides discussion on the real data analysis results. Section 4.6 presents the conclusions about the parameter estimation and the real data analysis results.

4.1 Motivation

Clutter reduction is a vital but challenging task in impulse GPR based landmine detection. Existing clutter reduction techniques are mainly based on the application of background subtraction and advanced signal processing techniques. It is also possible to classify targets and subsurface clutter depending on their EM properties. Subsurface and target parameter estimation based on inverse multilayer modeling is an alternative approach for the discrimination of target and clutter. These parameters are mainly the intrinsic impedance and relative permittivity.

4.2 Signal Model

It is difficult to define a complete, physically motivated signal model of the GPR backscattered waveform. However, based on extensive data analysis and basics of EM

wave propagation, a multilayer modeling approach as it has been defined in Chapter 3 is given as follows:

$$\mathbf{y}(t,x) = \mathbf{s}_c(t,x) + \sum_{m=-M}^{M} \sum_{k=1}^{N_l} \mathbf{w}(m) a_k(x) \delta(t - t_k(x)) + \mathbf{s}_n(t,x) \tag{4.1}$$

where $t = 1, 2, \ldots, N$, $x \in \mathbb{Z}^+$ is the antenna position, k represents the number of interfaces including air-ground, a_k and t_k are the amplitude and the two-way travel time of the k^{th} echo, respectively. The inverse modeling is based on the determination of the echo function, i.e., determination of the amount of electric field (voltage) reflected from an interface and the time taken by the echo signal to return.

4.3 Surface Reflection Method

Numerical inversion of any geophysical data is basically an iterative process where a multilayer model is fitted to the data. The parameters are adjusted until an acceptable fit between the model and the data is achieved. The greater the number of parameters involved in the inversion, the more complex the inversion process will be. Since some GPR parameters are interrelated, a unique solution cannot be obtained. Due to the involvement of a large number of parameters, the use of typical values for a given material's parameters and some assumptions can simplify the estimation.

We analyze the surface reflection method to retrieve the EM properties of the soil subsurface and shallowly buried targets from GPR measurements. The surface reflection method is an inverse multilayer modeling approach applied to an air-coupled GPR configuration. It is based on the determination of the echo function and using these echo functions to estimate the reflection coefficients of the layer interfaces [75, 81, 82]. The following assumptions are particularly considered in the analysis.

1. The antenna set is located in free space at some height above the ground.
2. The reflection coefficient can be approximated by the plane wave reflection coefficient.
3. Antenna distortion effects are considered to be negligible.
4. The soil is considered to be lossless, that is, the soil electric conductivity is assumed to be negligible.

5. The magnetic permeability of the soil and the targets is assumed to be the same as free space permeability.

6. The dielectric permittivity is considered to be frequency independent.

As a result of the above assumptions, the reflection coefficient at the interfaces is Dirac's delta function of time and amplitude. It is defined as a ratio of the backscattered, (E_r), to the incident, (E_i), electric fields. The reflection coefficient of an interface between two media is calculated as the ratio of amplitudes of the echo to the incident signal. Other parameters of the subsurface are determined using the reflection coefficients.

The parameters, which represent the subsurface layers, are many in number. However, they can be reduced by eliminating some parameters from consideration in the inversion or by determining some parameters in advance by other means. If some parameters are known or assumed for the subsurface model, they can be fixed or constrained during the inversion, thereby the inversion process will be simplified. Parameters can be independently determined by laboratory testing and is also possible to use average values of some subsurface parameters to simplify the inversion.

DC Offset Removal

The first step in subsurface parameter estimation is removing the DC offset or dewowing. It is a process of removing the DC bias or the low frequency signal component that present in the data. Because of the large energy input from the airwave, ground wave, and near surface reflectors or inductive coupling effects, the GPR receiver becomes signal saturated and unable to adjust fast enough to the large variations between vertical stacks [17, 83]. This induces a low frequency and slowly decaying "wow" on the higher frequencies of the signal trace arrivals. DC signal saturation is constant across each trace.

DC offset removal is an important process to ensure that the mean value of the A-scan is near zero. It can be corrected by subtracting the temporal mean value from each trace [5, 17]. The offset reduced trace has a magnitude distribution symmetric about the mean value [16].

$$\mathbf{u}(t,x) = \mathbf{y}(t,x) - \frac{1}{N}\sum_{t=1}^{N}\mathbf{y}(t,x) \tag{4.2}$$

where $\mathbf{y}(t,x)$ is the measured A-scan at the horizontal position x and N is the maximum number of sample points.

4.3.1 Basics of Parameter Estimation

The absolute peak amplitude, $E_{p1} = |E_{r1}|$, and peak time, t_{p1}, are measured and recorded in the time range of $0 < t \leq t^* + t_{off} + \tau/2$, where t^* is the arrival time of the first layer that is calculated using the general antenna height information, $\tau = 1/4\pi f_c$ is the antenna pulse width and t_{off} is a zero-offset or ground-offset time. Zero-offset is the time taken by the pulse to bias the internal electronics of the antenna set. It is the time shift measured between the zero start and the ground zero during recording. The time values $t^* + t_{off}$ can be estimated by measuring the peak time of an A-scan that is calculated as the average of the first N target free A-scans.

The reflection coefficient of the air-ground interface is estimated by taking the ratio of the peak value of measured A-scan to the incident pulse. A composite signal, E_{r1}, which represents the echo reflected from the first interface as shown in Figures 4.1 and 4.2, is modeled using the convolution function given in Equation (4.1). The modeled background signal is then subtracted from each A-scan after two modifications. The amplitude of the background signal is scaled, and then a time shift is introduced so that the highest and lowest peaks overlap. Composite return signal modeling and parameter estimation of the next interfaces follow the same steps as the first interface.

In this procedure we consider two layers, where the first layer corresponds to the ground soil and the second layer corresponds to landmine or mine-like targets. A third layer can be introduced depending on the residue of the difference between the two-layer model and measured return signals. The residue is compared against a threshold, and the third layer is introduced, if the amplitude of the residue is greater than the threshold.

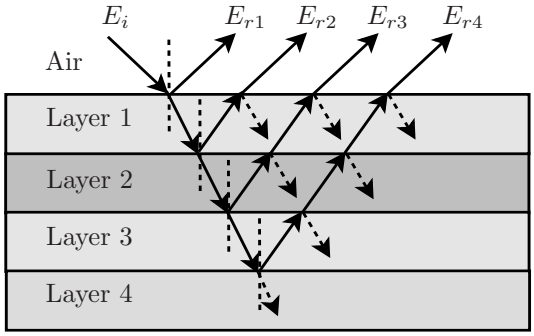

Figure 4.1. Reflections from lossless shallow subsurface layers [77].

The reflection strength of a boundary is measured as a ratio of the reflected electric field to the incident electric field. It is also represented as a function of the impedances

of the adjacent media. Figure 4.1 shows the reflection and transmission of an EM wave from lossless shallow subsurface layers. The composite return signals from the subsurface interfaces are related to the incident signal as:

$$\begin{aligned} \left|\frac{E_{r1}}{E_i}\right| &= \Gamma_{0,1} \\ \left|\frac{E_{r2}}{E_i}\right| &= T_{0,1}\Gamma_{1,2}T_{1,0} \\ &\vdots \\ \left|\frac{E_{rn}}{E_i}\right| &= \Gamma_{n-1,n}\prod_{i=1}^{n-1} T_{i-1,i}T_{i,i-1},\ n \geq 2 \end{aligned} \tag{4.3}$$

where E_{rn} is the composite signal reflected from the boundary of the $(n-1)^{th}$ and n^{th} layers as shown in Figure 4.1., E_i is the incident electric field, $T_{i,j}$ is the transmission coefficient through $(i-j)$ interface and $\Gamma_{i,j}$ is the reflection coefficient from $(i-j)$ interface.

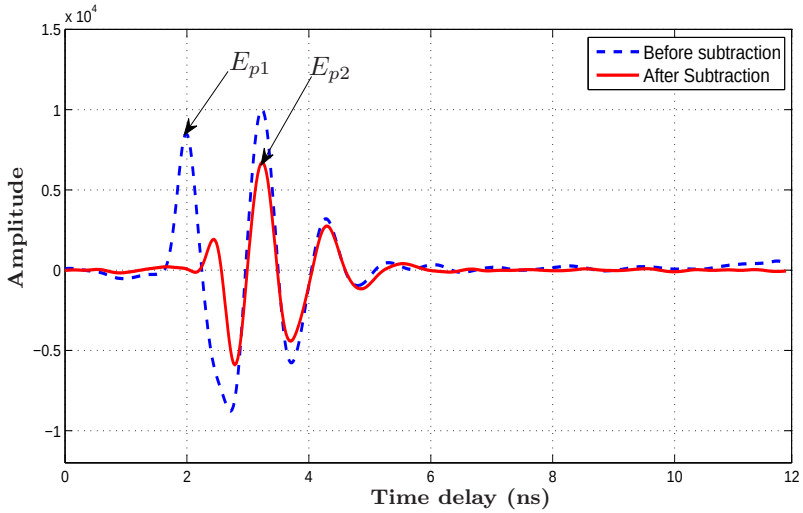

Figure 4.2. Measured A-scan(dash line), background reduced A-scan (solid line), E_{p1} and E_{p2} are peak values of the first and second interface reflections.

4.3.2 Antenna Height Estimation

The first interface reflection echoes are analyzed to provide estimations of the antenna height and reflection coefficient of the air-ground interface. In GPR measurement, the antenna should generally be close to the ground surface in order to reduce air-ground interface reflections [21]. But, for obvious reasons, this is not a feasible solution for

landmine detection applications since surface lying mines may explode in proximity or on contact. For landmine detection applications, GPR usually scans 0.5 to 5 cm above the ground [9].

The antenna height $\hat{h}_a$ at antenna position x is estimated as a product of the velocity of the EM wave in air and arrival time of the ground surface.

$$\hat{h}_a(x) = c \times \frac{t_{p1}(x)}{2} \tag{4.4}$$

where $t_{p1}(x)$ is the two-way travel time of the first interface and c is the velocity of an EM wave in free space. The arrival time is half of the two-way travel time, and the two-way travel time is calculated as:

$$t_{p1}(x) = \arg\max_t |\mathbf{u}(t,x)|\,,\ 0 \le t \le t^* + \frac{\tau}{2} + t_{off} \tag{4.5}$$

The pulse echo reflected from the air-ground interface is obtained from the A-scan evaluated at the two-way travel time of the first interface.

$$E_{p1}(x) = \mathbf{u}(t,x)|_{t=t_{p1}(x)} \tag{4.6}$$

4.3.3 Soil Characteristics Estimation

According to the Fresnel equations, the reflection coefficient (Γ) expresses the relationship between the reflected and incident energy of a plane wave. The reflection coefficient at the interface of free space and a different medium can be expressed as a function of the intrinsic impedance of air (η_0) and the first medium (η_1), as discussed in Chapter 3.

Assuming a normally incident plane wave on a planar interface and lossless medium, the air-ground reflection coefficient is calculated as a voltage ratio of the first peak of an A-scan to the incident [23, 71, 81, 82]. The air-ground reflection coefficient is always negative and is estimated using the following relationship.

$$\hat{\Gamma}_{0,1}(x) = \frac{\eta_1(x) - \eta_0}{\eta_1(x) + \eta_0} = -\frac{E_{p1}(x)}{|E_i|} \tag{4.7}$$

The intrinsic impedance of air is known to be $\sqrt{\mu_0/\varepsilon_0} = 376.82\ \Omega$ and from Equation (4.7), the intrinsic impedance of the first layer is estimated as:

$$\hat{\eta}_1(x) = \eta_0 \left(\frac{1 + \hat{\Gamma}_{0,1}(x)}{1 - \hat{\Gamma}_{0,1}(x)} \right) \tag{4.8}$$

The relative permittivity of the ground surface is estimated from the intrinsic impedance of the medium as:

$$\hat{\varepsilon}_{1r}(x) = \left(\frac{\eta_0}{\hat{\eta}_1(x)}\right)^2 + \frac{j\sigma_1(x)}{\omega\varepsilon_0} \tag{4.9}$$

where $\omega = 2\pi f_c$ is the angular frequency and σ_1 is the conductivity of the ground surface. If the ground surface is assumed to be lossless ($\sigma_1 = 0$), the relative permittivity of the medium will be real valued and frequency independent.

$$\hat{\varepsilon}_{r1}(x) = \left(\frac{\eta_0}{\hat{\eta}_1(x)}\right)^2 = \left(\frac{1-\hat{\Gamma}_{0,1}(x)}{1+\hat{\Gamma}_{0,1}(x)}\right)^2 \tag{4.10}$$

Estimation of the reflection coefficient of the air-ground interface and the arrival time of the ground surface enables to estimate the composite signal reflected from the first interface.

$$\hat{\mathbf{E}}_{r1}(t,x) = \sum_{m=-M}^{M} \mathbf{w}(m)\hat{P}_{tr}(1,x)\delta(t - t_{p1}(x) - m) \tag{4.11}$$

where $\hat{P}_{tr}(1,x) = \hat{\Gamma}_{0,1}(x)$ is the magnitude of the pulse echo from the first interface and $\mathbf{w}(m)$ is the driving wavelet function.

4.3.4 Target Characteristics Estimation

The second layer or target parameters are estimated using the residue of the composite signal reflected from the first interface. The composite reflected echo and the two-way travel time of the second interface are estimated as the peak value and peak time of the residue signal as:

$$\hat{E}_{p2}(x) = \max_t \left| u(t,x) - \nu_k(x)\hat{E}_{r1}(t - t_k(x), x) \right| \tag{4.12}$$

$$\hat{t}_{p2}(x) = \arg\max_t \left| u(t,x) - \nu_k(x)\hat{E}_{r1}(t - t_k(x), x) \right| \tag{4.13}$$

where $\nu_k(x) = E_{p1}(x)/|\hat{E}_{r1}(t,x)|$ is the scaling introduced at position x, $t_k(x) = \hat{t}_{p1}(x) - t_{p1}(x)$ is the time shift between the measured A-scan and the estimated A-scan, and $\hat{t}_{p1}(x)$ is the peak time of $\hat{E}_{r1}(t,x)$. The purpose of introducing the scaling and shifting is to correct the changes that occur during the convolution operation.

The thickness of the first layer or equivalently the depth of the target is estimated using the difference in arrival times of the two interfaces and velocity of the EM wave in the first layer as:

$$\hat{d}_2(x) = \frac{c}{\sqrt{\hat{\varepsilon}_1(x)}} \left(\frac{\hat{t}_{p2}(x) - \hat{t}_{p1}(x)}{2} \right) \tag{4.14}$$

The composite signal reflected from the second layer is the product of the incident voltage, transmission coefficient of the first interface, reflection coefficient of the second interface and transmission coefficient of the ground-air interface.

$$\frac{E_{p1}(x)}{\hat{E}_{p2}(x)} = \frac{\hat{\Gamma}_{0,1}(x)}{\hat{T}_{0,1}(x)\hat{\Gamma}_{1,2}(x)\hat{T}_{1,0}(x)} \tag{4.15}$$

where $\hat{T}_{0,1}$ and $\hat{T}_{1,0}$ are the estimated transmission coefficients from air to ground and from ground back to the air, respectively. The values of the transmission coefficients are determined using the Fresnel equations as:

$$\hat{T}_{0,1} = 1 + \hat{\Gamma}_{0,1} \text{ and } \hat{T}_{1,0} = 1 - \hat{\Gamma}_{0,1} \tag{4.16}$$

Reflection coefficient of the ground-target interface is estimated using Equations (4.15) and (4.16) as:

$$\hat{\Gamma}_{1,2}(x) = \hat{E}_{p12}(x) \left(\frac{\hat{\Gamma}_{0,1}(x)}{1 - (\hat{\Gamma}_{0,1})^2} \right) \tag{4.17}$$

where $\hat{E}_{p12}(x) = \hat{E}_{p2}(x)/E_{p1}(x)$ is the ratio of peaks of the composite signals reflected from the second interface to the first interface. The intrinsic impedance of the second layer is estimated using the reflection coefficient of the ground-target interface and the intrinsic impedance of the ground layer as:

$$\hat{\eta}_2(x) = \hat{\eta}_1(x) \left(\frac{\hat{E}_{p12}(x)(\hat{\eta}_1^2(x) - \eta_0^2) + 4\eta_0\hat{\eta}_1(x)}{\hat{E}_{p12}(x)(\hat{\eta}_1^2(x) - \eta_0^2) - 4\eta_0\hat{\eta}_1(x)} \right) \tag{4.18}$$

The relative permittivity of the second layer is determined either from the reflection coefficient of the ground-target interface or using the impedance value of the second layer.

$$\hat{\varepsilon}_{r2}(x) = \left(\frac{\eta_0}{\hat{\eta}_2(x)} \right)^2 + \frac{j\sigma_2(x)}{\omega\varepsilon_0} \tag{4.19}$$

where σ_2 is the conductivity of the second layer. If the buried target in the subsurface is assumed to be lossless or $\sigma_2/\omega\varepsilon_0$ is negligible, the relative permittivity given in Equation (4.19) could be simplified further to a real and frequency independent value.

$$\hat{\varepsilon}_{r2}(x) \approx \left(\frac{\eta_0}{\hat{\eta}_2(x)} \right)^2 = \hat{\varepsilon}_{r1}(x) \left(\frac{1 - \hat{\Gamma}_{1,2}(x)}{1 + \hat{\Gamma}_{1,2}(x)} \right)^2 \tag{4.20}$$

The composite signal reflected from the second interface is estimated in a similar way to the first interface and is given by:

$$\hat{\mathbf{E}}_{r2}(t,x) = \sum_{m=-M}^{M} \mathbf{w}(m)\hat{P}_{tr}(2,x)\delta(t-\hat{t}_{p2}(x)-m) \tag{4.21}$$

where $\hat{P}_{tr}(2,x) = \hat{\Gamma}_{1,2}(x)\hat{T}_{0,1}(x)\hat{T}_{1,0}(x)$ is the magnitude of the pulse echo reflected from the second interface.

4.3.5 Modeling Backscattered Signal

In a two-layer model assumption, the necessary parameters for signal reconstruction are the transmission-reflection products and the arrival times of each layer as estimated in Sections 4.3.2 through 4.3.4. The backscattered GPR signal from the first and the second interfaces can be estimated using Equation (4.1) and considering only two layers. The estimation of an A-scan for time $0 \leq t < \infty$ and at antenna position x is given by:

$$\hat{\mathbf{u}}(t,x) = \hat{\mathbf{E}}_{r1}(t,x) + \hat{\mathbf{E}}_{r2}(t,x) = \sum_{m=-M}^{M}\sum_{n=1}^{2} \mathbf{w}(m)\hat{P}_{tr}(n,x)\delta(t-\hat{t}_{p,n}(x)-m) \tag{4.22}$$

For the n layer case, where $n \geq 2$, the transmission-reflection product is given by:

$$\hat{P}_{tr}(n,x) = \hat{\Gamma}_{n-1,n}(x)\prod_{i=1}^{n-1}\hat{T}_{i-1,i}(x)\hat{T}_{i,i-1}(x),\ n \geq 2 \tag{4.23}$$

4.3.6 Estimation Errors

Every estimation involves an error arising from the simple fact that the quantity to be estimated generally differs from the measured values. The estimation errors result mainly from the assumptions considered during the estimation procedure, such as the consideration of only two subsurface layers, and the lossless supposition of the subsurface layers and the targets. The model error is calculated as the difference between the measured and estimated backscattered signals and is written as:

$$\mathbf{u}_e(t,x) = \mathbf{u}(t,x) - \hat{\mathbf{u}}(t,x) \tag{4.24}$$

The introduction of a third layer allows for minimizing the modeling error and estimation of the parameters of deeply buried targets. A third layer is introduced based on the magnitude of the estimation error, that is, if the test statistic of the residue is greater than a threshold. The threshold can be determined from the target-free measurements of the second layer. This suggests a test statistic which is given as:

$$T_{me}(x) = \max_t |\mathbf{u}(t,x) - \hat{\mathbf{u}}(t,x)| \tag{4.25}$$

Following the introduction of the third layer, the model in Equation (4.22) will be modified in the same procedure as the second layer. The three-layer model requires the determination of the reflected electric field $\hat{E}_{p3}(x)$, two-way travel time $\hat{t}_{p3}(x)$ and reflection coefficient, $\hat{\Gamma}_{2,3}(x)$, of the third interface. These quantities are determined from the residue of the difference between the measurement and the two-layer model in a similar procedure to the first and the second layers.

4.4 Real Data Analysis Results

We have examined the proposed subsurface parameter estimation techniques for several scenarios, however, only two cases are presented here. In the first case, we considered a setup in the presence of two plastic landmines, PMN1 and PMN2, buried in wet sand soil. The parameter estimation technique was applied to the measured radargram and the analysis results are shown in Figure 4.3. The second setup considered the presence of a rock of the same size as PMN1 and a plastic landmine, PMN2, buried in wet sand soil. Analysis results for the second setup are depicted in Figure 4.4. A two-layer and three-layer parameter estimation techniques were implemented for the first setup. Comparison of the estimated A-scans against measured data, and estimation errors under target present and target free scenarios are given in Figure 4.5. Other setups and their analysis results are shown in Appendix A.

4.5 Interpretation and Discussion

- **Peak amplitude:** For electric field to be reflected from an interface of any two media, there must be a dielectric contrast between the two media. Moreover, the

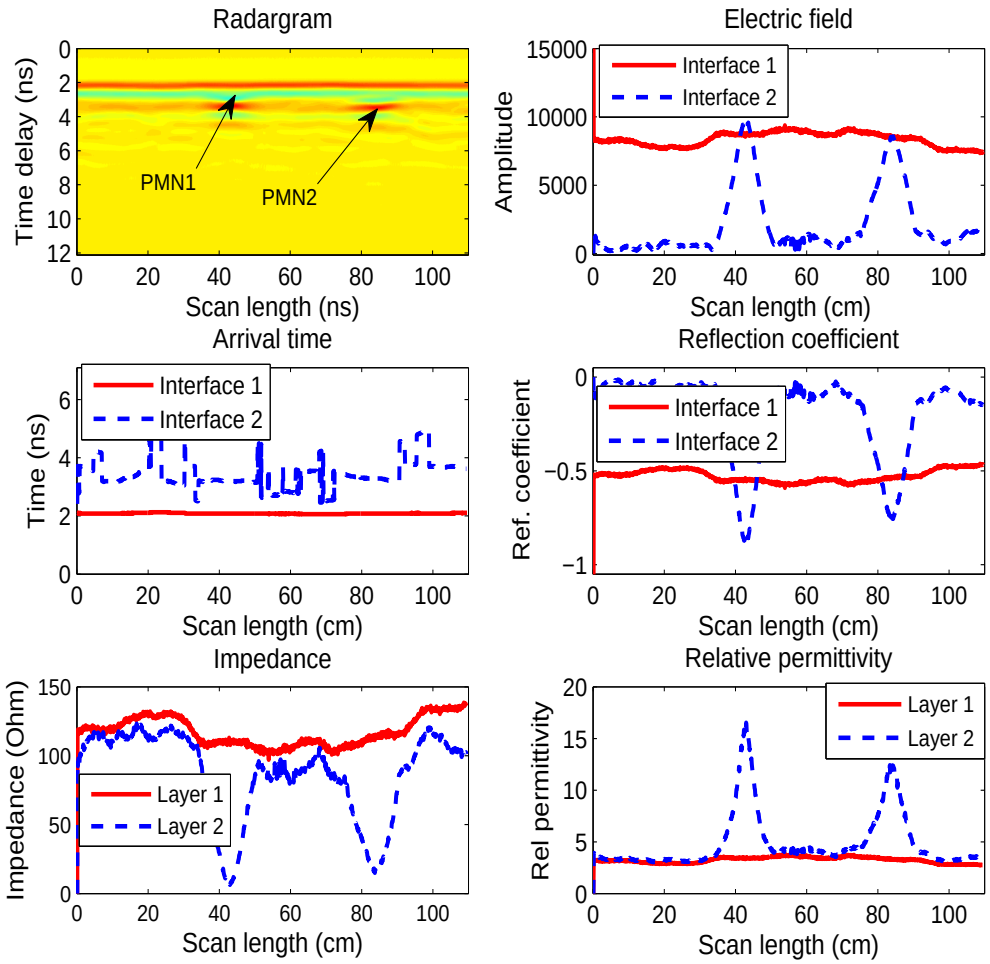

Figure 4.3. Two targets, PMN1 5and PMN2, placed in 1and soil and estimated parameters: ground layer (solid line) and target layer (dash line)

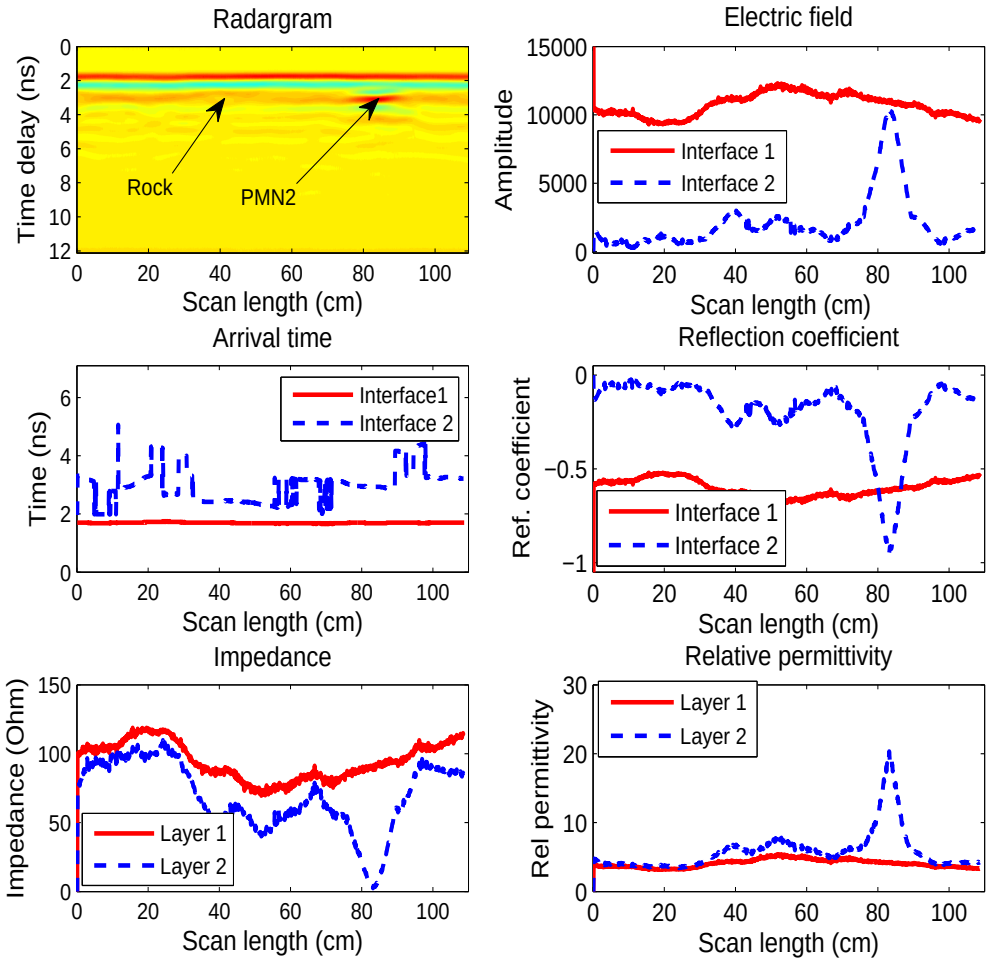

Figure 4.4. Two targets, a rock and PMN2, placed in sand soil and estimated parameters: ground layer (solid line) and target layer (dash line).

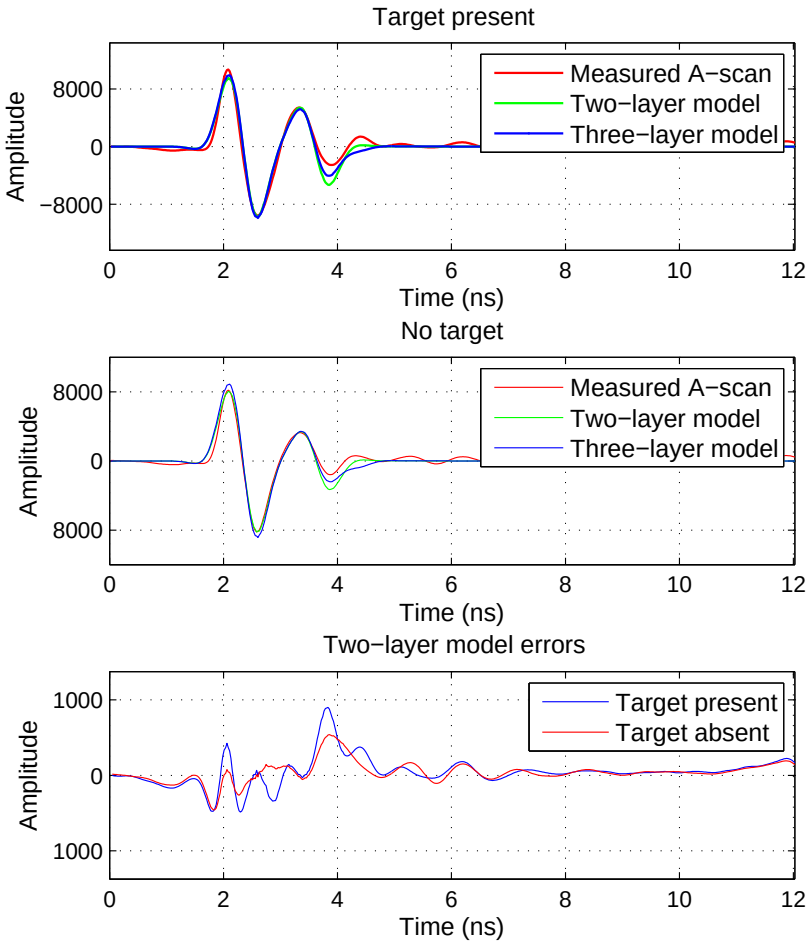

Figure 4.5. Top: target present A-scans of measured, two-layer and three-layer estimations. Middle: ground only A-scans of measured, two-layer and three-layer estimations. Bottom: two-layer model estimation error under target present and target absent.

amplitude of the reflected electromagnetic energy from the boundary is directly proportional to the difference in dielectric constant of the two media. The electric field reflected from the ground-target interface will be nearly zero when there is no buried target and the reflections are caused by the inhomogeneity of the background soil as shown in Figures 4.3 and 4.4.

- **Arrival time:** The arrival time of smooth surface is nearly constant. However, if the arrival time of the first interface is varying, either the ground surface is rough or there are surface-lying targets. The arrival time of the second layer is smooth under the presence of a buried target, while it is fluctuating under the inhomogeneity and scatterers. An overlap between the arrival times of the first and second layers indicates the presence of surface-lying targets. However, being well separated indicates the absence surface lying targets. Very long arrival time of the second layer indicates that the reflection is not due the presence of landmine, as AP mines are buried shallowly in the top 10 cm and AT mines in the top 30 cm of the ground soil [7, 10, 13]. The estimated arrival time of both layers is the summation of the true arrival time and zero-offset time. Zero-offset is the time-zero position or the start time of the ground surface position.

- **Reflection coefficient:** The reflection coefficient of the first interface being nearly uniform indicates that the top layer of the ground surface is homogeneous and that there are no surface-lying targets. However, if the variation is large enough, the ground is inhomogeneous or there may be surface-lying targets.

  The positive reflection coefficient implies the presence of an air filled void in the dielectric medium or a highly nonconducting and low relative permittivity material. Since the impedance of the ground is lower than that of the air medium, the reflection coefficient of the air-ground interface is always negative [16].

- **Impedance:** The difference in impedance of two adjacent layers causes an electromagnetic field to reflect from the interface. When the impedance of the second layer is greater than the first, the reflection coefficient will be positive. However, closely equal impedance corresponds to a low reflection coefficient or a low-amplitude reflected electric field. In general, having equal impedance indicates absence of a buried target.

- **Permittivity:** Subsurface materials are best characterized by their electric permittivity and magnetic permeability than that of electric conductivity [82, 84]. It is difficult to know the proportion of the components, especially the permittivity or conductivity, which make up the impedance. Assuming the subsurface layers to be lossless simplifies the problem greatly and it is possible to estimate the value

of permittivity uniquely.The relative permittivity of dry subsurface materials, ε_r, ranges between 3 and 6. The relative permittivity is always greater than one and the ε_r value of the second layer away from the subsurface ground indicates the presence of a target. Common explosives, such as TNT, RDX and Comp-B have relative permittivity ranging between 2.7 and 3.14, however, explosives like ammonium nitrate and nitroglycerin have values 7.10 and 19.00, respectively [10].

4.6 Conclusion

In this chapter, inverse model based parameter estimation and plastic landmine detection scheme have been considered. The proposed estimation method is useful to correctly estimate the parameters of the subsurface and buried landmines. There are many variables involved in the inversion of full wave GPR data. The procedure is unmanageable without making certain assumptions. If the soil is relatively iron-free then the magnetic permeability can be assigned a fixed value.

The effectiveness of the proposed methods is checked by using real data analysis of different scenarios. Prior knowledge of antenna height and amplitude of the incident voltage/electric field could greatly simplify the problem of parameter estimation. Moreover, for known soil characteristics, the nature of buried plastic landmines could be estimated perfectly. By considering more than two layers and using the same technique, the modeling error can be reduced greatly.

Chapter 5

Advanced Signal Processing Techniques for Landmine Detection

In this chapter, advanced signal processing techniques for clutter reduction and target detection is considered. The aim is to reduce or completely remove the clutter components that hide the target signal in GPR measurements. Clutter reduction allows to improve the detection capacity of the sensor by suppressing the unwanted signal components and enhancing the target signal.

Section 5.1 gives brief introduction and motivates the need and usage of clutter reduction in GPR based landmine detection. Section 5.2 presents the general signal modeling whereas Section 5.3 details different preprocessing techniques which are applied for signal conditioning purposes. The existing signal processing techniques are reviewed in Section 5.4. Section 5.5 presents the proposed signal processing techniques for clutter reduction, which are the main contributions of this chapter. Section 5.6 provides the comparison of the proposed techniques and draws the conclusions.

5.1 Introduction and Motivation

GPR is one of the most promising sensors for detecting and locating buried targets such as landmines, pipes, cables and tunnels. Its ability to detect nonmetallic targets makes it the best alternative for landmine detection applications. Because of military and civil engineering practical demands, GPR has found many applications in relation to exploring near-surface targets.

Not all waveforms collected by the GPR are due to subsurface reflections. Especially, in the case of an unshielded antennas, reflections may be collected from nearby above ground objects. These reflections generally produce high-amplitude unwanted reflections that are termed clutter. In complex environmental conditions, weak signals received from targets are normally obscured by strong background clutter. The presence of clutter is the most significant limitation on the practical applications of GPRs [16, 21, 53, 55, 85].

In GPR based landmine detection, there are mainly four clutter components, namely, antenna crosstalk, reflection from the air-ground interface, additive noise, and the scattered signal from mine-like objects and ground anomalies [32,85]. Antenna cross-talk is a quasi-stationary signal component caused by a direct wave measurement from transmitter to receiver antenna [21]. The additive noise may arise due to the interference of electromagnetic devices, mobile phone waves, radio transmission and television antennas, and electromagnetic wave carrying cables. The scattered signal components come from mine-like objects and ground anomalies such as tree roots, stones, air gaps and reflections resulting from scatterers within the soil.

Clutter reduction is a vital process for GPR based plastic landmine detection. Two of the clutter components, antenna crosstalk and additive noise, can be removed or significantly reduced by proper system design or easy signal processing. For example, the signal to noise ratio (SNR) can be improved by $10 \times \log_{10} M$ dB by averaging M consecutive A-scans [16, 17, 21]. Furthermore, the antenna crosstalk can be eliminated by time window gating [21, 32]. There are many effective signal processing techniques for clutter reduction. Unless these clutter components are removed, GPR becomes ineffective and it suffers from high false alarm rates. The aim of clutter reduction techniques is to suppress the clutter components and enhance the target signal.

5.2 Signal Modeling

The backscattered signal measured by the receiver antenna of a GPR system has four major components. These are the antenna crosstalk, additive process and measurement noise, reflections from the air-ground interface and the signal reflected from a buried target.

The most basic model depicted in Figure 5.1 can be represented analytically as a summation of the the four signal components.

$$\mathbf{y}(t,x) = \mathbf{s}_t(t,x) + \mathbf{s}_b(t,x) + \mathbf{s}_c(t,x) + \mathbf{s}_n(t,x),\ 0 \leq t < \infty,\ 0 \leq x < \infty \tag{5.1}$$

where $\mathbf{y}(t,x)$ is the return GPR signal measured at discrete time t and antenna position x, $\mathbf{s}_t(t,x)$ is the signal component returned from the target, $\mathbf{s}_b(t,x)$ is the background signal, $\mathbf{s}_c(t,x)$ is antenna cross-coupling and $\mathbf{s}_n(t,x)$ is additive noise.

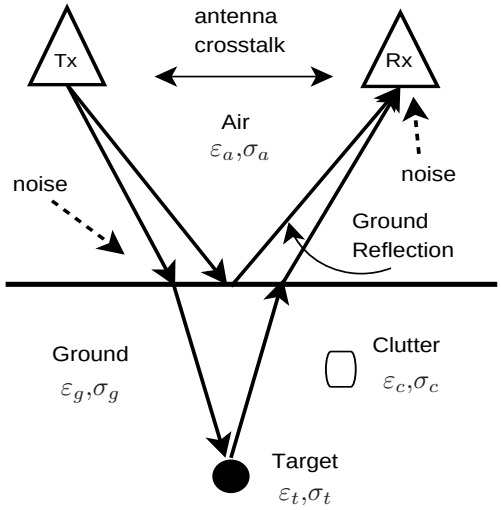

Figure 5.1. Typical GPR transmitter - receiver configuration model for target detection.

5.3 Preprocessing Techniques

Preprocessing techniques are elementary signal processing methods applied to simplify the interpretation of the GPR data. The main purpose of the preprocessors is for signal conditioning and data correction. These techniques include DC-offset removal, time-zero correction, noise reduction and antenna crosstalk removal. DC-offset removal techniques have already been discussed in Section 4.3.

5.3.1 Time-zero Correction

Thermal drift, electronic instability, cable length differences and variations in antenna air-gap can cause 'jumps' in the first arrival-time of the return signal. This is referred to as time-zero offset [17, 43, 60]. The process of setting the zero-time with the zero-depth needs to be done before interpretation of the radar image. This is an essential factor for conducting accurate shallow depth measurements in GPR. The first negative peak minus half of the pulse width may be considered to calculate the time-zero point [17, 21] and the corrected signal is then given by:

$$\mathbf{y}'(t, x) = \mathbf{y}(t + t_{off}, x) \tag{5.2}$$

where $\mathbf{y}'(t, x)$ is the processed signal and t_{off} is the time-zero offset.

5.3.2 Noise Reduction

Noise reduction is an important processing technique that can be achieved by either averaging each individual sample of the A-scan or storing and averaging repeated A-scans [16, 43]. The aim is to reduce the variance of the noise and to improve in signal-to-noise-ratio. The general form of the filtering operation is given by:

$$\mathbf{y}_s(t,x) = (1-\alpha_k)\mathbf{y}_s(x-1,t) + \alpha_k \mathbf{y}'(x,t),\ 0 < \alpha_k < 1 \tag{5.3}$$

where $\mathbf{y}_s(t,x)$ is the smoothed A-scan, $\mathbf{y}'(t,x)$ is the time-zero corrected A-scan and α_k is an exponential factor, where the smaller the value of α_k, the better the smoothing will be.

5.3.3 Antenna Crosstalk Removal

Because of the close configuration of the antenna set, the first pulse of the GPR return signal propagates directly from transmitter to receiver antenna. This quasi-stationary signal component is commonly called antenna crosstalk or cross-coupling [21, 32]. Bistatic high frequency GPRs are small in size and both antennas are kept in fixed geometry. For example, a 1.5 GHz antenna has a dimension of $T \times W \times L = 3.8 \times 10 \times 16.5$ cm [61].

Since both antennas are close to each other and the antenna coupling signal arrives earlier than any other signals, antenna crosstalk can be reduced or removed using time-window gating techniques [21]. As antenna crosstalk is stationary for a given antenna configuration under a given setup, it can also be removed using spatial mean or median filters [32].

5.4 Existing Clutter Reduction Techniques

The most disturbing signal component in GPR data analysis is the signal reflected from the air-ground interface. Due to the high dielectric contrast between the air and ground medium as compared to that of the mine and surrounding medium, the ground reflection is much higher in amplitude than the wanted target reflection [16]. Hence, reflections from smaller mines will be obscured by the ground clutter and noise [32]. An easy way to eliminate the air-ground interface reflection can be achieved by positioning

the antennas in direct contact with the soil so that no air-ground reflection is allowed to form [21]. But, for obvious reasons, this is not implementable for landmine detection applications.

Existing clutter reduction methods for GPR based landmine detection include background subtraction, Kalman filtering, wavelet packet decomposition, one or two sided linear prediction techniques, principal component analysis (PCA) or independent component analysis (ICA), and time-frequency analysis.

Commonly used techniques for ground clutter reduction are subtraction of the mean or median of all scans, or mean or median of A-scans along a running window [9, 27, 28]. The simple mean or median subtraction is computationally simple, but the estimate is less accurate. The windowed average or median subtraction method can be used for slowly varying ground surfaces so that slightly oblique surface reflections can be eliminated. The main disadvantage of the mean and median subtraction methods is that the target reflection will also be affected by the subtraction process. That is, the specific target scattering information, which can be used for target classification, may be lost [9, 21].

Many advanced signal processing algorithms have been examined to overcome the above disadvantages. Savelyev *et al.* presented deconvolution techniques in [16] to extract a target reflection ideally. But, for a successful application of this technique, an exact knowledge of each transfer function along the round trip from the transmitting antenna to the receiving antenna is inevitable. Deconvolution could be a useful technique for data processing even though it suffers the lack of knowledge of the transmitted signal [30].

Van Kempen in [40] and Brooks in [31] proposed an autoregressive moving average (ARMA) model for the contained clutter. In practice, the ARMA parameters of the clutter and the clutter-plus-target were so close that a meaningful target separation was not possible [30].

Zoubir *et al.* in [9] investigated the detection performances of various signal processing techniques with emphasis on a Kalman filter based approach. Compared to others, this technique showed the best overall performance. However, the cost of the Kalman filter approach shows substantial increase in the computational load.

Alvaro *et al.* in [27] applied many background subtraction techniques for their optimality. They compared the techniques based on their energy to clutter ratio. Frequency-domain scaled and shifted (SaS) background subtraction was found to be optimal for rough and smooth ground surfaces.

Dragana C. in [29] and [45] considered a Kalman filtering approach and a wavelet packet decomposition for clutter reduction applications. Yuan and Guang in [44] also considered a Kalman filtering approach to reduce the ground clutter.

5.4.1 Background Subtraction

A simple method to reduce ground clutter and detect the target is subtraction of the background estimate from the GPR return. The background signal can be estimated in several ways, such as taking the ensemble average of the GPR return, mean or median along a running window or a scaled and shifted version of arbitrary A-scans. In this method, target detection may be based on the amplitude or energy of the residual. This method assumes a simple additive signal model of the target and the background:

$$\mathbf{y}(t,x) = \eta \cdot \mathbf{s}_t(t,x) + \mathbf{s}_b(t,x) \tag{5.4}$$

The hypothesis test for the presence or absence of a target is given by:

$$\begin{aligned} H_0: &\quad \eta = 0, \quad \text{no target at position } x \\ H_1: &\quad \eta = 1, \quad \text{target present at position } x \end{aligned} \tag{5.5}$$

Under H_0, the difference between the estimate of the background signal $\hat{\mathbf{s}}_b(t,x)$ and the GPR return will be negligible. However, the difference will be considerable under the H_1 hypothesis due to the presence of a return signal from the target. This leads to test statistics which are based on the residual and are given by:

$$T_{b1}(x) = \max_t |\mathbf{y}(t,x) - \hat{\mathbf{s}}_b(t,x)| \tag{5.6}$$

$$T_{b2}(x) = \frac{1}{N} \sum_{t=1}^{N} |\mathbf{y}(t,x) - \hat{\mathbf{s}}_b(t,x)|^2 \tag{5.7}$$

The advantage of background subtraction is its simplicity and computational efficiency. The main problem with this method is to obtain a good estimate for the background signal. Most of the existing classical methods use mean or median A-scans to estimate the background signal. Here, advanced background subtraction techniques, which are based on adaptive background estimation and multilayer modeling, are presented in Section 5.5.1.

5.4.2 Kalman Filter

The Kalman filter uses a state space based approach to track the changes in the GPR return. It has two states: the first state is associated with the absence of a target, while the second state is associated with the presence of a target [9,29,44]. By using previous accumulated information, the preceding future values are predicted. Differences in the prediction may cause to update the current state which then indicates the presence or absence of a target. The Kalman filter reduces the clutter efficiently and provides an excellent detection rate, but it is computationally demanding.

5.4.3 Wavelet Packet Decomposition

Wavelet packet decomposition based target detection uses a transformation to decompose the radar return signal $\mathbf{y}(t,x)$ into a set of basis waveforms called wavelets [9,45–47]. The decomposed basis wavelet coefficients describe the return signal, $\mathbf{y}(t,x)$. Changes in these coefficients can be examined to test the presence of a target. Even though, the technique provides good results in clutter reduction, the test statistic is not well defined.

5.4.4 Matched Filter Deconvolution

In this approach, the subsurface ground is considered as a linear time invariant (LTI) channel that filters the incoming signal in some way to produce the output backscattered waveform. The received GPR return is considered as a convolution of the ground impulse response $\mathbf{h}(t,x)$ and the input signal $r(t)$

$$\mathbf{y}(t,x) = \mathbf{r}(t,x) \star \mathbf{h}(t,x) \tag{5.8}$$

where the input signal is $\mathbf{r}(t) = \delta(t)$ under no target case and $\mathbf{r}(t,x) = \delta(t) + \eta \cdot \mathbf{s}_t(t,x)$ in the presence of a target. The target signal, $\mathbf{s}_t(t)$, is obtained by deconvolving the estimate of the impulse response, $\hat{\mathbf{h}}(t,x)$, from the GPR return signal and subtracting the delta function. This method removes the clutter efficiently, but it requires complete model of the ground and the target.

5.5 Proposed Clutter Reduction Techniques

5.5.1 Advanced Background Subtraction

The backscattered signal from the subsurface ground can be easily distinguished from the target if the target is buried deep below the surface. The signals can be separated by a time gating technique [32]. Time gating is not a proper solution if the target is shallowly buried near the surface as the backscattered signals from both, the target and the surface, arrive almost simultaneously.

The simplest technique for target detection is removing the signal bounced from the air-ground interface using background subtraction techniques. The background signal is determined using background estimation techniques and the estimate is subtracted from the measured B-scan. The method assumes a signal model as given in Equation (5.4). The hypothesis testing for target presence and suggested test statistics are described in Equation (5.5) through (5.7).

In this section, we are going to present one classical and three advanced techniques for background signal estimation. The classical method is based on the application of spatial filters. The advanced techniques are based on the shifted and scaled estimation of an arbitrary A-scan, the adaptive shifted and scaled estimation of the average of N target-free A-scans and estimation based on multilayer ground and target modeling.

5.5.1.1 Running Spatial Filters

This method uses a long sliding window to process each A-scan by subtracting a mean or median of the A-scans comprised within the sliding window. The A-scan being processed is placed in the center of the sliding window. The window contains an odd, (N), numbers of A-scans.

Background signal estimation using a running average is given by:

$$\hat{\mathbf{s}}_b(t,x) = \frac{1}{N} \sum_{k=x-\frac{N-1}{2}}^{x+\frac{N-1}{2}} \mathbf{y}(t,k) \tag{5.9}$$

In a similar manner, using running median of odd window length, (M), and $m = \frac{M-1}{2}$, the background estimate is given by:

$$\hat{\mathbf{s}}_b(t,x) = \text{median}(\mathbf{y}(t,x-m), \mathbf{y}(t,x-m+1), \ldots, \mathbf{y}(t,x+m)) \tag{5.10}$$

where 'median' represents a median filtering process. Spatial filters provide very good estimation of the background signal. The main problem with spatial filters is the choice of appropriate window size. The window size should be wide enough to allow an accurate estimate to be made, with low variance, while narrow enough to avoid introducing effects from the changes in the local background characteristics [9, 41].

5.5.1.2 Shifted and Scaled Background Estimation

In this method, the background signal estimation begins with averaging N target-free A-scans and two modifications are performed before subtraction. First magnitude scaling is introduced so that the maximum and minimum values of the estimate and the current A-scan are equal. Second, a time phase-shift is introduced so that the maximum and minimum values overlap. For each A-scan, the signal correction is performed by removing the low-frequency component as discussed in Section 4.3:

$$y_{ref}(t) = \frac{1}{N}\sum_{k=1}^{N}\mathbf{u}(t,k) \tag{5.11}$$

where $\mathbf{u}(t,x)$ is a DC-offset reduced A-scan as formulated in Equation (4.2) and $y_{ref}(t)$ is an estimated reference signal. The background signal $\hat{\mathbf{s}}_b(t,x)$ is estimated as an amplitude-scaled and time-shifted version of the reference signal and is given by:

$$\hat{\mathbf{s}}_b(t,x) = r_\alpha(x)y_{ref}(t - t_\alpha(x)) \tag{5.12}$$

where $r_\alpha(x) = |\mathbf{u}(t_p(x),x)|/|y_{ref}(t_{ref})|$ is the amplitude scaling and $t_\alpha(x) = t_p(x) - t_{ref}$ is the time shift, $t_p(x) = \arg\max_t |\mathbf{u}(t,x)|$ is the absolute peak time of the current A-scan and $t_{ref} = \arg\max_t |y_{ref}(t)|$ is the peak time of the reference signal. The background subtraction is implemented by subtracting the background estimate from the DC-offset removed A-scan.

5.5.2 Multilayer Ground and Target Modeling

In this approach, the background and target signals are estimated using the inverse multilayer modeling as discussed in Chapter 4. The background signal is estimated from the first layer estimations and the target signal is obtained as a difference between the return signal and first layer signal estimations [41, 86]. The target signal can also be obtained from the second layer backscattered signal estimations.

5.5.2.1 Background Signal Modeling

The background signal is estimated based on the measurement of the peak values of the GPR return signal. In GPR electromagnetic propagation, the intensity of the signal reflected from an interface is directly proportional to the contrast between the adjacent layers. The highest contrast exists between air and ground. Correspondingly, the peak amplitude of an A-scan is usually the ground reflection [27, 41, 86]. The background signal is estimated as given in Equation (4.11).

$$\hat{\mathbf{s}}_b(t,x) = \hat{\mathbf{E}}_{r1}(t,x) \tag{5.13}$$

where $\hat{\mathbf{E}}_{r1}(t,x)$ is the composite signal reflected from the air-ground interface at horizontal position x. Background subtraction is implemented by subtracting the estimated signal from the measured signal.

5.5.2.2 Target Signal Modeling

Target signal modeling is performed right after the background estimation signal is subtracted from the GPR return signal. From the residue, we search for the peak amplitude and target arrival time as in Equations (4.12) and (4.13), in Section 4.3.5. The target signal is estimated as a convolution of the driving function and the echo function, as in Equation (4.21).

$$\hat{\mathbf{s}}_t(t,x) = \hat{\mathbf{E}}_{r2}(t,x) \tag{5.14}$$

5.5.2.3 Application for Target Detection

The problem of target detection may be formulated as a hypothesis test in order to decide whether target presence is likely or not. To construct the test, two hypotheses are formulated: the null hypothesis, H_0, states that there is no target and the alternative, H_1, states that there is a target.

The aim of the ground/target signal modeling is nothing but to improve the target detection capacity of GPR. It is possible to declare target presence based on the magnitude of the signal reflected from the ground-target interface. An EM wave radiated from GPR antenna gets reflected from the interface of two layers when the adjacent layers have different electromagnetic properties. The hypotheses test can therefore be

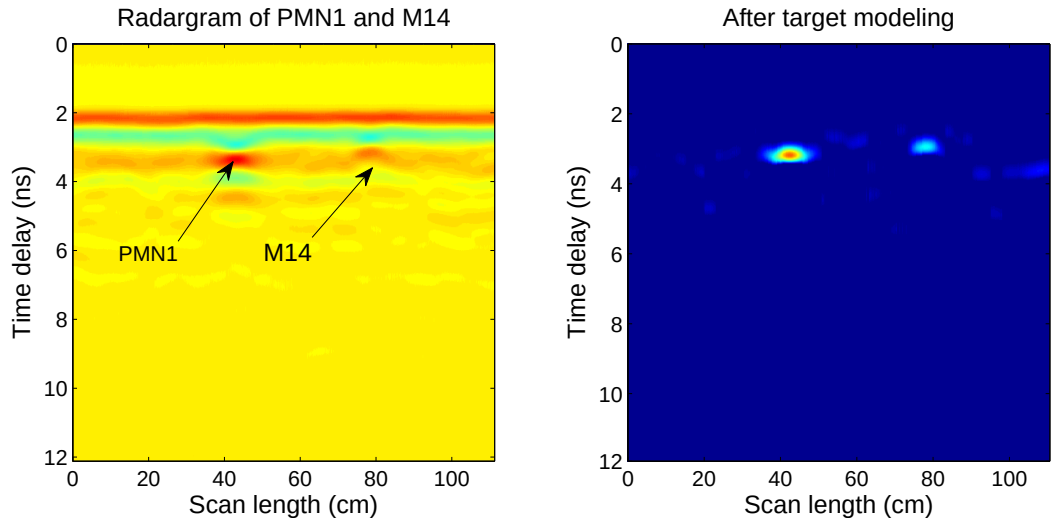

Figure 5.2. Radargram of PMN1 and M14, and radargram after target modeling.

defined depending on the amplitude the electric field reflected from the ground-target interface.

The objective is to test the significance of the reflected electric field from the second interface using amplitude detection. Under no target conditions, the amplitude of the reflected electric field is negligible. However, it is considerable when a target is present. The null hypothesis implies $H_0 : \hat{\mathbf{E}}_{r2}(t,x) = \mathbf{s}_n(t,x)$ and the alternative hypothesis implies $H_1 : \hat{\mathbf{E}}_{r2}(t,x) = \mathbf{s}_t(t,x) + \mathbf{s}_n(t,x)$. This suggests the following test statistic

$$T_{vs}(x) = \max_t \left| \hat{\mathbf{E}}_{r2}(t,x) \right| = \hat{E}_{p2}(x) \tag{5.15}$$

The null hypothesis is accepted if the test statistic $T_{vs}(x)$ is smaller than a threshold $T_{v\alpha}$, otherwise, it is rejected. The threshold $T_{v\alpha}$ is determined empirically.

$$T_{vs}(x) \underset{H_0}{\overset{H_1}{\gtrless}} T_{v\alpha} \tag{5.16}$$

Test statistic for two targets, PMN1 and M14, buried in wet sand soil is depicted in Figure 5.3

5.5.3 Adaptive Background Subtraction

The main idea of the adaptive shifted and scaled algorithm is to update the reference signal, $y_{ref}(t)$, according to the decision made on the current trace. If a test indicates that the current A-scan is target-free, the list of ground traces are updated by adding

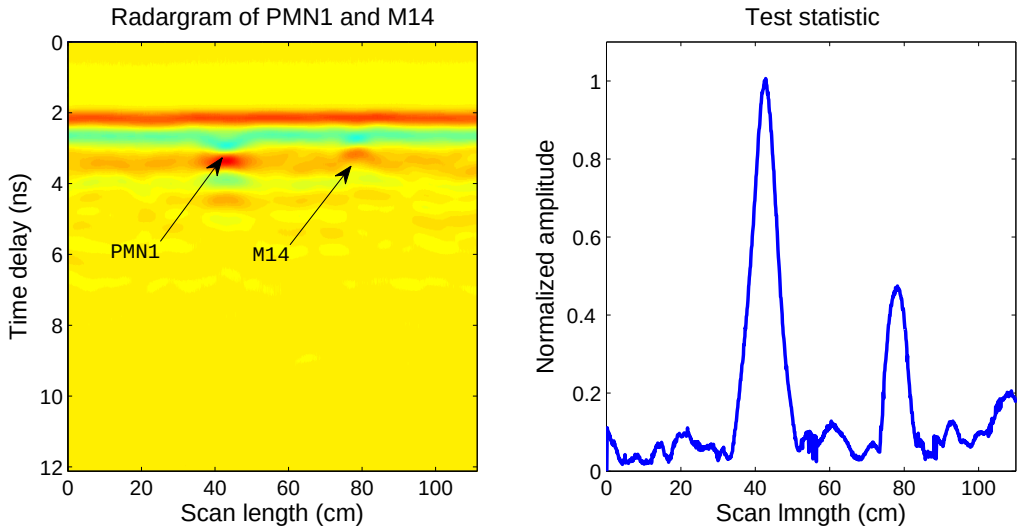

Figure 5.3. Radargram of PMN1 and M14, and test statistics based on the reflected electric field.

the current trace and removing the oldest, otherwise a presence of a target is declared and the current list of background traces will remain unchanged.

The adaptive background subtraction procedure is explained in Table 5.1.

5.5.4 Decorrelation Method

Upon the inspection of the characteristics of the real-world GPR data, it has been found that the background has strong correlation from trace to trace [16, 53]. The Karhunen-Loéve transform (KLT), which is also known as principal component analysis (PCA) is applied here to remove the correlations between the GPR traces and enhance the signal-to-noise-ratio. PCA provides a basis in which the transformed signals are decorrelated. Thus, every original signal can be represented as a weighted superposition of the eigenvectors. In general the KLT can be represented as:

$$\mathbf{X} = T\mathbf{Y} \tag{5.17}$$

where $\mathbf{Y}$ is the data matrix to be transformed, $\mathbf{T}$ is a transformation matrix and $\mathbf{X}$ is the transformation of the data matrix $\mathbf{Y}$. The transformation matrix is obtained from data matrix. Suppose the data matrix is:

$$\mathbf{Y} = (\mathbf{y}_1, \mathbf{y}_2, \cdots, \mathbf{y}_N)^T \tag{5.18}$$

Step 1. Consider K target-free A-scans and let $\mathbf{x}(t,k) = \mathbf{u}(t,k)$, for $k = 1, 2 \ldots K$ and $K \in \mathbb{Z}^+$

Step 2. Estimate a background reference A-scan as an average of the first K target-free A-scans, as given in Equation (5.11).

Step 3. Consider the current A-scan and locate the peak time $t_p(x)$, and locate the peak time of the estimated reference signal, t_{ref}

$$t_{ref} = \arg\max_t |y_{ref}(t)| \text{ and } t_p(x) = \arg\max_t |\mathbf{u}(t,x)|$$

Step 4. Introduce amplitude scaling and time shifting to the reference background signal

$$r_\alpha(x) = \left| \frac{\mathbf{u}(t_p(x), x)}{y_{ref}(t_{ref})} \right| \text{ and } t_\alpha(x) = t_p(x) - t_{ref}$$

$$\hat{\mathbf{s}}_b(t,x) = r_\alpha(x) y_{ref}(t - t_\alpha(x))$$

Step 5. Subtract the estimate from the current A-scan and compare the test statistic against a threshold to determine the presence or absence of a target.

- If H_1 is accepted, declare presence of a target and go to Step 3.
- If H_0 is accepted, update the estimator set of traces by adding the current trace and removing the oldest trace and go to Step 2.

$$\begin{aligned} \mathbf{x}(t,k) &= \mathbf{x}(t,k+1),\ k = 1, 2, \cdots, K-1 \\ \mathbf{x}(t,K) &= \mathbf{u}(t,n) \end{aligned}$$

Table 5.1. Adaptive background subtraction procedure.

then the covariance matrix is

$$\Psi_Y = E\{[\mathbf{Y} - E(\mathbf{Y})][\mathbf{Y} - E(\mathbf{Y})]^T\} \tag{5.19}$$

where $E(\mathbf{Y})$ is the mean vector of $\mathbf{Y}$. In general, Ψ_Y is a positive or semi-positive definite matrix. Suppose $\mathbf{B} = (\mathbf{v}_1, \mathbf{v}_2, \ldots, \mathbf{v}_N)$ is a unit normal eigenvector orthogonal matrix and satisfies the following relationship

$$\mathbf{B}^T \Psi_Y \mathbf{B} = \begin{bmatrix} \lambda_1 & 0 & \ldots & 0 \\ 0 & \lambda_2 & \ldots & 0 \\ \ldots & \ldots & \ldots & \ldots \\ 0 & 0 & \ldots & \lambda_N \end{bmatrix} \tag{5.20}$$

where λ_i is an eigenvalue of the covariance matrix and meets $\lambda_1 \geq \lambda_2 \geq \cdots \geq \lambda_N$. $\mathbf{v}_i$ is normal orthogonal eigenvector orthogonal to $\mathbf{v}_j$ for $i \neq j$. The eigenvector $\mathbf{v}_i$ is associated with the eigenvalue λ_i. λ_1 is the biggest eigenvalue and it represents the most correlated components among all the random variables $\mathbf{y}_i$. The smallest eigenvalue corresponds to the uncorrelated components which are often considered as random noise. The orthogonal transformation is defined as:

$$\mathbf{X} = \mathbf{B}^T \mathbf{Y} = (\mathbf{x}_1, \mathbf{x}_2, \cdots, \mathbf{x}_N)^T \tag{5.21}$$

$\mathbf{X}$ is called the Karhunen-Loéve transform of $\mathbf{Y}$.

5.5.5 Subtract and Weight Method

In this section we will present a technique to suppress the noise and background signals correlated between the traces using a subtract and weight (SaW) method. From each A-scan, the average of target-free A-scans is subtracted and the sample variance of the residue is calculated.

The mean-subtracted A-scans are weighted by the standard deviation of the residue. In this process, the ground only traces are suppressed and the target present traces are enhanced. The motivation behind this method is that when a trace is target free, the variance of the background-subtracted trace is very low. On the other hand, the variance will be high if the trace contains a target. Therefore, it is possible to suppress

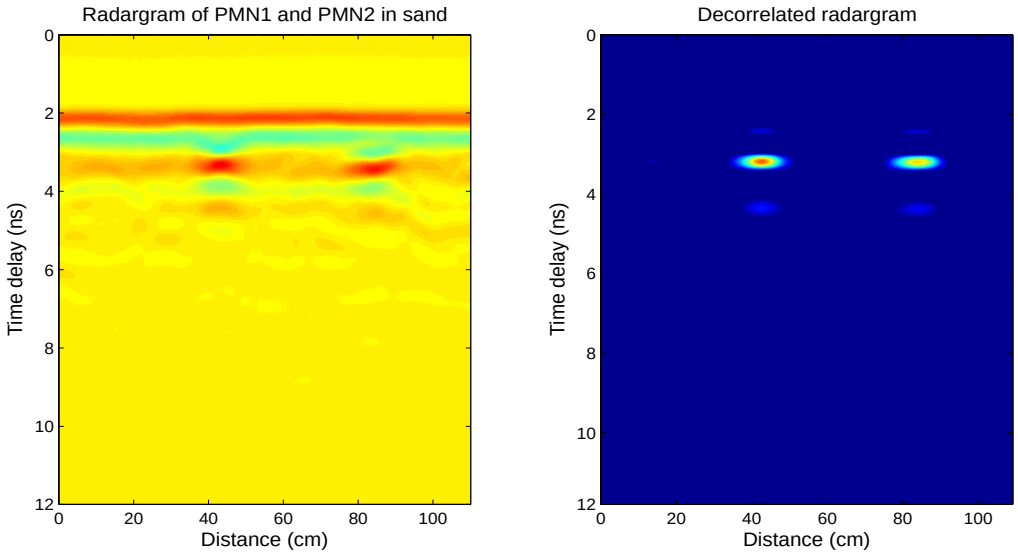

Figure 5.4. Left: raw radargram data in the presence of PMN1 and PMN2 in sand soil, Right: radargram after enhancement.

the noise and signals due to ground inhomogeneities by weighting the background-subtracted traces with the standard deviation or variance.

Let $\mathbf{y}_1(t), \mathbf{y}_2(t), \cdots, \mathbf{y}_N(t)$ be a set of N vectors of length M, N equal to the number of traces for background signal estimation. Then the sample mean vector μ_y is given by:

$$\mu_{\mathbf{y}}(t) = \frac{1}{N} \sum_{i=1}^{N} \mathbf{y}_i(t) \tag{5.22}$$

and the sample variance $\sigma_{\mathbf{y}}^2$ is given by:

$$\sigma_i^2 = \frac{1}{M} \sum_{j=1}^{M} (\mathbf{y}_i(t) - \mu_{\mathbf{y}}(t))^2 \tag{5.23}$$

The signal vector with enhanced signal-to-noise-ratio is given by:

$$\mathbf{z}_i(t) = \sigma_i^2 \left(\mathbf{y}_i(t) - \mu_{\mathbf{y}}(t)\right) \tag{5.24}$$

The set of vectors $\mathbf{z}_1, \mathbf{z}_2, \cdots, \mathbf{z}_M$ contain elements with high SNR.

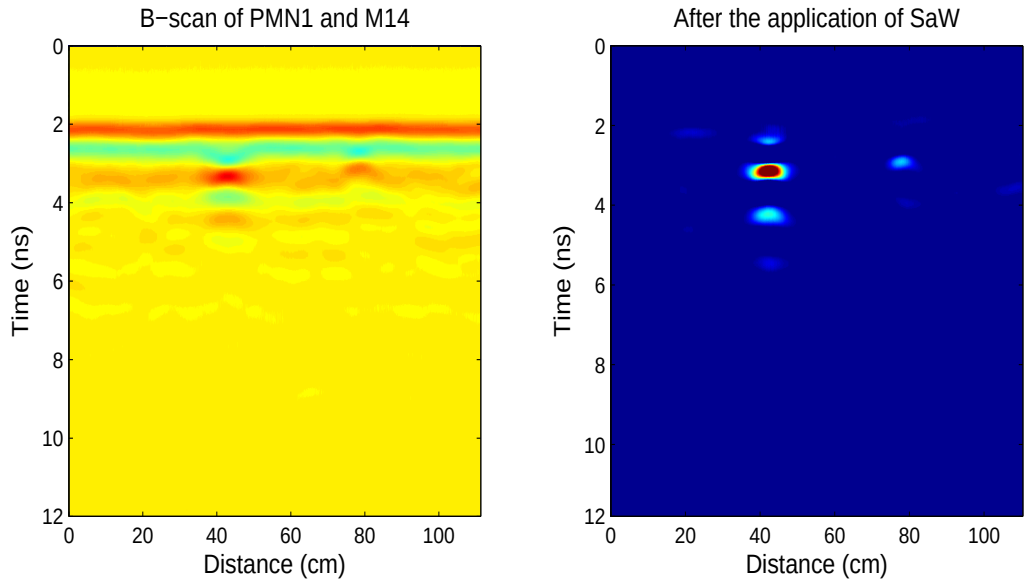

Figure 5.5. Left: raw radargram data in the presence of PMN1 and M14 in sand soil, Right: radargram after the application of SaW.

5.5.6 Symmetry Filtering Algorithm

Most of the clutter reduction techniques discussed in the previous sections can reduce or completely remove three of the clutter components. However, they can not distinguish landmines from mine-like objects and scatterers in the ground. The aim of this algorithm is to reduce the random clutter due to the external anomalies based on their geometry. Moreover, the symmetry filtering approach is employed to suppress the signatures from asymmetrical objects and enhances the signatures from symmetric objects.

Elementary preprocessing techniques are applied to reduce the stationary clutter components and symmetry filtering is used to discriminate the random clutter and locate the symmetry points of the symmetric targets.

Motivation

Most AP and AT mines are symmetrical that they have either cylindrical or box-like shapes [7, 10]. However, clutter have no definite shape as shown in Figure 5.6. GPR measurements also show a symmetric signature for symmetric buried objects and asymmetric for asymmetric objects as shown in Figures 5.7 and 5.8. The symmetry difference between the target reflections and variable clutter in B-scan is one of the

Figure 5.6. (a) Box like plastic landmine, (b) AP mine having a shape of cylinder and (c) Irregular rock clutter.

important signal features for target classification [55,56]. Symmetry filtering addresses the problems associated with distinguishing landmines from friendly objects.

Principle

When a radar set moves against a target bearing ground, a hyperbolic structure is created in the image. This is caused due to the relative positions of the antenna set and the point target [16]. The center or apex of the hyperbola appears when the antenna is just above the point-target. It is the shortest distance between the point-target and the antenna position or it is the position at which the shortest time delay is recorded as shown in Figure 5.7.

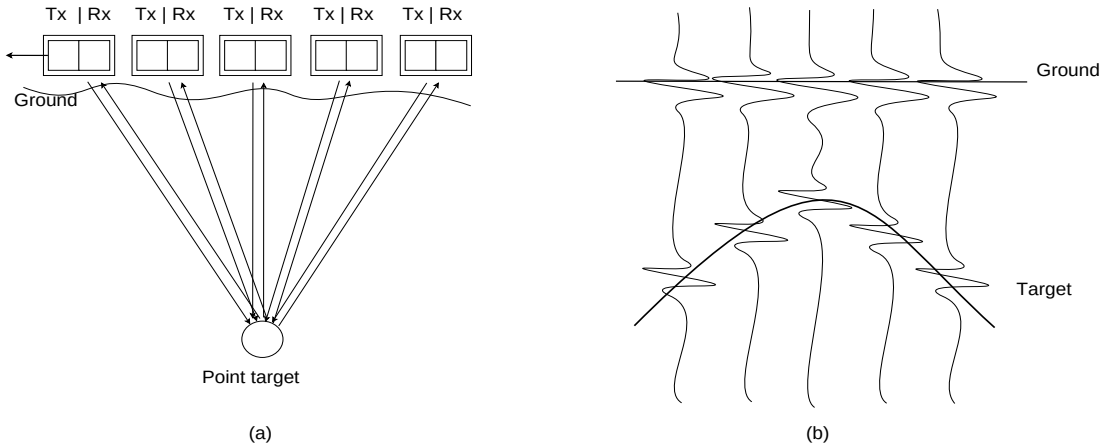

Figure 5.7. (a): Transmit-receive at different positions and (b): creation of hyperbola due to the relative positions.

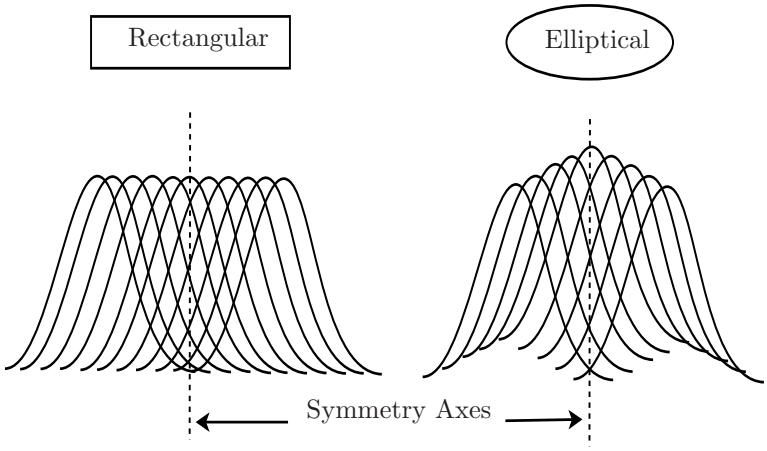

Figure 5.8. Hyperbolic structures for a rectangular and elliptical shaped objects.

Each point in the object creates a hyperbola and the summation of hyperbolas of a symmetrical object appears as a symmetrical hyperbola image centered at the middle of the object as shown in Figure 5.8. However, if the buried object is asymmetrical, the summation of hyperbolas appears to be an asymmetrical image.

The objective is to design a symmetry filter which suppresses signatures from asymmetrical clutter and enhances return signals from symmetric targets. The application of the symmetry filtering method for clutter reduction is explained in [55] for single target and in [56] for multiple-target scenarios. In both cases, techniques to reduce the stationary clutter components were not incorporated. Unless these components are reduced, a stationary clutter is considered as a symmetrical object and cause false alarms. Moreover, there was no explanation as to how the symmetry locations are determined in the presence of many or unknown number of targets. The presence of noise and DC-offset also affects the symmetry properties of the received signal and must be removed prior to symmetry filtering.

Signal Model

A signal model for symmetry filtering can be achieved by decomposing the background signal into constant and variable components. The constant components are due to the stationary background and the variable components are due to undulated ground bounce, soil roughness scattering and external anomaly reflections. That is, $\mathbf{s}_b(t,x) = \mathbf{s}_{bs}(t,x) + \mathbf{s}_{bv}(t,x)$, and the signal model given in Equation (5.1) can be rewritten as a summation of the stationary and variable components of the GPR return signal.

$$\mathbf{y}(t,x) = \underbrace{\mathbf{s}_c(t,x) + \mathbf{s}_n(t,x) + \mathbf{s}_{bs}(t,x)}_{\mathbf{y}_{st}(t,x)} + \underbrace{\mathbf{s}_t(t,x) + \mathbf{s}_{bv}(t,x)}_{\mathbf{y}_{vr}(t,x)} \tag{5.25}$$

where $\mathbf{s}_{bs}(t,x)$ and $\mathbf{s}_{bv}(t,x)$ are the constant and variable components of the background signal, respectively.

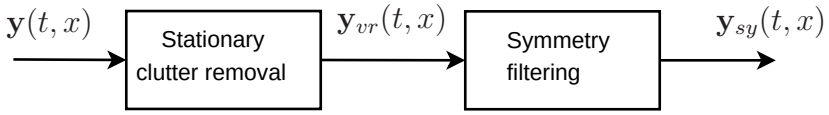

Figure 5.9. Symmetry filtering procedure.

where $\mathbf{y}_{sy}(t,x)$ is the symmetric part of the measurement signal.

The objective is to test the symmetry difference between the target and the clutter. Under the null hypothesis, H_0, the symmetry difference is negligible, whereas under the alternative, H_1, there is a considerable symmetry difference. H_0 indicates that there is no symmetric object, whereas, H_1 indicates the presence of a symmetric object. The target detection procedure tests the significance of the symmetry difference using the amplitude of the residue. The suggested statistics are given as follows:

$$T_{s1}(x) = \max_t |\mathbf{y}_{sy}(t,x)\}| \tag{5.26}$$

$$T_{s2}(x) = \frac{1}{N}\sum_{t=1}^{N} |\mathbf{y}_{sy}(t,x)|^2 \tag{5.27}$$

The null hypothesis is rejected if the test statistic is greater than a threshold, $T_{s\alpha}$, otherwise the null hypothesis is accepted.

$$T_s(x) \underset{H_0}{\overset{H_1}{\gtrless}} T_{s\alpha} \tag{5.28}$$

where the threshold $T_{s\alpha}$ is determined empirically.

Symmetry Filtering Algorithm

The procedure for the symmetry filtering method has two parts as depicted in Figure 5.9. The first is the preprocessing part that includes techniques of signal conditioning and data correction. The second part includes techniques of symmetry filtering and symmetry point location.

A. Preprocessing and Stationary Clutter Removal

In this step the preprocessing techniques and clutter reduction techniques discussed at the beginning of this chapter are applied here to remove the DC-offset, noise and the stationary clutter components.

Step 1. DC-offset removal

DC-offset removal has been explained briefly in Section 4.3 and can be performed according to Equation (4.2). The discrete form of Equation (4.2) is given by:

$$\mathbf{y}_1[i,j] = \mathbf{y}[i,j] - \frac{1}{M}\sum_{i=1}^{M}\mathbf{y}[i,j],\ \ i,j \in \mathbb{Z} \tag{5.29}$$

where M is the total number of pixels along the A-scan which is equivalent to the number of samples per scan. The time index is transformed to pixels as:

$$i = t \times \frac{\text{samples-per-scan}}{\text{range}} \tag{5.30}$$

where 'samples-per-scan' and 'range' belong to the measurement setup of the antenna-controller set. For a 1.5 GHz GPR antenna, GSSI [61] recommends samples-per-scan of 512 and range of 12 ns as given in Section 2.5.1.

Step 2. Antenna crosstalk removal

The quasi-stationary signal component can be reduced using time window gating, as explained in Section 5.3.3. Time window gating can be formulated as:

$$\mathbf{y}_2[t,x] = \begin{cases} \mathbf{y}_1[t,x], & \text{if } t \geq t^* - \tau \\ 0\ , & \text{if } t < t^* - \tau \end{cases} \tag{5.31}$$

where t^* is the arrival time of the first reflection from the ground surface, which is estimated from the general antenna height information and τ is the pulse width. Modern GPR antennas are shielded in that the effect of cross-coupling and interference from other objects is negligible. For a shielded antenna, the cross coupling and stationary ground components are reduced using simple background subtraction techniques [17, 32].

Step 3. Noise removal

The additive noise can be removed using moving average smoothing techniques. The exponential moving average (EMA) is one of the techniques which can effectively remove the additive noise and is given as in Equation (5.3).

$$\mathbf{y}_3[i,j] = k_\alpha \mathbf{y}_2[i,j] + (1-k_\alpha)\mathbf{y}_3[i,j] \tag{5.32}$$

Step 4. Stationary clutter removal

Stationary clutter corresponds to the signal bounced from a uniform air-ground interface. This component can be removed using the techniques explained in Section 5.5.1. The signal bounced from nonuniform ground is considered as a nonsymmetric clutter and will be removed using symmetry filtering. The discrete form of stationary clutter removal algorithm is given by:

$$\mathbf{y}_4[i,j] = \mathbf{y}_3[i,j] - \frac{1}{K}\sum_{j=1}^{K}\mathbf{y}_3[i,j] \tag{5.33}$$

where K indicates the number of A-scans whose average is used to estimate the stationary ground and $\mathbf{y}_4(i,j)$ is the variable component of the GPR return signal to be processed using the symmetry filter.

B. Symmetry Filtering

Step 5. Locating symmetry position

The symmetry filtering algorithm is applied on the preprocessed return signal, $\mathbf{y}_4[i,j]$. The variable component of the GPR return signal is equal to the preprocessed signal, i.e., $\mathbf{y}_{vr}[i,j] = \mathbf{y}_4[i,j]$. To locate the symmetry points, we implement staking of the preprocessed return signals, formulated as:

$$\mathbf{z}[i,j] = \sum_{m=-M}^{M}\sum_{n=1}^{N}\mathbf{y}_{vr}[i-m,j-n]\mathbf{y}_{vr}[i-m,j+n] \tag{5.34}$$

where N is related to the valid aperture radar and M is related to the radar pulse width. The symmetry position for a single target assumption as explained in [55] is:

$$J_0 = \arg\max_j(\mathbf{z}[i,j]) \tag{5.35}$$

where J_0 is the symmetry position of the target reflection signal. When there are many targets or the number of targets are unknown, we use a search algorithm to locate the points of symmetry.

a. Calculate the peak values of the traces

$$r[j] = \max_i(\mathbf{z}[i,j]) \tag{5.36}$$

b. Search for j such that $r[j]$ is greater than γ times the average of $r[j]$

$$J = j : r[j] > \gamma \frac{1}{N} \sum_{j=1}^{N} r[j] \tag{5.37}$$

where γ is multiplied with the mean to set the threshold.

c. Declare J as a point of symmetry if $r[J]$ satisfies the condition in (b) and $r[J]$ is greater than all values of $r[J \pm k]$.

$$J_0 = J : r[J] \geq \frac{1}{2}(r[J-k] + r[J+k]) + \frac{1}{2}|r[J-k] - r[J+k]|, \forall k \in 1, 2, \ldots, R \tag{5.38}$$

where R is the number of pixels that fall in the radius of the smallest landmine, which is equal to the product of the radius of the smallest landmine and number of scans-per-unit length of the antenna setup.

Step 6. Compute the range direction symmetry weighting matrix for all possible values of J_0

$$\rho[i] = \frac{\sum_{m=-M}^{M} \sum_{n=1}^{N} \mathbf{z}[i-m, J_0-n]\mathbf{z}[i-m, J_0+n]}{\sqrt{\sum_{m=-M}^{M} \sum_{n=1}^{N} \mathbf{z}[i-m, J_0-n]^2 \sum_{m=-M}^{M} \sum_{n=1}^{N} \mathbf{z}[i-m, J_0+n]^2}} \tag{5.39}$$

Step 7. Calculate the lateral direction symmetry weighting matrix

$$\mathbf{a}[i, J_0+j] = \mathbf{a}[i, J_0-j] = \frac{\mathbf{z}_{12}[i,j]}{\sqrt{\mathbf{z}_{11}[i,j] \times \mathbf{z}_{22}[i,j]}} \tag{5.40}$$

where

$$\begin{aligned}
\mathbf{z}_{12}[i,j] &= \sum_{m=-M}^{M}\sum_{n=-N}^{N}\mathbf{z}[i-m, J_0-j-n]\mathbf{z}[i-m, J_0+j+n] \\
\mathbf{z}_{11}[i,j] &= \sum_{m=-M}^{M}\sum_{n=-N}^{N}\mathbf{z}[i-m, J_0-j-n]^2 \\
\mathbf{z}_{22}[i,j] &= \sum_{m=-M}^{M}\sum_{n=-N}^{N}\mathbf{z}[i-m, J_0+j+n]^2
\end{aligned} \tag{5.41}$$

where M and N are related to the radar pulse width.

Step 8. Determine the synthetic symmetry filtering weighting matrix as:

$$\mathbf{w}[i,j] = e^{\rho_n[i]}e^{\mathbf{a}_n[i,j]} \tag{5.42}$$

where $\rho_n[i]$ and $a_n[i,j]$ are the normalization of $\rho[i]$ and $a[i,j]$, respectively.

Step 9. Perform symmetry filtering

The overall filtering is considered for each symmetry position J_0 and is given by:

$$\mathbf{y}_{sy}[i,j] = \mathbf{y}_{vr}[i,j]w[i,j] \tag{5.43}$$

5.6 Comparison and Conclusion

Our comparison of the signal processing techniques described in the previous sections will be based on detection rates, false alarm rates and computational complexity. To do this, we use receiver operating characteristic (ROC) curves [9].

5.6.1 ROC Evaluation

Due to the large number of parameters in the detection algorithms, comparison of the various detection techniques is a difficult task. A commonly used method to compare detector performance is through ROC curves [9]. The rates of false alarm and correct

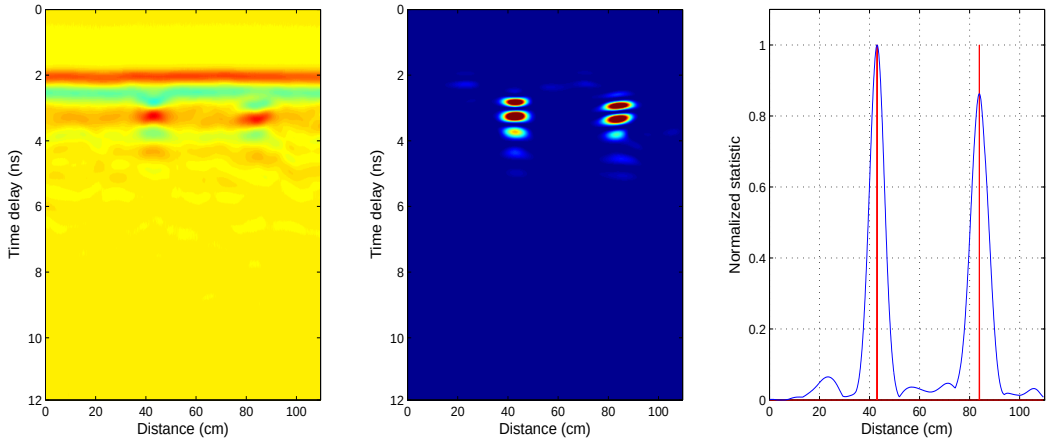

Figure 5.10. Left: Radargram in the presence of PMN1 and PMN2 in wet sand soil. Middle: Radargram after symmetry filtering. Right: test statistic and symmetry points.

detection are determined for varying nominal levels of significance. ROCs are considered to be a good way to compare detectors as they incorporate both these performance indicators.

While using the available data sets, the unknown ground truth and spatial variation of the background create difficulties. It is not possible to simply run the detectors over target free or target-present data and estimate the probabilities of false alarm and correct detection as the average number of detections. There is a correlation between the detection decisions, unless the effect of the background is completely removed. Several techniques can be used for background estimation, as discussed in Section 5.5.1. Here, a running spatial filter of background traces is used for background signal estimation.

A test area is manually identified from the target-present recordings to find the detection rate. The same area of ground is then tested in the target-free recordings to find the false alarm rate. The testing procedure is described in Table 5.2. The threshold setting area in Step 1 of Table 5.2 was chosen to start at 150 traces before the start of the test area and to finish 50 traces before the start of the test area for the results to be shown here.

5.6.2 Conclusion

In this chapter different signal processing techniques have been presented to reduce clutter in GPR data. The techniques are compared based on their detection perfor-

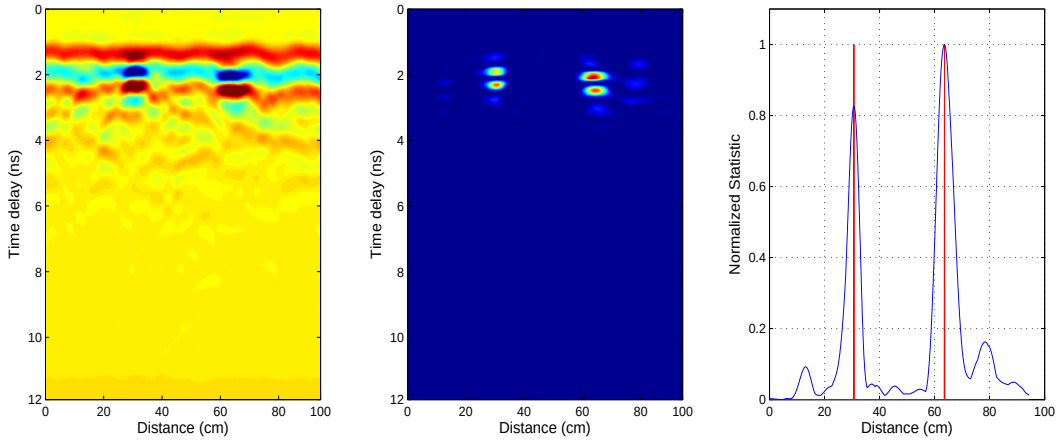

Figure 5.11. Left: Radargram in the presence of PMN1 and PMN2 in wet rough clay soil. Middle: Radargram after symmetry filtering. Right: test statistic and symmetry points.

Step 1.	Find a test statistic using a moving window background estimate for a target free area close to the test area. The moving window background estimator is given in Table 5.3.
Step 2.	Set the threshold at an appropriate percentile of the test statistics calculated above to achieve a desired false alarm probability.
Step 3.	Find the test statistics of the trace in the test area using moving window ground estimator. The background estimate is updated depending on whether a target is declared to be present or not.
Step 4.	Calculate the ratio of the number of traces where a target is declared to be present to the ratio of the total number of traces tested in Step 3. Depending on whether the test area contains a target or not, the ratio will represent the probability of detection, P_d or false alarm, p_f

Table 5.2. ROC evaluation procedure.

Step 1. Initialize list of background traces immediately before the area under consideration.

Step 2. For each trace, i, in the area under consideration, find a test statistic $T_s(i)$ for the current trace using the current list of background traces.

Step 3. Compare the test statistic against a threshold

- If $T_s(i)$ is less than the threshold, declare the trace to be target free and update the list of background traces by adding the current trace and removing the oldest trace.
- Otherwise declare a target present and retain the current list of background traces.

Table 5.3. Moving window background estimator.

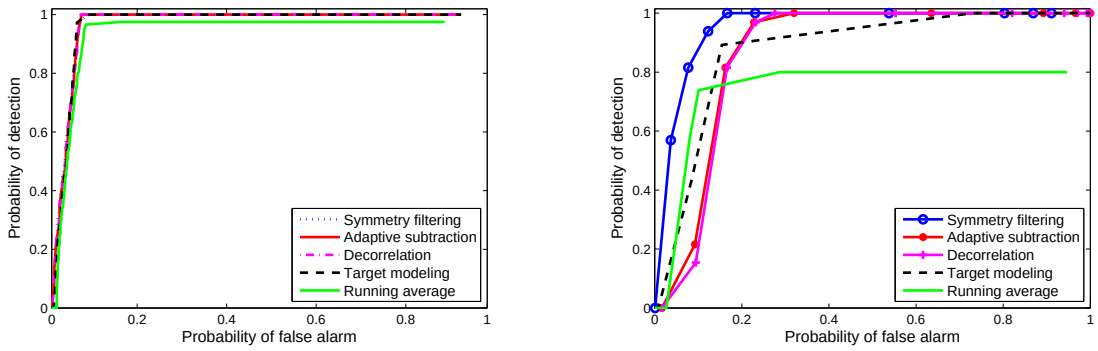

Figure 5.12. ROC curves for PMN1 in sand soil (left) and in clay soil (right).

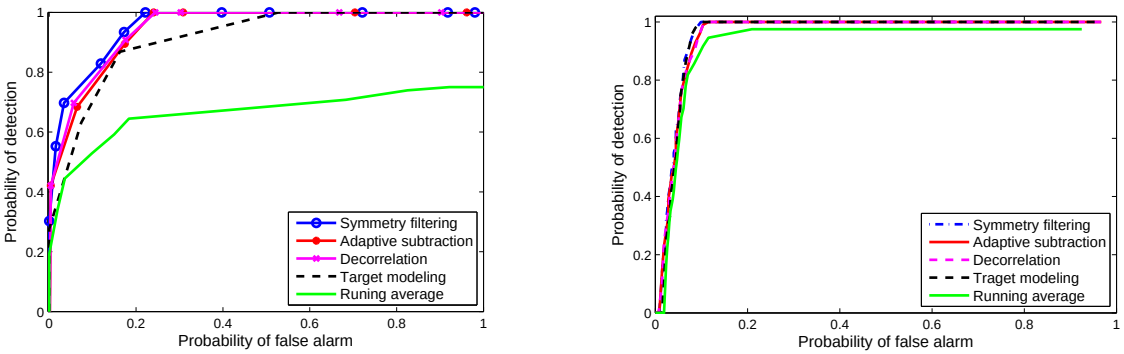

Figure 5.13. ROC curves for PMN2 in sand soil (left) and in clay soil (right).

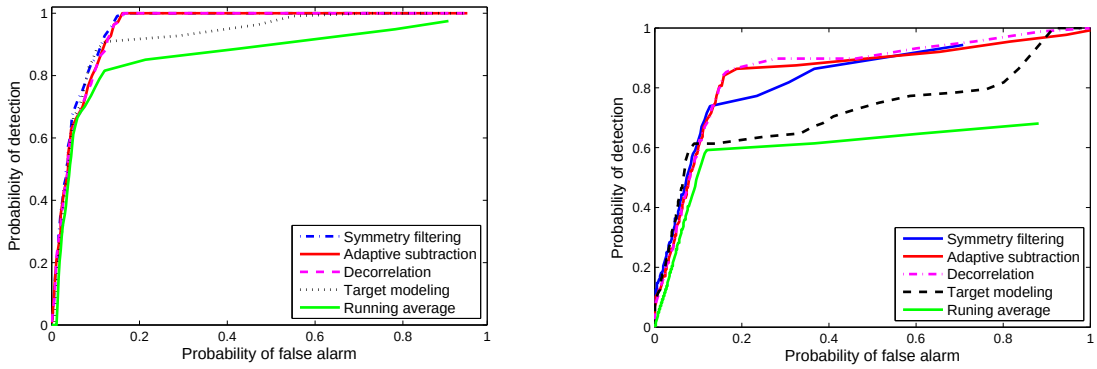

Figure 5.14. ROC curves for M14 in sand soil (left) and in clay soil (right).

mance using ROC curves. It has been shown that the way the background is estimated and the number of traces considered in the estimation have an impact on the analysis results.

A simple mean subtraction technique is not sufficient to reduce the clutter. The background estimator in both moving average and median filters is not accurate enough, and both methods give poor results. Symmetry filtering has shown excellent performance for all scenarios except for M14 in clay soil. It has also been found that PMN2 is more detectable in clay than in sand soil.

Adaptive background estimator yields the best results in reducing the probability of false alarm. The symmetry filtering algorithm, which detects a target based on its geometry, yields the best results in discriminating landmines from natural clutter. The decorrelation technique also shows very good performance in rough and wet surfaces.

Chapter 6
Decision Fusion

In this chapter, the fusion of correlated decisions is investigated. We hereby consider a single sensor, GPR, and many signal processing experts (algorithms) to process the observations. The experts are designed to reduce the clutter components and to make a decision regarding the presence or absence of a target. The decisions made by the experts are sent to the fusion center (FC) so that. The FC could ultimately make a global decision depending on the received decisions and some decision fusion rules.

We considered here three decision fusion techniques. Two of the techniques are adapted optimal fusion techniques based on Bahadur-Lazarsfeld and Chow expansions. The third technique is based on fuzzy set operations. The performance of these techniques is compared with the classical decision fusion techniques.

6.1 Motivation

An animal recognizes its environment by the evaluation of signals from multiple and multifaceted sensors. Nature has found a way to integrate information from multiple sources to a reliable and feature-rich recognition. Even in the case of sensor deprivation, systems are able to compensate for lacking information by reusing data obtained from sources with an overlapping scope. Humans for example combine signals from the five body senses (sight, sound, smell, taste, and touch) with knowledge of the environment to create and update a dynamic model of the world. Based on this information, the individual interacts with the environment and makes decisions about present and future actions.

In GPR based landmine detection, many signal processing experts are employed as clutter reduction techniques and as detectors. Performance of signal processing detectors depends on the type of buried object; soil type, roughness and homogeneity; amount of clutter and added moisture [9, 15]. The decisions made by these experts may be conflicting, vague or incomplete. Moreover, there is no single expert, which is the most favorable for all scenarios [9]. Cooperation among the experts could improve the detection capacity of the sensor by increasing the power of detection and reducing the false alarm rate. The ultimate objective of data fusion is, therefore, to provide an accurate assessment of the situation so that an appropriate action can be taken.

6.2 Background

Data fusion is a process of combining information from different sources aiming to improve the performance of a system. The most known example of fusion is the use of different sensors for detecting a target. Even if the information comes from a single sensor, experts may interpret it differently and reach different conclusions. In this case, decisions from many experts may be fused to come up with a single decision with the highest confidence. The main objective of employing fusion is to produce a fused result that provides the most detailed and reliable information possible.

6.2.1 Advantages of Fusion

The advantages of a multi-expert system over a single expert system can be quantified in terms of improvement in the ability of situation assessment. There are many factors that multi-expert fusion system contributes to the enhancement of quantifiable system performance [87–89]. Some of them are:

- Higher signal-to-noise ratio
- Increased robustness and reliability in the event of failure
- Reduced uncertainty
- Increased hypothesis discrimination
- Increased confidence, since detectors can confirm each other's inference
- Shorter response time

Data fusion can be used for many purposes like detection, recognition, identification, tracking and decision making. Information and decision fusion find applications in a wide range of areas, such as defense, robotics, medicine, space, pattern recognition, radar tracking, finance, meteorology and traffic control.

6.2.2 Fusion Strategies

Data can be combined either as it arrives at the system or at a defined level within the fusion process [15, 87, 90]. The fusion levels are classified according to the processing stage or the abstraction level where the fusion takes place [91]. There are mainly three types of fusion strategies, namely, data (low-level) fusion, feature (intermediate-level) fusion, and decision (high-level) fusion.

Data fusion combines raw data from several sources and produces new raw data which is expected to be more expressive than the inputs. Landmine detection systems that apply data fusion usually have multiple sensors of the same kind that differ in wavelength, range or polarization. The fusion methods are based on a physical model of the sensor and combine different sensor data into one image for visual display or further analysis [15].

Data fusion usually takes place at the front end of the processing stream and is generally based on signal and image processing techniques. Examples of this strategy are fusion of multi-spectral data and images from different sensors. It is also possible to fuse data from a single sensor after it has been processed using many experts.

Feature fusion merges several features like edges, corners, lines, texture parameters, etc. into a feature set. The features may come from several raw data sources like several sensors or extracted from the same raw data. The features may be obtained from several feature extraction methods. For landmine detection applications, features may be extracted from many sensors of the same kind or from the a single sensor [91].

Decision fusion combines decisions or probabilities of detections obtained from several sensors or from the same sensor using several experts. If the experts return a confidence or score instead of a decision, it is also a decision fusion problem. These decisions may be made based on raw data, features extracted or output of signal processing experts [87, 92]. Popular fusion methods include Bayesian approaches, applications of Dempster-Shafer theory, fuzzy logic rules and voting techniques [15].

In general, the choice of a suitable fusion level depends on the available sensor types. When the sensors are alike, one can opt for fusion at data level. Feature level fusion is the proper level when features obtained from different sensors can be combined so that the combination provides sufficient information for landmine detection. When the sensors are very different or we have only single sensor and many experts, decision level fusion is more suitable and computationally efficient.

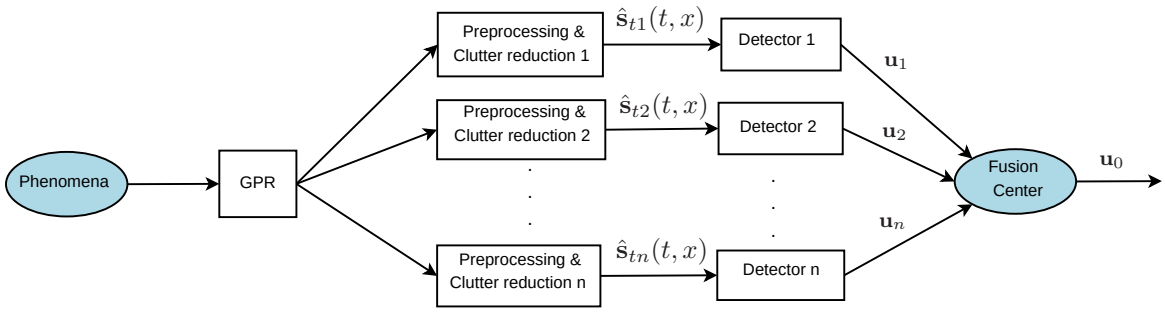

Figure 6.1. Decision fusion architecture for single sensor, GPR, and many detectors.

6.2.3 Decision Fusion Problem

The design of local decision rules and the optimal decision fusion rule for binary local decisions has been investigated in great detail in [87, 93]. When the decisions are assumed to be conditionally independent, it has been shown under the Bayesian and NP formulations, that the optimal decision rule is nothing but the likelihood ratio (LR) based on binary quantizer. The optimal decision fusion rule statistic is a weighted sum of the decisions [87]. However, when the local decisions are dependent, the likelihood ratio based binary quantization at the local detectors may not be optimal. In [94], the authors presented examples of performance loss due to correlation when local decisions are based on LR tests. In the case of dependent observations, the computational complexity of the distributed detection problem increases considerably [92].

In our system, the GPR antenna set scans over a target bearing ground and the experts are arranged in parallel to work as clutter reduction techniques and decision makers. The detectors receive common data and reach a local inference regarding the presence of a target based on the received data and some algorithms.

Here, we focus only on the design of fusion rules at the fusion center. Each detector receives the observation data $y_i \in \mathbb{R}^n$ and transforms it using local mapping to a local decision $u_i = g_i(y_i)$, $u_i \in \{0, 1\}$, $i = 1, 2, \ldots, n$. The decisions, $(u_1, u_2, \ldots, u_n)$, are transmitted and combined in the FC to yield a global decision u_0. The decision fusion architecture for this model is depicted in Figure 6.1.

If the entire detection system is considered, it is a data in, decision out system whereas the fusion center is a decision in, decision out system.

6.3 Optimal Decision Fusion Techniques

In this section, a quick review of the optimal binary decision fusion according to the NP criterion will be presented. We consider a binary hypothesis testing problem with two hypotheses H_0 and H_1. The probability distribution of the received signals of the n detectors are assumed to be known under both hypothesis, i.e $p(y_i|H_0)$ and $p(y_i|H_1)$ for $i = 1, 2, \ldots, n$.

Each detector processes its observation y_i and makes a decision u_i, which may take the value 0 or 1 depending on the hypothesis. Optimality criteria for distributed detection systems in the case of binary decisions are known from previous studies [89, 93, 95]. According to the NP criterion, it is required to maximize the global detection probability while keeping the global false alarm probability below a given value [96]. The binary decision at each detector can be described as:

$$u_i = \begin{cases} 0, & \text{if } L(y_i) = \frac{p(y_i|H_1)}{p(y_i|H_0)} \geq \underline{\lambda}_i \\ 1, & \text{otherwise} \end{cases} \tag{6.1}$$

where $\underline{\lambda}_i$ is the detector's threshold. For most types of observations, like Gaussian, exponential and Rayleigh distributions, the comparisons given in Equation (6.1) are equivalent to the comparison of the statistic to another threshold t_i. The decision rule in Equation (6.1) becomes:

$$u_i = \begin{cases} 0, & \text{if } y_i \geq t_i \\ 1, & \text{otherwise} \end{cases} \tag{6.2}$$

where the threshold t_i is determined by the probability of false alarm of the i^{th} detector.

In distributed detection systems, sensor noise is usually assumed to be uncorrelated and decisions are independent. However, cases may arise where the noise is correlated and the assumption of statistical independence of the local decisions is no longer valid [94, 97]. The FC makes a global decision u_0, $u_0 = 0$ for accepting H_0 and $u_0 = 1$ for accepting H_1. The problem is to design a decision fusion rule $u_0 = f(u_1, u_2, \ldots, u_n)$, $f : \{0, 1\}^n \longrightarrow \{0, 1\}$, which minimizes the average Bayesian cost function formulated in Equation (6.4).

$$u_0 = \begin{cases} 0, & \text{when no target is detected} \\ 1, & \text{when a target is detected} \end{cases} \tag{6.3}$$

The average Bayesian cost can be represented as:

$$\underline{C} = \sum_{j=0}^{1} \sum_{k=0}^{1} C_{jk} P(u_0 = j, H_k) \tag{6.4}$$

where C_{jk} is the cost of choosing decision j while the true decision is k.

Design of the fusion system involves the derivation of the decision-combining rule based on some optimization criteria [88]. When the decisions are statistically independent, the problem is greatly simplified and can be solved using the Chair and Varshney rule [93]. The problem with correlated local decisions was studied in different forms by Ashock *et al.* in [92] who considered copula based correlated decision fusion, Aalo and Viswanathan in [94], Kam *et al.* in [97], Darkopoulos and Lee in [98], and Jian and Ansari in [95] who considered adaptive fusion of correlated decisions.

By finding an expansion for the probability density function of U, $P(U)$, it is possible to approximate $P(U)$ by a partial sum. The Bahadur-Lazerfeld and Chow expansions are interesting classes that can be used to estimate $P(U)$ in a suitable form. However, the two methods use different approaches to compute the distribution.

6.3.1 Bahadur-Lazerfeld Expansion

In the case of correlated decision fusion, the degree of dependence has to be determined first so that an appropriate fusion rule is derived. The Bahadur-Lazerfeld expansion (BLE) provides a way to expand the joint pdf, $P(U)$, by a set of polynomials where the coefficients of the polynomials are correlation coefficients [97, 99]. Application of BLE allows computation of all joint probabilities by estimating only n multivariate integrals, where n is the number of detectors.

Since the signal processing experts receive the observation data from the same sensor, the detectors are statistically identical and the correlation coefficients are index independent. We consider the local detectors receive equi-correlated zero mean Gaussian noise with unit variance. After computing the required threshold at the local detectors, the probability of detection at the fusion center is obtained as a function of the correlation coefficient. The correlation coefficient can take a value between -1 and 1.

For the correlated local decision vector, $U = [u_1, u_2, \ldots, u_n]$, and the cumulative probability density function of $P(U)$, the optimal fusion rule of the FC is given by

$$\lambda(U) = \frac{P(U|H_1)}{P(U|H_0)} \underset{H_0}{\overset{H_1}{\gtrless}} \frac{P_0(C_{10} - C_{00})}{P_1(C_{01} - C_{11})} = \lambda_0 \tag{6.5}$$

where P_0 and P_1 are the prior probabilities of the hypothesis H_0 and H_1, respectively.

Using the BLE based probability density function (pdf), it is possible to develop optimal data fusion rules for correlated binary local decisions. Specifically, the pdf of the local binary decisions can be represented by the pdf of independent random variables multiplied by correlation factor [97, 100, 101].

$$P(U) = P_1(U)F(U) \tag{6.6}$$

where $P_1(U)$ is the conditional probability distribution for the independent case and $F(U)$ is a correction factor. The correction factor, which is a function of the correlation coefficients and normalized random variables, represents the correlation between the local decisions. The normalized random variables are derived from the local decisions and result in a distribution having zero mean and unit variance. The derivation assumes that p_i is neither 0 nor 1, and the normalized variables z_i are defined as:

$$z_i = \frac{u_i - p_i}{\sqrt{p_i(1 - p_i)}} \tag{6.7}$$

where $p_i = p(u_i = 1)$ whereas $1 - p_i = P(u_i = 0)$. The Bahadur-Lazarsfeld's polynomials can be obtained by systematically forming distinct products of z_is taken none at a time, one at a time, two at a time, and, all at a time.

$$\varphi_i(U) = \begin{cases} 1 & i = 0 \\ z_1 & i = 1 \\ z_2 & i = 2 \\ \vdots & \\ z_n & i = n \\ z_1 z_2 & i = n + 1 \\ z_1 z_3 & i = n + 2 \\ \vdots & \\ z_1 z_2 z_3 & i = n + 1 + \frac{n(n-1)}{2} \\ \vdots & \\ z_1 z_3 \ldots z_n & i = 2^n - 1 \end{cases} \tag{6.8}$$

These polynomials are not orthogonal by themselves, but they are orthogonal with respect to the weighting function $P_1(U)$,

$$P_1(U) = \prod_{i=1}^{n} p_i^{u_i}(1-p_i)^{1-u_i} \tag{6.9}$$

that is,

$$\sum_{U} \varphi_i(U)\varphi_j(U)P_1(U) = \delta_{ij} \tag{6.10}$$

where δ_{ij} is the Kronecker delta function.

$$\delta_{ij} = \begin{cases} 1, & \text{if } i = j \\ 0, & \text{if } i \neq j \end{cases} \tag{6.11}$$

In particular, the function $P(U)/P_1(U)$ has the following expansion

$$\frac{P(U)}{P_1(U)} = \sum_{i=1}^{2^n-1} b_i\varphi_i(U) \tag{6.12}$$

where b_i is a correlation coefficient and is given by:

$$b_i = \sum_{U} \varphi(U)P(U) = E[\varphi(U)] \tag{6.13}$$

Recalling that $\varphi(U)$ is the product of normalized variables, z_i, we can clearly see that the b_is are the correlation coefficients and $b_0 = 1$, and $b_1 = b_2 = \cdots b_n = 0$. Depending on the order of $\varphi(U)$, the correlation coefficients can be defined as a function of $\{z_i\}_{i=1}^{n}$ by order as follows:

$$\begin{aligned} \gamma_{ij} &= \sum_{U} z_i z_j P(U) = E\left[z_i z_j\right] && 2^{nd} \text{ order} \\ \gamma_{ijk} &= \sum_{U} z_i z_j z_k P(U) = E\left[z_i z_j z_k\right] && 3^{rd} \text{ order} \\ &\vdots \\ \gamma_{ij\ldots n} &= \sum_{U} z_i z_j \ldots z_n P(U) = E\left[z_i z_j z_k \cdots z_n\right] && n^{th} \text{ order} \end{aligned} \tag{6.14}$$

The complete expansion of $P(U)$ in Equation (6.12) becomes:

$$P(U) = P_1(U)\left[1 + \sum_{i<j}\gamma_{ij}z_i z_j + \sum_{i<j<k}\gamma_{ijk}z_i z_j z_k + \cdots \gamma_{12\ldots n}z_1 z_2 \cdots z_n\right] \tag{6.15}$$

The conditional normalized variables, z_i^h, where $h = 0, 1$ indicates the hypothesis H_h, are formulated as:

$$z_i^h = \frac{u_i - P(u_i = 1|H_h)}{\sqrt{P(u_i = 1|H_h)[1 - P(u_i = 1|H_h)]}} \tag{6.16}$$

Let the probability of false alarm and the probability of missed detection of the i^{th} local detector be $P_{Fi} = P(u_i = 1|H_0)$ and $P_{Mi} = P(u_i = 0|H1)$, respectively. Then, the conditional normalized variables can be expressed as:

$$z_i^0 = \frac{u_i - P_{Fi}}{\sqrt{P_{Fi}(1 - P_{Fi})}}\ ,\ z_i^1 = \frac{u_i - P_{Di}}{\sqrt{P_{Di}(1 - P_{Di})}} \tag{6.17}$$

The variable z_i^0 is the way u_i is transformed assuming that detector i decides for H_0, while z_i^1 corresponds to normalized u_i when the detector i decides for H_1.

In a similar way, the conditional correlation coefficients are given by:

$$\begin{aligned}
\gamma_{ij}^h &= \sum_U z_i^h z_j^h P(U) = E\left[z_i^h z_j^h\right] && 2^{nd} \text{ order} \\
\gamma_{ijk}^h &= \sum_U z_i^h z_j^h z_k^h P(U) = E\left[z_i^h z_j^h z_k^h\right] && 3^{rd} \text{ order} \\
&\vdots \\
\gamma_{ij\ldots n}^h &= \sum_U z_i^h z_j^h \ldots z_n^h P(U) = E\left[z_i^h z_j^h z_k^h \cdots z_n^h\right] && n^{th} \text{ order}
\end{aligned} \tag{6.18}$$

The likelihood ratio test in Equation (6.5) can be written as:

$$\lambda(U) = \frac{P_1(U|H_1)}{P_1(U|H_0)} \cdot \frac{\left[1 + \sum_{i<j}\gamma_{ij}^1 z_i^1 z_j^1 + \sum_{i<j<k}\gamma_{ijk}^1 z_i^1 z_j^1 z_k^1 + \cdots + \gamma_{12\cdots n}^1 z_i^1 z_j^1 \cdots z_n^1\right]}{\left[1 + \sum_{i<j}\gamma_{ij}^0 z_i^0 z_j^0 + \sum_{i<j<k}\gamma_{ijk}^0 z_i^0 z_j^0 z_k^0 + \cdots + \gamma_{12\cdots n}^0 z_i^0 z_j^0 \cdots z_n^0\right]} \tag{6.19}$$

Using the definition of the probability of false alarm and missed detection of the i^{th} detector and Equation (6.9) we have:

$$\frac{P_1(U|H_1)}{P_1(U|H_0)} = \frac{\prod_{i=1}^{n}(1-p_{Mi})^{u_i}(p_{Mi})^{1-u_i}}{\prod_{i=1}^{n}(1-p_{Fi})^{1-u_i}(p_{Fi})^{u_i}} = \prod_{i=1}^{n}\left(\frac{1-p_{Mi}}{p_{Fi}}\right)^{u_i}\left(\frac{p_{Mi}}{1-p_{Fi}}\right)^{1-u_i} \tag{6.20}$$

From Equation (6.19) and (6.20), the log-likelihood ratio test is given as:

$$\begin{aligned}\log\lambda(U) &= \sum_{i=1}^{n} u_i\left[\log\frac{(1-p_{Mi})(1-p_{Fi})}{p_{Mi}p_{Fi}}\right] + \sum_{i=1}^{n}\log\frac{p_{Mi}}{1-p_{Fi}} \\ &+ \log\frac{1+\sum_{i<j}\gamma^1_{ij}z^1_i z^1_j + \sum_{i<j<k}\gamma^1_{ijk}z^1_i z^1_j z^1_k + \cdots + \gamma^1_{12\cdots n}z^1_i z^1_j\cdots z^1_n}{1+\sum_{i<j}\gamma^0_{ij}z^0_i z^0_j + \sum_{i<j<k}\gamma^0_{ijk}z^0_i z^0_j z^0_k + \cdots + \gamma^0_{12\cdots n}z^0_i z^0_j\cdots z^0_n}\end{aligned} \tag{6.21}$$

Equation (6.21) is the fusion rule for a system of correlated local decisions. It is known that the number of computations are so high. For n detectors, the BLE expansion of $P(U)$ contains 2^n-1 coefficients, the n first-order probabilities p_i, the $\binom{n}{2}$ second-order correlation coefficients γ_{ij}, the $\binom{n}{3}$ third-order correlation coefficients γ_{ijk}, and so on. In many practical applications, the correlation coefficient after a certain order can be neglected. Thus, the computational burden can be reduced [97, 99–101].

On the other hand, tentative approximations of the Bahadur-Lazarsfeld model by truncation were found to be less robust than the original model. Truncation could result in improper probabilities that can be negative or greater than one. Moor in [99] suggested a replacement for the negative probabilities by a small number like 10^{-5}.

If the decisions are statistically independent, the joint probability simplifies to:

$$P(U) = P_1(U) = \prod_{i=1}^{n} P(u_i) = \prod_{i=1}^{n} p_i^{u_i}(1-p_i)^{1-u_i} \tag{6.22}$$

In this case, the estimation of $P(U)$ reduces to the estimation of n probabilities p_i. Moreover, if all the correlation coefficients are zero under both hypotheses, then the optimal fusion rule simplifies to a linear form [97, 100, 101].

$$\log\lambda(U) = k_0 + \sum_{i=1}^{n} k_i u_i \tag{6.23}$$

where

$$\begin{aligned} k_0 = & \sum_{i=1}^{n} \log \frac{P_{Mi}}{1-P_{Fi}} \\ k_i = & \log \frac{(1-P_{Mi})(1-P_{Fi})}{P_{Mi}P_{Fi}} \end{aligned} \tag{6.24}$$

The fusion rule applied here is the same as the optimal fusion rule that Chair and Varshney developed in [93] for fixed local detectors with independent local decisions.

Here, we will consider a system of three detectors with decision variables u_1, u_2, u_3 and the global decision u_0. The FC minimizes the cost function while the i^{th} detector makes decision about the the observation in normal additive noise. This is achieved by minimizing the local Bayesian cost.

Corresponding to the definition of the threshold, λ_0 in Equation (6.4) and (6.5), we can define the threshold for the i^{th} detector as:

$$\lambda_0^{(i)} = \frac{P_0(C_{10}^{(i)} - C_{00}^{(i)})}{P_1(C_{01}^{(i)} - C_{11}^{(i)})}, \ i = 1, 2, 3 \tag{6.25}$$

We can rewrite the observations under the two hypotheses in the following form:

$$\begin{aligned} H_0 : & \ y_i = n_i^0 \\ H_1 : & \ y_i = m + n_i^1 \end{aligned} \tag{6.26}$$

where m is a positive constant. The noise variables n_1^0, n_2^0, n_3^0 and n_1^1, n_2^1, n_3^1 are jointly normal with zero mean and the covariance matrices are:

$$\sum\nolimits_0 = \sum\nolimits_{n_1^0, n_2^0, n_3^0} = \begin{bmatrix} 1 & 0 & 0 \\ 0 & 1 & 0 \\ 0 & 0 & 1 \end{bmatrix} \text{ and } \sum\nolimits_1 = \sum\nolimits_{n_1^1, n_2^1, n_3^1} = \begin{bmatrix} 1 & \rho_{ij} & \rho_{ij} \\ \rho_{ij} & 1 & \rho_{ij} \\ \rho_{ij} & \rho_{ij} & 1 \end{bmatrix} \tag{6.27}$$

where $0 \leq \rho_{ij} < 1$. From the statistically identical property of detectors, we have $\rho_{12} = \rho_{23} = \rho_{13}$. The i^{th} detector employs a log-likelihood ratio test locally to minimize the cost, $\underline{C}_i$

$$y_i \underset{H_0}{\overset{H_1}{\gtrless}} \tau_i = \frac{1}{m} \log \lambda_0^{(i)} + \frac{m}{2}, \ i = 1, 2, 3 \tag{6.28}$$

where τ_i is a threshold for a specified false alarm rate. For the given $\sum_0$ and $\sum_1$, all the γ^0 coefficients in Equation (6.18) that correspond to the hypothesis H_0, are zero.

However, the γ^1s coefficients, which correspond to the H_1 hypothesis, may not be zero [97]. There are three second-order coefficients and one third-order coefficient to be determined. The second-order coefficients under H_1 are given by:

$$\gamma_{ij}^1 = E(z_i^1 z_j^1) = \frac{E(u_i u_j|H_1) - (1-P_M)^2}{P_M(1-P_M)} \ , \ i < j < 3 \tag{6.29}$$

where

$$P_M = \frac{1}{\sqrt{2\pi}} \int_{-\infty}^{r-m} e^{-t^2/2} dt \tag{6.30}$$

and

$$E(u_i u_j|H_1) = P(y_i \geq \tau_i, \ y_j \geq \tau_i|H_1) \tag{6.31}$$

The third-order correlation coefficient under the hypothesis H_1 is given by:

$$\gamma_{123}^1 = E(z_1^1 z_2^1 z_3^1) = E\left(\prod_{i=1}^{3} \frac{u_i - (1-P_M)}{\sqrt{P_M(1-P_M)}} \Big| H_1 \right) \tag{6.32}$$

For $m = \sqrt{2\log\lambda_0}$, where $(\lambda_0 \geq 1)$, there exists a closed form for the expectations in Equations (6.31) and (6.32) as defined in [97]. The second and third order expectations are, respectively given by:

$$E(u_i u_j|H_1) = \frac{1}{4} + \frac{1}{2\pi} \sin^{-1} \rho_{ij} \tag{6.33}$$

$$E(u_i u_j u_k|H_1) = \frac{1}{8} + \frac{3}{2\pi}(\sin^{-1} \rho_{12} + \sin^{-1} \rho_{23} + \sin^{-1} \rho_{13}) \tag{6.34}$$

Consequently, the second-order correlation coefficient is given by $\gamma_{ij}^1 = (2/\pi) \sin^{-1} \rho_{ij}$ and the third-order correlation coefficient by $\gamma_{123}^1 = 0$. Therefore, in the vicinity of $m = \sqrt{2\log\lambda_0}$, the third-order correlation coefficient can be ignored [97].

6.3.2 Chow Expansion

Chow expansion is another interesting class of pdf estimation, which is used to approximate the joint probability distribution of correlated decisions. The joint probability distribution in this case is based on an identity, that is

$$\begin{aligned} P(U) &= P(u_1, u_2, \cdots, u_n) \\ &= P(u_1)P(u_2|u_1)\cdots P(u_n|u_{n-1}, \ldots, u_2, u_1) \\ &= P(u_1)\prod_{i=2}^{n} P(u_i|u_{j(i)}) \end{aligned} \tag{6.35}$$

where $u_{j(i)} = u_1, u_2, \cdots, u_{i-1}$. If we substitute 0 and 1 for u_i and $u_{j(i)}$, we can verify that

$$P(u_i|u_{j(i)}) = \left[p_{i|j(i)}^{u_i}(1-p_{i|j(i)})^{1-u_i}\right]^{u_{j(i)}} \left[p_i^{u_i}(1-p_i)^{1-u_i}\right]^{1-u_{j(i)}} \tag{6.36}$$

where $p_{i|j(i)} = P(u_i = 1|u_{j(i)} = 1)$ and $p_i = P(u_i = 1|u_{j(i)} = 0)$. Substituting Equation (6.36) into Equation (6.35), taking the logarithm and collecting like terms, we obtain the Chow expansion as given in [102].

$$\begin{aligned} \log P(U) = &\sum_{i=1}^{n} \log(1-p_i) + \sum_{i=1}^{n} u_i \log \tfrac{p_i}{1-p_i} \\ + &\sum_{i=2}^{n} u_{j(i)} \log \tfrac{1-p_{i|j(i)}}{1-p_i} + \sum_{i=2}^{n} u_i u_{j(i)} \log \tfrac{p_{i|j(i)}(1-p_i)}{p_i(1-p_{i|j(i)})} \end{aligned} \tag{6.37}$$

Considering Equation (6.37), and the conditional probabilities under the null, $P(U|H_0)$, and alternative, $P(U|H_1)$, hypotheses, the log-likelihood ratio can be expressed as:

$$\begin{aligned} \log \tfrac{P(U|H_1)}{P(U|H_0)} &= \sum_{i=1}^{n} \log \tfrac{(1-p_i)}{(1-q_i)} + \sum_{i=1}^{n} u_i \log \tfrac{p_i(1-q_i)}{q_i(1-p_i)} + \sum_{i=2}^{n} u_{j(i)} \left(\log \tfrac{1-p_{i|j(i)}}{1-q_{i|j(i)}} - \log \tfrac{1-p_i}{1-q_i}\right) \\ &+ \sum_{i=2}^{n} u_i.u_{j(i)} \left(\log \tfrac{p_{i|j(i)}(1-q_{i|j(i)})}{q_{i|j(i)}(1-p_{i|j(i)})} - \log \tfrac{p_i(1-q_i)}{q_i(1-p_i)}\right) \underset{H_0}{\overset{H_1}{\gtrless}} \log \tfrac{P(H_1)}{P(H_0)} \end{aligned} \tag{6.38}$$

In Equation (6.38), we note that if the decisions are indeed independent, $p_i = p_{i|j(i)}$, then the last two sums in the expansion disappear. The remaining two sums belong to a familiar expansion of the independent case similar to the Chair and Varshney rule [93]. When dependence exists, we obtain additional linear and quadratic terms.

Rearranging the terms in Equation (6.38), we obtain a simplified form of the optimal fusion rule based on the MAP or minimum probability detection rule as defined in [87, 88, 95].

$$\log \lambda(U) = W_0 + \sum_{i=1}^{n} W_{1i} u_i + \sum_{i=2}^{n} W_{2i} u_{j(i)} \tag{6.39}$$

where the weights are defined as:

$$W_0 = \sum_{i=1}^{n} \log \frac{(1-p_i)}{(1-q_i)} \tag{6.40}$$

$$W_{1i} = \log \frac{p_i(1-q_i)}{q_i(1-p_i)} \tag{6.41}$$

$$W_{2i} = \begin{cases} \log \frac{(1-q_i)(1-p_{i|j})}{(1-p_i)(1-q_{i|j})} & \text{if } u_i = 0 \\ \log \frac{q_i p_{i|j}}{p_i q_{i|j}} & \text{if } u_i = 1 \end{cases} \tag{6.42}$$

and the conditional probabilities are defined as:

$$\begin{aligned} p_{i|j} &= P(u_i = 1 | u_{j(i)} = 1, H_1) \\ q_{i|j} &= P(u_i = 1 | u_{j(i)} = 1, H_0) \end{aligned} \tag{6.43}$$

The conditional probabilities defined in Equation (6.43) can be rewritten as:

$$p_{i|j} = P(u_i = 1 | u_{j(i)} = 1, H_1) = \frac{P(u_i = 1, u_{j(i)} = 1 | H_1)}{P(u_{j(i)} = 1 | H_1)} \tag{6.44a}$$

$$q_{i|j} = P(u_i = 1 | u_{j(i)} = 1, H_0) = \frac{P(u_i = 1, u_{j(i)} = 1 | H_0)}{P(u_{j(i)} = 1 | H_0)} \tag{6.44b}$$

Let $p_{i,j(i)} = P(u_i = 1, u_{j(i)} = 1 | H_1)$ and $p_{j(i)} = P(u_{j(i)} = 1 | H_1)$, then for $i = 2, \ldots, n$, the two probabilities are related as:

$$p_{j(i+1)} = p_{i,j(i)} \text{ and } q_{j(i+1)} = q_{i,j(i)} \tag{6.45}$$

Therefore, from Equation (6.44) and (6.45), we can generalize

$$p_{i|j} = \frac{p_{i,j(i)}}{p_{i-1,j(i-1)}} \text{ and } q_{i|j} = \frac{q_{i,j(i)}}{q_{i-1,j(i-1)}} \tag{6.46}$$

Since the weights in Equation (6.42) are related in a recursive manner [95], let $m_{k,h}$ be defined as the number of $(u_1, u_2, \cdots, u_{k-1}, u_k = 1, H_h)$ occur for $h = 0, 1$ and $i = 2, 3, \ldots, n$. Then Equation (6.46) can be rewritten as:

$$p_{i|j} = \frac{m_{i,1}}{m_{i-1,1}} \text{ and } q_{i|j} = \frac{m_{i,0}}{m_{i-1,0}} \tag{6.47}$$

Correspondingly, the weights in Equation (6.42) are given by:

$$W_{2i} = \begin{cases} \log\left(\frac{1-q_i}{1-p_i}\right) + \log\frac{m_{i-1,0}}{m_{i-1,1}} + \log\frac{m_{i-1,1}-m_{i,1}}{m_{i-1,0}-m_{i,0}} & u_i = 0 \\ \log\frac{q_i}{p_i} + \log\frac{m_{i-1,0}}{m_{i-1,1}} + \log\frac{m_{i,1}}{m_{i,0}} & u_i = 1 \end{cases} \tag{6.48}$$

6.4 Fuzzy Set Based Decision Fusion

Fuzzy set theory is the basis of fuzzy logic and was introduced by Lotfi Zadeh in 1965 [90]. It is specifically designed to mathematically represent uncertainty and vagueness with formalized logical tools. It helps to deal with the imprecision inherent in many real-world problems. Fuzzy logic is a valuable tool used to make decisions and accommodates imprecise states or variables. Each fuzzy set has an associated membership function to provide a representation of its scope and boundary. A variable of a fuzzy set takes on a membership value between 0 and 1, with 0 indicating the variable is not in that state and 1 indicating it is completely in the specified state.

Fuzzy rules specify logic inferences in the form of IF-THEN statements, which are also often referred to as fuzzy rule-base. The basic algorithm is that the AND operation returns the minimum value of its two arguments, and the OR operation returns the maximum value of its two arguments. The output fuzzy set is defuzzified to convert the fuzzy values, produced by the consequent membership functions, into a fixed and discrete output.

6.4.1 Fuzzy Conceptual Model

The conceptual model of a fuzzy system consists of three processing steps as shown in Figure 6.2. The first step is creating a fuzzy system, i.e., “fuzzification” or changing the crisp binary values into a continuous grading values between 0 and 1. This basically means applying fuzzy membership functions and assigning group membership values to input data. The second step is to apply fuzzy set logic combined with knowledge about the system and to make a set of inferences and associations between members in various groups. The last step is “defuzzification” of the inferences and reaching at a decision representing the output of the fuzzy system.

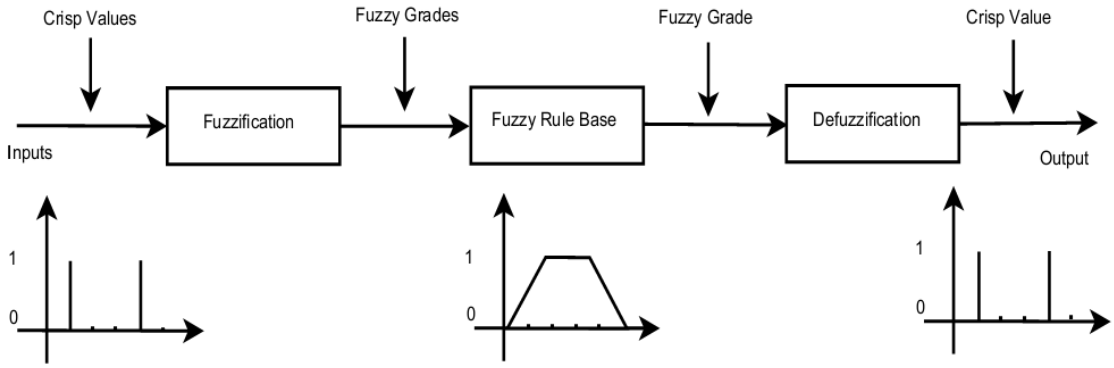

Figure 6.2. Computational model of fuzzy fusion process

Fuzzification Scheme

The fuzzification scheme is the process of applying and assigning membership functions to crisp inputs. The membership function is a grading, which ranges between 0 and 1 [103]. It has a shape of continuous curves such as trapezoidal, triangular or exponential s-shaped curves. Here, we use a moving average of size W to fuzzify the crisp inputs. W is related to the size of the landmine and to the allowable degree of vagueness. The degree of vagueness affects the performance of the fusion process. The vagueness should be large in order not to miss the targets, but small enough to minimize the occurrence of false alarms. A window of width W will have a vagueness order or grading step size of $1/W$. A trapezoidal membership function, μ_j of the j^{th} source, is generated using moving average as:

$$\mu_j(k) = \frac{1}{W} \sum_{k=-\frac{W-1}{2}}^{k+\frac{W-1}{2}} u_j(k) \tag{6.49}$$

where $u_j(k)$ is the k^{th} decision of detector j. Various shapes of commonly used membership functions are given in Figure 6.3.

Fuzzy Rule-Base

The fuzzy rule-base is the core of fuzzy system, which contains mainly a set of IF-THEN implication rules. After the fuzzification and generation of the membership functions, some rule-base function is applied to fuse the local decisions. In this thesis, a generalized mean is applied as fuzzy rule-base to aggregate the decisions at the FC, as will be discussed in Section 6.4.2.

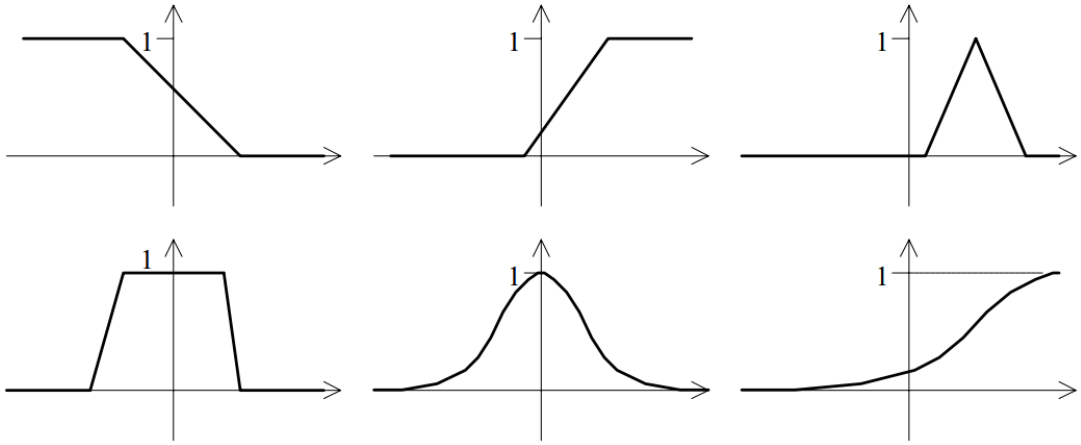

Figure 6.3. Shapes of commonly used membership functions

For the decision fusion problem, which constitutes a multiple-inputs, single-output (MISO) system, the general fuzzy logic description is given by a weighted average of the membership functions. The weights depend on the relative importance of the detectors. If the detectors are equally likely, an equal weighting may be used. In this scheme, all the inputs and outputs are fuzzy.

Defuzzification Scheme

The

$$\begin{aligned} H_1: &\quad \mu_u(u_0) \geq 0.5 \\ H_0: &\quad \mu_u(u_0) < 0.5 \end{aligned} \tag{6.50}$$

where $\mu_u(u_0)$ is the membership function of the global decision.

6.4.2 Decision Fusion Approach

The fuzzy set approach provides many advantages due to the fact that there are numerous ways of combining data in addition to the union and intersection operations. Usually, in decision making based on several criteria, a certain amount of compensation is desirable [104]. Human decisions and evaluations always show some degree of compensation. The generalized mean also shows some compensation, which closely

matches the human decision making process. For the trapezoidal membership functions, $\mu_j(u_j)$, generated from the binary two-valued decisions, the generalized mean rule-base is given as:

$$M_p(\mu_1(u_1), \mu_2(u_2), \ldots, \mu_n(u_n); p; w'_1, w'_2, \ldots, w'_n) = \left(\sum_{j=1}^{n} w'_j \mu_j^p(u_i) \right)^{\frac{1}{p}} \tag{6.51}$$

where $\mu_j(u_j)$ is membership functions of the decisions u_j, w'_j is the relative importance factors and p is the degree of fuzziness. For different values of p, the generalized mean shows different characteristics as depicted in Table 6.1.

p	$-\infty$	-1	0	1	2	∞
Mp	Intersection	Harmonic mean	Geometric mean	Arithmetic mean	Root-mean -square	Union

Table 6.1. Behavior of generalized mean for different values of p.

The attractive properties of the generalized mean are explained by assuming any two arbitrary membership functions a, b.

- $\min(a, b) \leq \text{mean}(a, b) \leq \max(a, b)$
- mean increases with increasing value of p; by varying the value of p; between $-\infty$ and ∞, one can obtain all values between 'min' and 'max'.

For two values $[a, b] = [0.1, 0.9]$, the generalized mean plot is depicted in Figure 6.4.

It can be shown that $p = 1$ gives the arithmetic mean, $p = -1$ gives the harmonic mean and $p = 0$ gives the geometric mean. The rate of compensation for the generalized mean can be controlled by changing the value of p. The larger the value of p, the more fuzzy the partition will be.

The choice for the degree of fuzziness depends on the redundancy and the number of sources. For the fusion process, one can choose a larger p value for the fusion of information from complementary sources and a smaller p for the fusion of information from redundant sources. If information about the complementarity/redundancy is not available, we can assume a smaller p for a large number of sources and a larger p for a small number of sources [104].

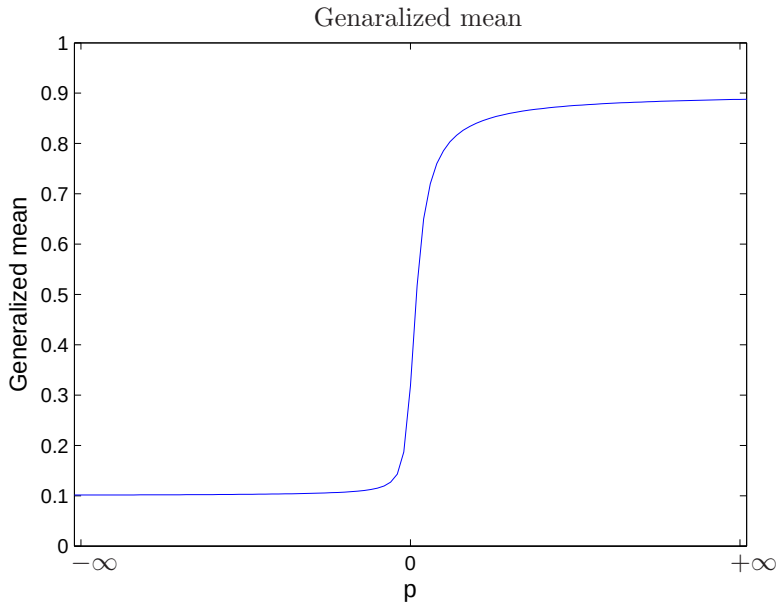

Figure 6.4. Behavior of the generalized mean.

The relative importance factors, w_i' is related to the probability of detection, false alarm and the hypothesis. The sum of the relative importance factors gives unity, i.e., $w_1' + w_2' + \cdots + w_n' = 1$. For the j^{th} detector, the i^{th} weight can be calculated as:

$$w_j(i) = \left(\ln \frac{1 - P_M^j}{P_F^j} u_j(i) + \ln \frac{1 - P_F^j}{P_M^j} (1 - u_j(i)) \right) \tag{6.52}$$

where P_M^j is the probability of missed detection, P_F^j is the probability of false alarm of the j^{th} detector and $u_j(i)$ is the i^{th} decision of the j^{th} detector. The importance factor is then given by:

$$w_j'(i) = \frac{w_j(i)}{\sum_{j=1}^{N} w_j(i)} \tag{6.53}$$

The higher the confidence of the source, the higher the weight assigned during the fusion. If there is no enough information to bias, the weights are assumed to be equally important, i.e., $w_i = 1/N$, where N is number of sources to be fused.

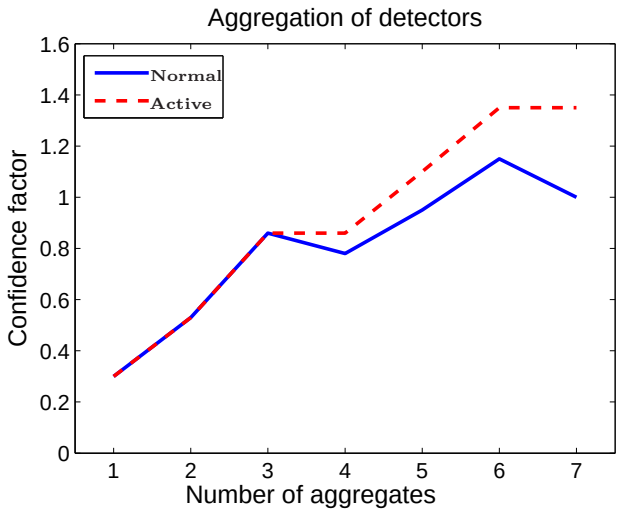

Figure 6.5. Confidence factor of seven detectors.

6.4.3 Aggregation Procedure

The aggregation procedure begins with the fusion of decisions from two detectors and then the confidence factor is calculated. Decisions from a third detector are fused to the existing aggregate. If the confidence factor decreases, decision from this detector is ignored and decision from the other detector is aggregated. The procedure continues till the n^{th} detector is aggregated.

In this case, the confidence factor is defined as:

$$C_f = \frac{1}{e_{av}} \tag{6.54}$$

Then the average error,e_{av} is calculated as:

$$e_{av} = \sum_{i=1}^{r} w_i'(u_0 - u_i)^2,\ 1 < r \leq n \tag{6.55}$$

The weights are the same as the weights used in the fusion process.

Here we have considered an aggregation of seven decisions and the confidence factor is depicted in Figure 6.5. It is clear from the plot that the confidence factor decreases when the 4^{th} and 6^{th} decisions are added. Therefore, decisions from these detectors should be ignored at that given instant.

The final decision has to be obtained by some defuzzification method. An α-cut is the most common and easy method of defuzzification. After fixing the value of α, an α-cut is performed on the aggregated decision.

6.5 Results

Here, we considered for detectors with known probability of detection and false alarm. The detector characteristics and fusion using classical techniques is given in Table 6.2. The fuzzy set operation for different values of p is tabulated in Table 6.3.

	D1	D2	D3	D4	AND	OR	Majority
P_d	0.7960	0.8608	0.8682	0.8850	0.79	0.9120	0.8760
P_{fa}	0.0244	0.0231	0.0159	0.0170	0.0140	0.0245	0.0185

Table 6.2. Fusion using classical techniques.

p	-10	-5	-1	0	1	5	10
P_d	0.8250	0.8483	0.8632	0.8706	0.8806	0.8905	0.9102
P_{fa}	0.0140	0.0152	0.0168	0.0186	0.0202	0.0215	0.0243

Table 6.3. Fuzzy decision fusion for different degrees of fuzziness.

The optimal value of p is chosen by measuring the distance of the point (pfi, pdi) which is close to the left corner, i.e., (0,1) as shown in Figure 6.6. Therefore, in this case the union like operation is optimal.

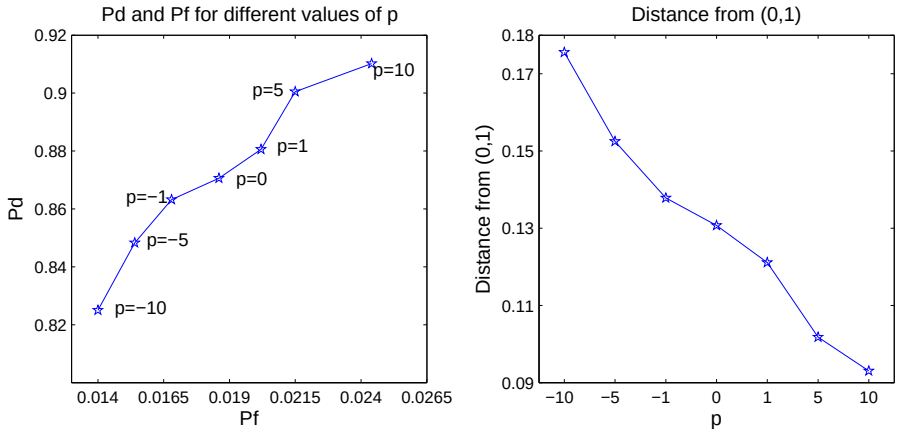

Figure 6.6. Distance measurement for optimal value of p

For a plastic mine laid in wet clay sand, comparison of the three fusion techniques against the best detector, which is the symmetry filtering, is illustrated in Figure 6.7.

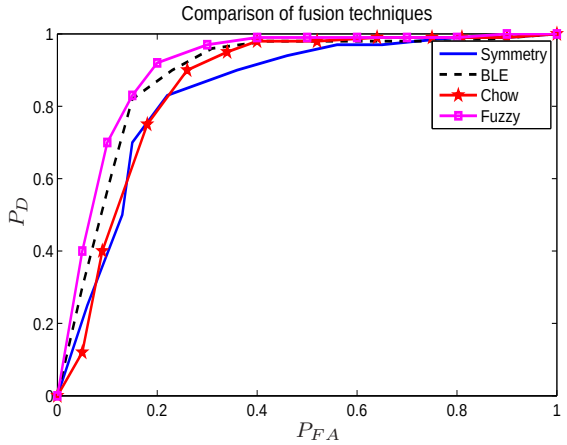

Figure 6.7. Comparison of fusion techniques against the best detector.

6.6 Conclusion

In this chapter, the fusion of local decisions has been considered. After reviewing basic fusion strategies, an optimal correlated decision fusion for n binary decisions using the Bahadur-Lazarsfeld and Chow expansion of probability density functions was derived. These rules use expansions to approximate the probability distribution. In addition, decision fusion based on fuzzy set logic was discussed. In case of BLE, the most general case is to estimate $2(2^n - n - 1)$ correlation coefficients in order to obtain the log-likelihood ratio test. The computational complexity can be greatly simplified assuming most of the correlation coefficients are zero. When all correlations are zero, we obtain the optimal decision fusion for independent local decisions. The complexity of the BLE method increases when the number of detectors increases.

In case of the Chow expansion, the estimation of probability density function is based on the identity of the decision. This method is less difficult in calculating the dependency between the decisions. Moreover, the weights are related in a recursive manner so that an adaptive mechanism is possible to implement.

The fuzzy set based decision approach provides several advantages over other classical techniques. There are numerous ways of combining fuzzy sets in addition to the union or intersection. Trapezoidal membership functions were implemented and a generalized mean was used as a rule-base. It is found that the aggregated function depends on the degree of fuzziness, p. The final binary decision is obtained from the aggregated function by setting an α-cut value of 0.5.

Experimental data showed that all the proposed techniques give rise to performance improvement compared to the classical techniques.

Chapter 7
Conclusions and Future Directions

This thesis has dealt with the problem of detecting buried AP and AT landmines using impulse ground penetrating radar. Weak reflected signals obtained from buried targets are usually obscured by strong clutter, which mainly comes from the interference of surrounding devices, rough ground surfaces, underground inhomogeneities and coupling between the transmitting and receiving antennas. Therefore, reducing or eliminating the clutter signal is of fundamental importance.

The objectives of this work have been to study, develop and compare signal processing techniques as regarding their ability to extract landmine signals from GPR measurements. The main topics covered in this thesis include: EM propagation modeling, clutter reduction techniques, subsurface and target parameter estimation, and fusion of correlated decisions made by the clutter reduction experts.

A summary and the main conclusions of the work performed in this thesis are provided in Section 7.1. Section 7.2 provides an outlook for possible future work.

7.1 Conclusions

7.1.1 GPR EM Wave Propagation Modeling

A multi-layer transmission line modeling approach has been implemented to estimate the EM propagation of GPR in different scenarios. The subsurface ground and the targets are modeled as cascaded layers of distinct electromagnetic properties. Using this approach, it is possible to predict the backscattered signal components in different soil types, for a given antenna frequency. In the course of modeling, metallic and plastic targets were placed shallowly in the ground, and an air-coupled antenna setup was considered. Moreover, the effect of added moisture and multi-reflections in the subsurface layers have been investigated. This modeling approach is easy to understand and effective alternative to the numerical modeling approaches. The proposed modeling technique is tested for different scenarios and shown attractive results.

The proposed modeling approach is relatively easy and allows for the prediction of the GPR return signal for a given scenario.

7.1.2 Subsurface and Target Parameter Estimation

In the area of ground and target parameters estimation, the surface reflection parameter method (SRPM) has been applied. Landmines and clutter components can be classified based on their parameters, such as intrinsic impedance and relative permittivity. We applied the inverse multilayer modeling scheme to estimate parameters of the subsurface ground and buried targets. The method is useful to correctly estimate the parameters of the subsurface and buried plastic landmines by comparing the amplitudes reflected from the interfaces and the incident electric field. Target detection and hypothesis testing are implemented using the test statistics of the estimated parameters. The test statistics are compared against a threshold for the detection problem. It is found that prior knowledge of the antenna height and amplitude of the incident electric field could greatly simplify the problem of parameter estimation. Moreover, for known soil characteristics, the nature of buried plastic landmines could be estimated perfectly.

The proposed approach for subsurface and parameter estimation allows for the detection of buried landmines based on their characteristic properties.

7.1.3 Advanced Signal Processing for Landmine Detection

Several signal processing techniques for discriminating landmines from clutter using GPR measurements have been discussed in detail. These methods have been divided into four categories: background subtraction methods such as scaling and shifting, adaptive and model based clutter estimation; the symmetry filtering algorithm and the decorrelation approach. Moreover, subsurface and target parameter estimation, which are based on inverse multilayer modeling, have been implemented. Finally, in order to improve the detection capacity of the GPR sensor, fusion of correlated decisions made by the signal processing experts has been performed.

The proposed signal processing algorithms are promising for clutter reduction and automatic target detection. The proposed techniques showed superior performance when compared to classical background subtraction techniques. Moreover, preprocessing of measurement data has been shown to be absolutely necessary for many of the clutter reduction algorithms.

7.1.4 Decision Fusion

Cooperation among detectors could improve the detection capacity of the detector. For this objective, three correlated decision fusion experts have been implemented. Two of the techniques were optimal which are based on the Bahadur-Lazarsfeld and Chow expansions. However, the third suboptimal technique is based on fuzzy set operations.

The proposed scheme allows for the fusion of correlated local decisions. The proposed techniques optimally fuse the decisions coming from many signal processing experts so as to improve the detection capacity of the sensor.

7.2 Future Work

The humanitarian demining technologies in use today remain quite crude, with the common metal detector and basic, manual prodding used almost universally. Clearly, a metal detector is ineffective with non-metallic landmines, so the operator is still constrained to manually prod for such mines. The research presented in this dissertation has advanced the effectiveness of GPR techniques for landmine detection, but much additional research is still needed.

7.2.1 Multilayer Inverse Modeling

In the inverse modeling based target and subsurface estimation, we have made many assumptions to simplify the problem. These assumptions were the main causes for the estimation errors. Assumptions, such as the subsurface ground and the targets being lossless are practically not correct. A realistic inverse modeling of a lossy subsurface and targets should be considered. Advanced robust techniques, which can fully estimate the subsurface and target parameters, should be developed.

7.2.2 Clutter Reduction

The clutter reduction techniques considered in this thesis were effective, however, there are also many effective techniques such as Kalman filtering, ICA, one-sided and two-sided linear prediction techniques, and time-frequency distribution. In addition, the

symmetry filtering technique considered in this thesis is effective in discriminating targets and friendly objects based on their geometry, but requires the preprocessing of the measured data. It is possible to improve the effectiveness of the technique by removing the use of preprocessing techniques.

The decorrelation, adaptive background subtraction and model based background subtraction algorithms developed here show promise when applied to raw GPR data which has not been preprocessed for clutter removal. Our feature work will include the application of time-frequency, wavelet packet decomposition and Kalman filtering techniques for target detection and discrimination purposes.

7.2.3 Decision Fusion

In this thesis, we have restricted our selves to optimal decision fusion techniques. Moreover, the techniques need the knowledge of prior probabilities of the detectors which is sometimes not possible to acquire. Our future work will focus on the application of adaptive correlated decision fusion techniques, where the prior probabilities will be obtained using adaptive techniques. Moreover, we will develop techniques to estimate higher-order correlation coefficients in the case of BLE. The fuzzy set based technique was sub optimal. However, it is possible to include optimization techniques and our future work will consider this.

Appendix A
Additional Real Data Analysis Results for Chapter 4.

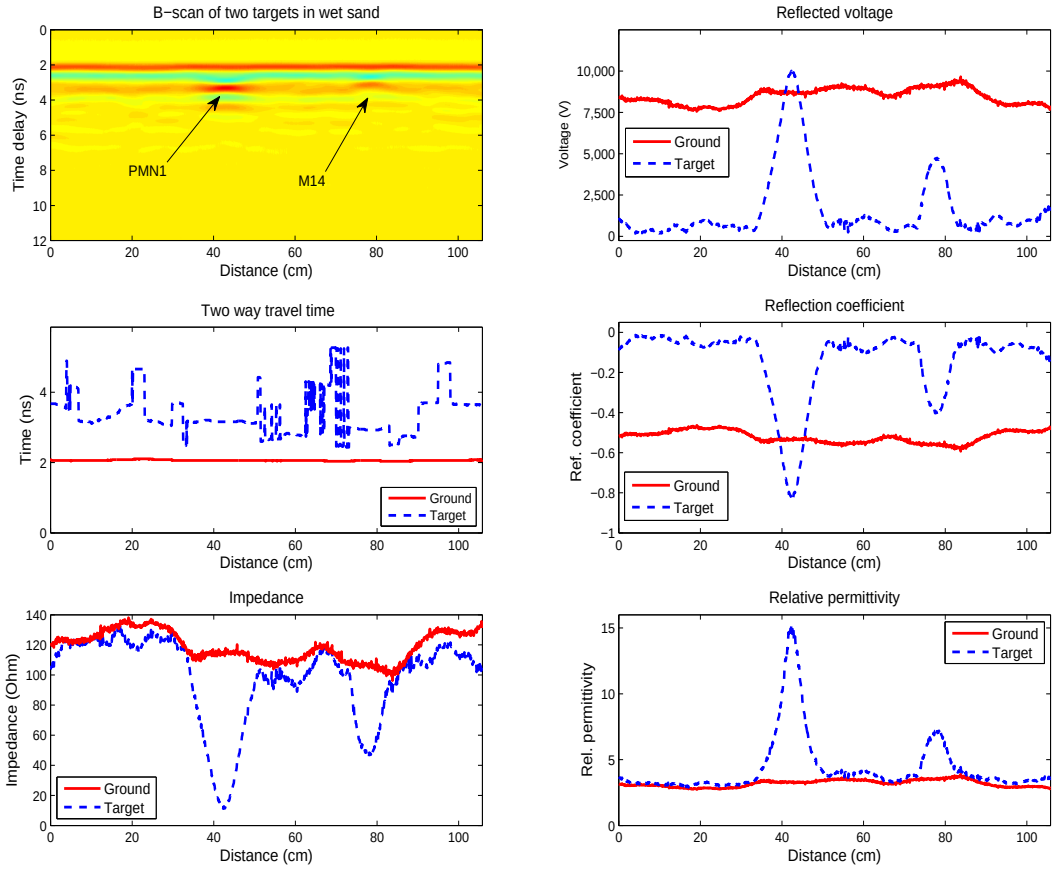

Figure A.1. Two plastic targets, PMN1 and M14, placed in sand soil and estimated parameters: ground layer (solid line) and target (dash line).

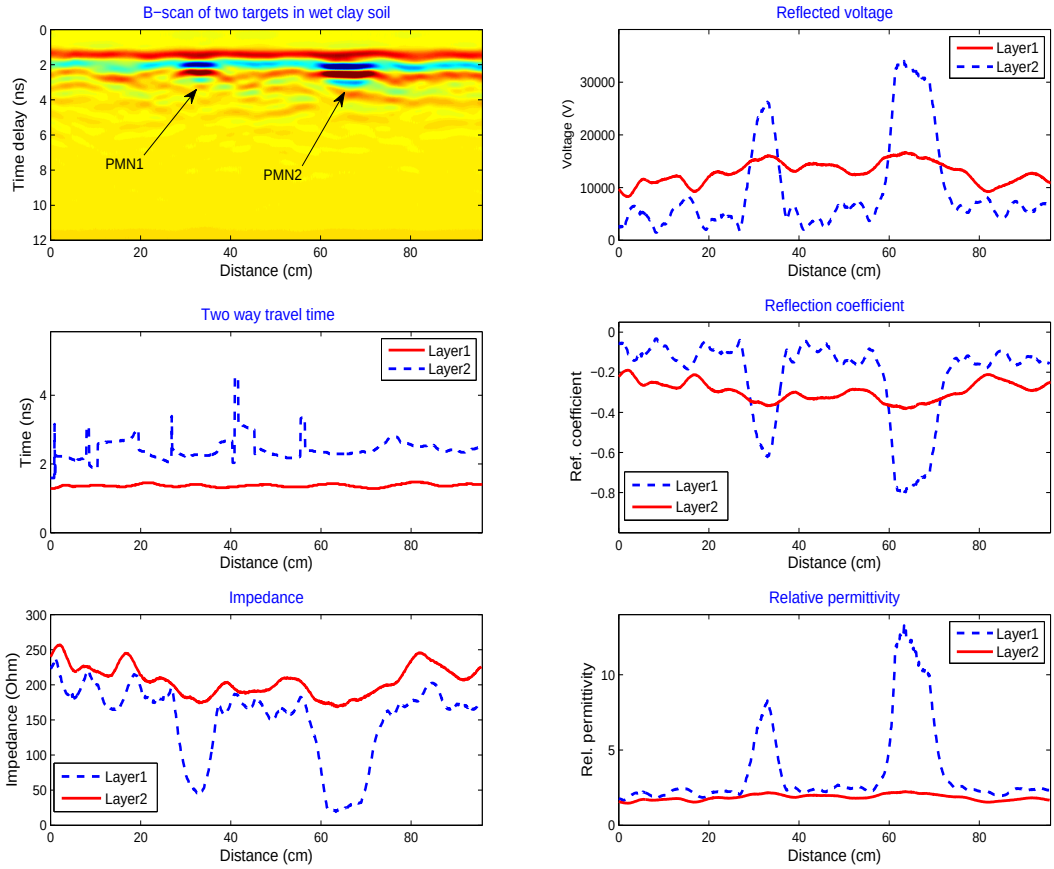

Figure A.2. Two targets, PMN1 and PMN2, placed in wet clay soil and estimated parameters: ground layer (solid line) and target (dash line).

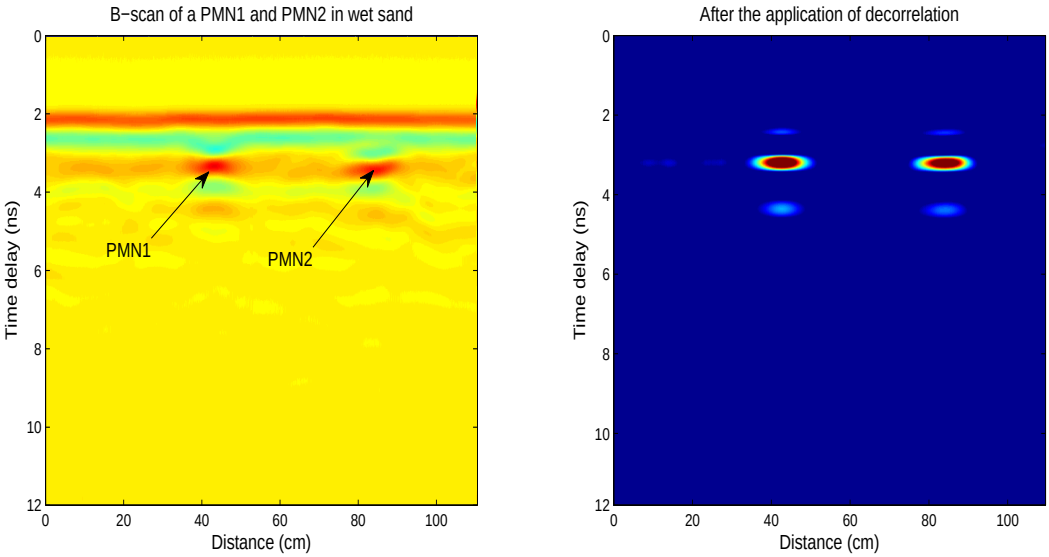

Figure A.3. Left: Raw radargram data, Right: After decorrelation.

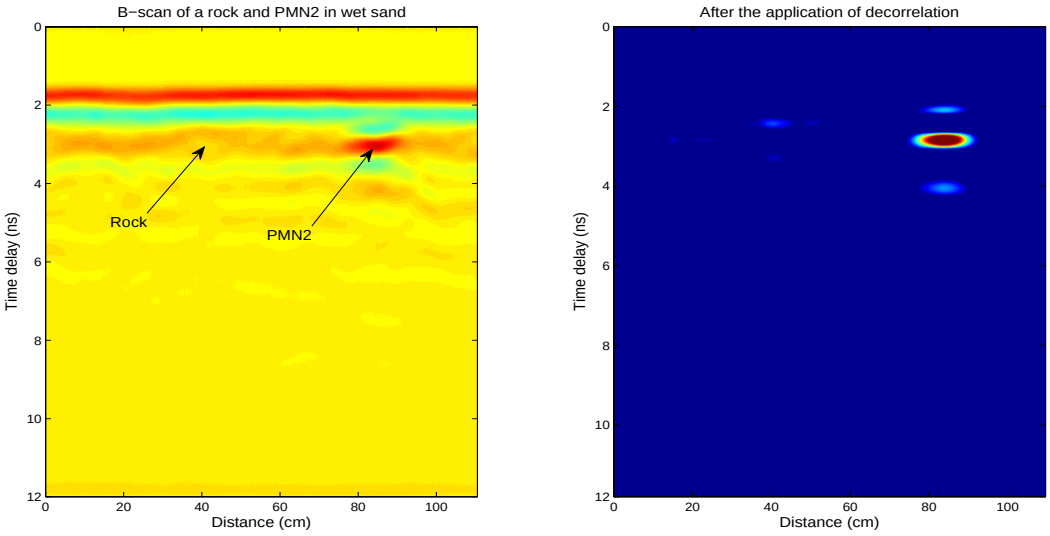

Figure A.4. Left: Raw radargram data, Right: After decorrelation.

List of Acronyms

ARMA	Autoregressive Moving Average
AT	Anti Tank
AP	Anti Personnel
BLE	Bahadur - Lazarfeld Expansion
CRIM	Composite Refractive Index Method
EMI	Electromagnetic Induction
ERW	Explosive Remnants of War
FAR	False Alarm Rate
FC	Fusion Center
GLRT	Generalized Likelihood Ratio Test
GSSI	Geophysical Survey Systems Inc
GPR	Ground Penetrating Radar
LRT	Likelihood Ratio Test
LTI	Linear Time Invariant
KLT	Karhunen-Loéve Transform
MAP	Maximum Apriori
MD	Metal Detector
ML	Maximum Likelihood
NP	Neyman-Pearson
NQR	Nuclear Quadrupole Resonance
PCA	Principal Component Analysis
PD	Probability of Detection
pdf	probability density function
RCS	Radar Cross Section

RDX	Royal Demolition Explosive
ROC	Receiver Operating Characteristic
SRPM	Surface Reflection Parameter Method
SNR	Signal to Noise Ratio
TL	Transmission Line
TNT	Trinitrotoluene
TI	Thermal Imaging
UXO	Unexploded Ordinance

List of Symbols

ω	Angular frequency	rad(s^{-1})
ε	Absolute permittivity	F/m
ε_0	Free space permittivity	F/m
ε_r	Relative permittivity	
μ	Absolute magnetic permeability	H/m
μ_0	Free space magnetic permeability	H/m
μ_r	Relative permeability	
μ_y	Sample mean vector of measured data	
γ	Propagation coefficient/ constant	
$\Gamma_{i,j}$	Reflection coefficient from $i-j$ interface	
$\hat{b}(t,x)$	Background estimation signal	
y_{ref}	Background reference signal	
$g(t)$	One-dimensional radar function	
$g(x,t)$	Two-dimensional radar function	
$g(x,y,t)$	Three-dimensional radar function	
$y(t,x)$	Received GPR data	
f_i	Fractional volume of components in a mixture	
τ	Pulse width of a radar system	s
t^*	Estimated arrival time of the air-ground interface	s
t_{off}	Time offset between the zero-time and zero-ground	s
$t_d(n,x)$	Pulse echo time delay of the n^{th} layer	s
$t_r(n)$	Travel time of the n^{th} layer	s
E_{pi}	Peak electric field reflected from the i^{th} layer	
E_{ri}	Composite electric field reflected from the i^{th} layer	
$\hat{h}_a$	Estimated antenna height	
$T_{me}(x)$	Test statistic for estimation error	
$T_{vs}(x)$	Test statistic for voltage test	
$T_{rs}(x)$	Test statistic for reflection coefficient test	
$T_{ps}(x)$	Test statistic for voltage permittivity	
T	Transformation function for KLT	
α	Attenuation coefficient/ constant	NP/m
α_k	Exponential factor of exponential moving average	
α_s	Significance level	

β	Phase coefficient	
η_0	Intrinsic impedance	Ω/m
Z	Characteristic impedance	Ω/m
$\mathbf{H}$	Magnetic field intensity	A/m
$\mathbf{E}$	Electric field intensity	V/m
$\mathbf{J}$	Current density	$\mathrm{A/m^2}$
$\mathbf{D}$	Electric field displacement	$\mathrm{C/m^2}$
$\mathbf{B}$	Magnetic field displacement	$\mathrm{Wb/m^2}$
ρ	Charge density	$\mathrm{C/m^3}$
ρ_{ij}	covariance between i and j decision vectors	
v	Wave velocity	m/s
$w(t, f)$	Wavelet function	
$\mathbf{f}$	Echo time delta function	
P_{tr}	Transmission-reflection product	
$T_{i,j}$	Transmission coefficient from $i - j$ interface	
ε^e_{mix}	Effective permittivity of a mixture	
ε^*_e	Effective complex permittivity	
J_0	Point of symmetry	
Ψ	Residual covariance matrix	
U	Decision vector	
$u(i, j)$	Preprocessed radargram	
u_i	Binary decision variable	
u_0	Variable for the global decision	
$\gamma_{12\ldots n}$	n^{th} order correlation coefficient	
$\gamma^h_{12\ldots n}$	n^{th} order correlation coefficient under hypothesis H_h	
C_f	Confidence factor of an aggregation	
φ_i	Bahadur-Lazarfeld polynomial	
f_s	Sampling frequency	
V_r	Vertical resolution	
H_r	Horizontal resolution	
θ_i	Angle of incidence	
θ_t	Angle of refraction	
p	Degree of fuzziness	
w'_i	Relative importance factor	
μ_i	Membership function of decision i	

Bibliography

[1] Mines Action Canada, Action on Armed Violence, Handicap International, Human Rights Watch, and Norwegian Peoples Aid, "Landmine report 2009," *Special ten-year review of the mine ban treaty*, pp. 1–1276, October 2009.

[2] Mines Action Canada, Action on Armed Violence, Handicap International, Human Rights Watch, and Norwegian Peoples Aid, "Landmine report 2010," *Mine Action Canada*, pp. 1–78, October 2010.

[3] Mines Action Canada, Action on Armed Violence, Handicap International, Human Rights Watch, and Norwegian Peoples Aid, "Landmine report 2011," *Mine Action Canada*, pp. 1–82, October 2011.

[4] Mines Action Canada, Action on Armed Violence, Handicap International, Human Rights Watch, and Norwegian Peoples Aid, "Landmine report 2012," *Landmine and Cluster Munition Monitor*, pp. 1–78, November 2012.

[5] Luke A. Cirillo, Christopher L. Brown, and Abdelhak M. Zoubir, "Polynomial phase signal based detection of buried landmine using ground penetration radar," *Proceedings of the IEEE 11th Signal Processing Workshop on Statistical Signal Processing*, pp. 166–169, 2001.

[6] Maki K. Habib, "Humanitarian demining mine detection and sensors," *IEEE International Symposium on Industrial Electronics (ISIE)*, pp. 2237–2242, 2011.

[7] Esam M.A. Hussein and Edward J. Waller, "Landmine detection: The problem and the challenge," *Applied Radiation and Isotopes*, vol. 55, pp. 557–563, September 2000.

[8] Katsuhisa Furuta and Jun Ishikawa, *Anti-personal Landmine Detection for Humanitarian Demining*, Springer-Verlag London Limited, 2009.

[9] Abdelhak M. Zoubir, Ian James Chant, Christopher L. Brown, Braham Barkat, and Canicious Abeynayake, "Signal processing techniques for landmine detection using impulse ground penetrating radar," *IEEE Sensor Journal*, vol. 2, no. 1, pp. 41–51, February 2002.

[10] David J. Daniels, Paul Curtis, and Oliver Lockwood, "Classification of landmines using gpr," *IEEE Proceedings of International Radar Conference, RADAR '08.*, pp. 1–6, May 2008.

[11] Nicolas E. Walsh and Wendy S. Walsh, "Rehabilitation of landmine victims the ultimate challenge," *Bulletin of the World Health Organization*, vol. 81, no. 2, pp. 665–670, February 2003.

[12] UN Landmine Department, "Landmine facts," February 2002.

[13] Maki K. Habib, *Humanitarian Demining Innovative Solutions and the Challenges of Technology*, I-Tech Education and Publishing Vienna, Austria, first edition, February 2008.

[14] Xiaoyin Xu, Eric L. Miller, Carey M. Rappaport, and Gary D. Sower, "Statistical method to detect subsurface objects using array ground-penetrating radar data," *IEEE Transactions on Geoscience and Remote Sensing*, vol. 40, no. 4, pp. 963–976, April 2002.

[15] Jacqueline MacDonald, J.R. Lockwood, John McFee, Thomas Altshuler, Thomas Broach, Lawrence Carin, Russell Harmon, Carey Rappaport, Waymond Scott, and Richard Weaver, "Alternatives for landmine detection," *RAND Science and Technology policy Institute*, 2003.

[16] David J. Daniels, *Ground Penetrating Radar*, The Institution of Electrical Engineers, UK, second edition, 2004.

[17] Harry M. Jol, *Ground Penetration Radar Theory and Application*, vol. 1, Elsevier B. V., first edition, 2009.

[18] Claudio Bruschini and Bertrand Gros, "A survey of research on sensor technology for landmine detection," *Journal of Humanitarian Demining*, 1998.

[19] A.G. Yarovoy, V. Kovalenko, F. Roth, E. Ligthart, A. Fogar, and L. Ligthart, "Landmine detection and discrimination based on gpr data," *IEEE Tenth International Conference on Ground Penetrating Radar*, vol. 40, no. 4, June 2004.

[20] David Kerner, John Deni, Joseph Grubb, Churchill Hutton, Richard Johnson, and Thomas Kincaid, "Anti-personnel landmine (apl) detection technology survey and assessment," *Technical report: Defense Threat reduction Agency*, March 1999.

[21] Gerald Oßberger, Thomas Buchegger, Erwin Schimbäck, Reimar Pfeil, Andreas Stelzer, and Robert Weigel, "Adaptive ground clutter removal algorithm for ground penetrating radar applications in harsh environments," *Sensing and Imaging: An International Journal*, vol. 7, no. 3, pp. 71–89, September 2006.

[22] Kostyleva V.V., Smirnov A.B., Nikolayev V.A., and Medvedev S.P., "Based on two-port network theory simulation of electromagnetic wave propagation in multilayer medium," *Second International Workshop on Ultrawideband and Ultrashort Impulse Signals*, pp. 176–178, September 2004.

[23] Martin Lapinski and Pawel Kaczmarek, "Multilayer time domain transmission line model," *17th International Conference on Microwaves, Radar and Wireless Communications (MIKON 2008)*, pp. 1–4, 2008.

[24] Thomas P., Weldon, and Ammar Y. Rathore, "Wave propagation model and simulations for landmine detection," *Technical report, North Carolina University at Charlotte Department of Electrical Engineering*, pp. 1–17, March 1999.

[25] Yarovoy A.G. and Ligthart L.P., "Uwb radars for challenging applications," *The Third International Conference on Ultrawideband and Ultrashort Impulse Signals*, pp. 50–55, September 2006.

[26] A.G. Yarovoy, P. van Genderen, and L.P. Ligthart, "Ground penetrating impulse radar for landmine detection," *Proceedings of SPIE, 8th international Conference on Ground Penetrating Radar*, pp. 1–5, April 2007.

[27] Alvaro M. Mayordomo and Alexander G. Yarovoy, "Optimal background subtraction in gpr for humanitarian demining," *Proceedings of the 5th European Radar Conference*, p. 4, October 2008.

[28] Fawzy Abujarad, Andreas Jöstingmeier, and A.S. Omar, "Clutter removal for landmine using different signal processing techniques," *Tenth Intenational Conference on Ground Penetrating Radar*, pp. 697–700, June 2004.

[29] Dragana Carevic, "A kalman filter-based approach to target detection and target background separation in ground penetrating radar data," *Electronics and Surveillance Research Laboratory DSTO-TR 0853*, vol. 1, no. 1, 2000.

[30] van Kempen L. and H. Sahli, "Ground penetrating radar data processing: a selective survey of the state of the art literature," *November*, pp. 1–38, 1999.

[31] Hichem Sahli John W . Brooks, Luc van Kempen, "Ground penetrating radar data processing: clutter characterization and removal," *Proc. of the 11th IEEE Workshop on Statistical Signal Processing*, pp. 158–161, 1999.

[32] Galal Nadim, "Clutter reduction and detection of landmine objects in ground penetrating radar data using likelihood method," *Proceedings of ISCCSP 2008*, pp. 98–106, March 2008.

[33] Stephane Penin, Alain Bibaut, Emmanuel Duflo, and Philippe Vanheeghe, "Use of wavelets for ground-penetrating radar signal analysis and multi-sensor fusion in the frame of landmines detection," *IEEE International Conference on Systems, Man and Cybernetics*, vol. 4, pp. 2940–2945, 2000.

[34] Ping Gao, Stacy Tantum, and Leslie Collins, "Statistical signal processing techniques for the detection of low-metal landmines using em1 and gpr sensors," *IEEE Proceedings of International Symposium on Geoscience and Remote Sensing IGARSS '99*, vol. 5, pp. 2465–2467, 1999.

[35] K.C. Ho, Leslie M. Collins, Lisa G. Huettel, and Paul D. Gader, "Discrimination mode processing for emi and gpr sensors for hand-held land mine detection," *IEEE Transactions on Geoscience and Remote Sensing*, vol. 42, no. 1, pp. 2465–2467, January 2004.

[36] Akgn S., Azak Mustafa D., Samedov S., and R.K aputu, "Buried object detection-em1 and ir sensors," *Proceedings of the 12th IEEE on Signal Processing and Communications Applications*, pp. 668–671, 2004.

[37] Zakarya Zyada, Yasuhiro Kawai, Takayuki Matsuno, and Toshio Fukuda, "Sensor fusion based fuzzy rules learning for humanitarian mine detection," *SICE-ICASE International Joint Conference*, pp. 1860–1865, October 2006.

[38] V. Kovalenko, A. Yarovoy, and L.P. Ligthart, "Polarimetric feature fusion in gpr for landmine detection," *IEEE International Symposium on Geoscience and Remote Sensing IGARSS 2007*, pp. 30–33, 2007.

[39] Gebremichael T. Tesfamariam, Abdelhak M. Zoubir, and Dilip S. Mali, "Fusion of correlated decisions for gpr based plastic landmine detection," *Proceedings of 14th IEEE international conference on GPR*, pp. 1–43, April 2012.

[40] van Kempen L. and H. Sahli, "Signal processing techniques for clutter parameters estimation and clutter removal in gpr data for landmine detection," *Proceedings of the 11th IEEE Workshop on Statistical Signal Processing*, pp. 158–161, 2001.

[41] Gebremichael T. Tesfamariam and Abdelhak M. Zoubir, "Advanced background subtraction techniques for gpr based landmine detection applications," *7th European Radar Conference*, July 2013.

[42] Jonathon C. Ralston and David W. Hainsworth, "Application of ground penetrating radar for coal depth measurement," *Proceedings of IEEE International Conference on Acoustics, Speech and Signal Processing*, 1999.

[43] Andrew D. Strange, Jonathon C. Ralston, and Vinod Chandran, "Application of ground penetrating radar technology for near-surface interface determination in coal mining," *IEEE International Conference on Acoustics, Speech and Signal Processing, 2005. Proceedings. (ICASSP '05)*, pp. 701–705, March 2005.

[44] Yuan Luo and Guang-You Fang, "Gpr clutter reduction and buried targetdetection by improved kalman filter technique," *Proceedings of the 4th International Conference on Machine Learning and Cybernetics,Guangzhou*, August 2005.

[45] Dragana Carevic, "Clutter reduction and detection of mine like objects in ground penetrating radar data using wavelets," *Subsurface Sensing Technologies and Applications*, vol. 1, no. 1, 2000.

[46] Quan Fu, Yalin Li, Huarui Yin, and Peixia Xu, "Uwb signal detection based on wavelet packet decomposition," *4th International Conference on Wireless Communications, Networking and Mobile Computing, WiCOM,08*, 2008.

[47] Fawzy Abujarad, Gala1 Nadimi, and Abbas Omar, "Wavelet packets for gpr detection of non-metallic anti-personnel land mines based on higher-order-statistic," *Proceedings of the 3rd International Workshop on Advanced Ground Penetrating Radar, IWAGPR 2005*, pp. 21–26, 2005.

[48] Hui-Lin Zhou, Mao Tian, and Xiao-Li Chen, "Time-frequency representations for classification of ground penetrating radar echo signal," *Proceedings of 2005 International Symposium on Intelligent Signal Processing and Communication Systems*, December 2005.

[49] O. Lopera, N. Milisavljevi, D. Daniels, and B. Macqt, "Time frequency domain signature analysis of gpr data for landmine identification," *4th International Workshop on Advanced Ground Penetrating Radar*, June 2007.

[50] Brham Barkat, Abdelhak M. Zoubir, and C.L. Brown, "Application of time-frequency techniques for the detection of anti-personnel landmines," *Proceedings of the Tenth IEEE Workshop on Statistical Signal and Array Processing*, pp. 294–297, 2000.

[51] Huilin Zhou and Yuhao Wang, "Time frequency representations for classification of landmine using uwb impulse gpr," *4th International Workshop on Wireless Communications, Networking and Mobile Computing, WiCOM '08*, 2008.

[52] Timofey Grigorievich Savelyev, Luc van Kempen, Hichem Sahli, Juergen Sachs, and Motoyuki Sato, "Investigation of timefrequency features for gpr landmine discrimination," *IEEE Transactions on Geoscience and Remote Sensing*, vol. 45, no. 1, January 2007.

[53] Anxing Zhao, Yansheng Jiang, and Wenbing Wang, "Exploring independent component analysis for gpr signal processing," *Progress In Electromagnetics Research Symposium, Hangzhou, China*, pp. 750–753, August 2005.

[54] William Ng, Thomas C.T. Chan, H.C. So, and K.C. Ho, "On particle filters for landmine detection using impulse ground penetrating radar," *5th IEEE Sensor Array and Multichannel Signal Processing Workshop,SAM 2008.*, pp. 225–228, 2008.

[55] Li Ting-jun, Kong Ling-jiang, and Zhou Zheng-ou, "Symmetry filtering method for gpr clutter reduction," *IEEE Proceedings of International Conference Millimeter and Microwave Technology, ICMMT 2008*, vol. 3, April 2008.

[56] Suncheol Park, Kangwook Kim, and Kwang Hee Ko, "Multiple landmine detection algorithm using ground penetrating radar," *IEEE Transactions of Geoscience and Remote Sensing Symposium (IGARSS)*, vol. 3, pp. 3190–3193, July 2012.

[57] L. Capineri, S. Ivashov, T. Bechtel, A. Zhuravlev, P. Falorni, C. Windsor, G. Borgioli, I. Vasiliev, and A. Sheyko, "Comparison of gpr sensor types for landmine detection and classification," *12th International Conference on Ground Penetrating Radar*, vol. 55, pp. 557–563, June 2008.

[58] David J. Daniels, "Gpr for landmine detection, an invited review paper," *Proceedings of the tenth international conference on Ground Penetrating Radar*, pp. 7–10, June 2004.

[59] David J. Daniels, *Detection of Concealed Targets*, John Wiley & Sons, Inc Hoboken, New Jersey,, first edition, 2010.

[60] Steve Cardimona, "Subsurface investigation using ground penetration radar," *Proceeding of 2nd Annual Conference on the Application of Geophysical and NDT Methodologies to Transportation Facilities and Infrastructure*, July 2002.

[61] GSSI, "Terrasirch sir system-3000 users manual," *Geophysical Survey Systems, Inc.*, 2003.

[62] William H. Hyat and Jr. John A. Buck, *Engineering Electromagnetics*, McGraw Hill series in Electrical and Computer Engineering, sixth edition, January 2010.

[63] Rajeev Bansal, *Handbook of Engineering Electromagnetics*, Marcel Dekker, Inc., New York, USA, first edition, 2004.

[64] Rajeev Bansal, *Fundamentals of Engineering Electromagnetics*, Taylor & Francis Group, LLC, USA, first edition, 2006.

[65] Mattew N.O. Sadiku, *Elements of Electromagnetics*, Oxford University Press, fifth edition, January 2009.

[66] Sophocles J. Orfanidis, *Electromagnetic Waves and Antennas*, Rutgers University, New Jersey, USA, first edition, August 2010.

[67] Henri Benisty, Vincent Berger, and Jean-Michael Lourtioz, *Photonic Crystals: Towards Nanoscale photonic Devices*, Springer Science and Business Media, verlag Berlin Heidelberg, second edition, May 2008.

[68] Kazunori Takahashi, Holger Preetz, and Jan Igel, "Soil properties and performance of landmine detection by metal detector and ground-penetrating radarsoil characterization and its verification by afield test," *Journal of Applied Geophysics*, vol. 73, pp. 368–377, February 2011.

[69] Gary R. Olhoeft, "Electromagnetic field and material properties in ground penetration radar," *Proceedings of the second International Workshop on Advanced GPR*, pp. 144–147, May 2003.

[70] Wu Renbiao, Cao Yunqian, and Liu Jiaxue, "Multilayered diffraction tomography algorithm for ground penetrating radar," *IEEE 10th International Conference on Signal Processing (ICSP)*, pp. 2129–2132, October 2010.

[71] Vera Behar and Christo Kabakchiev, "A simple algorithm for simulation of stepped-frequency gpr images of multi-layered media," *Progress In Electromagnetics Research Symposium, Hangzhou, China*, pp. 1–4, 2008.

[72] Maurice Weiner, *Electromagnetic Analysis Using Transmission Line Variables*, World Scientific Publishing Co. Ltd, first edition, Singapore, 2001.

[73] Peter Torrione and Leslie Collins, "Statistical models for ground penetrating radar: Applications to synthetic data generation and statistical pre-screening," *IEEE conference on Geoscience and Remote Sensing Symposium, IGARSS 2008*, vol. 2, pp. 367–370, 1999.

[74] Jenneke Bakker, Jan van der Kruk, Jutta Bikowski, and Harry Vereecken, "Two-layer inversion of dispersive gpr data due to freezing induced waveguides a synthetic study," *6th International Workshop on Advanced Ground Penetrating Radar (IWAGPR), 2011*, 2011.

[75] Janet E. Simms, Dwain K. Butler, and Michael H. Powers, "Full waveform inverse modeling of ground penetrating radar data: An initial approach," *Discretionary Research Program U.S Army Engineer Waterways Experiment Station*, pp. 1–138, September 1995.

[76] M.A. Jusoh, Z. Abbas, J. Hassan, B.Z. Azmi, and A.F. Ahmad, "A simple procedure to determine complex permittivity of moist materials using standard commercial coaxial sensor," *Measurement Science Review*, vol. 11, no. 1, pp. 19–22, 2011.

[77] Helmi Zulhaidi Mohd Shafri, RSA Raja Abdullah, Mardeni Roslee, and Ratnasamy Muniandy, "Optimization of ground penetrating radar (gpr) mixture model in road pavement density data analysis," *Geoscience and Remote Sensing Symposium, IEEE International*, vol. 3, pp. 1326–1329, 2008.

[78] Grit Dannowski and Ugur Yaramanci, "Estimation of water content and porosity using combined radar and geoelectrical measurements," *European Journal of Environmental and Engineering Geophysics*, vol. 4, pp. 1–15, July 1999.

[79] M.A. Jusoh, Z. Abbas, J. Hassan, B.Z. Azmi, and A.F. Ahmad, "A simple procedure to determine complex permittivity of moist materials using standard commercial coaxial sensor," *Measurement Science review*, vol. 11, no. 1, pp. 19–23, 2011.

[80] S. Valle, L. Zanzi, and G. Lenzi, "2d and 3d focusing of ground penetrating radar data for ndt," *Proceedings of the Eighth International Conference on Ground Penetrating Radar (GPR 2000)*, pp. 157–162, May 2000.

[81] Sébastien Lambot, Evert C. Slob, Idesbald van den Bosch, Benoit Stockbroeckx, and Marnik Vanclooster, "Modeling of ground-penetrating radar for accurate characterization of subsurface electric properties," *IEEE Transactions on Geoscience and Remote Sensing*, vol. 42, no. 11, pp. 163–169, November 2004.

[82] Sébastien Lambot, Lutz Weihermüller, Johan A. Huisman, Harry Vereecken, Marnik Vanclooster, and Evert C. Slob, "Analysis of air-launched ground-penetrating radar techniques to measure the soil surface water content," *Water Resources Research, W11403*, vol. 42, pp. 1–12, November 2006.

[83] Bradley M. Battista, Adrian D. Addison, and Camelia C. Knapp, "Empirical mode decomposition operator for dewowing gpr data," *Journal of Environmental and Engineering Geophysics (JEEG)*, vol. 14, no. 7, pp. 163–169, December 2009.

[84] Sébastien Lambot, Evert. C. Slob, I. van den Boch, B. Stockbroeckx, B. Sheers, and M. Vanclooster, "Gpr design and modeling for identifying the shallow subsurface dielectric properties," *2nd Intemtwnal Workshop on Advanced GPR*, pp. 130–133, May 2003.

[85] Merrill I. Skolink, *Introduction to radar systems*, McGraw-Hill Higher Education, third edition, 2001.

[86] Gebremichael T. Tesfamariam and Dilip S. Mali, "Gpr technologies for landmine detection," *TECHNIA International Journal of Computing Science and Communication Technologies*, vol. 5, no. 1, pp. 768–774, July 2012.

[87] Pramod K. Varshney, *Distributed Detection and Data Fusion*, Springer Verlag, New York. Ink, USA, first edition, 1997.

[88] Pramod K. Varshney, "Multisensor data fusion," *Electronics and Communication Engineering Journal*, pp. 245–253, December 1997.

[89] Stelios C.A. Thomopoulos, "Sensor selectivity and intelligent data fusion," *IEEE Proceedings of International Conference on Multisensor Fusion and Integration for Intelligent Systems (MFI'94)*, pp. 530–537, 1994.

[90] Maged Mikhail, Saleh Zein-Sabatto, and Mohammad Bodruzzaman, "Decision fusion methodologies in structural health monitoring system," *Southeastcon,2012 IEEE Transactions*, pp. –, 2012.

[91] John G.M. Schavemaker, Eric den Breejen, Frank Cremer, Klamer Schutte, and Koen W. Benoist, "Depth fusion for anti-personnel landmine detection," *Proc. SPIE on Det. and Rem. Techn. for Mines and Minelike Targets VI*, vol. 4394, pp. 1–11, April 2001.

[92] Ashok Sundaresan, Pramod K. Varshney, and Negeswara S.V. rao, "Copula based fusion of correlated decisions," *IEEE Transactions on Aerospace and Electronic Systems*, vol. 47, no. 1, pp. 454–460, 2011.

[93] Z. Chair and Varshney P.K., "Optimal data fusion in multiple sensor detection systems," *IEEE Transactions on Aerospace and Electronic Systems*, vol. 22, no. 1, pp. 98–101, January 1986.

[94] V. Aalo and R. Viswanathan, "Evaluation of five discriminant procedures for binary variables," *IEEE Transactions on Aerospace and Electronic Systems*, vol. 25, no. 3, pp. 414–421, 1989.

[95] Jian-Guo Chen and Nirwan Ansari, "Optimum multisensor fusion of correlated local decisions," *IEEE Transactions On System Man and Cybernetics-Part C: Application and Reviews*, vol. 28, no. 2, pp. 276–281, May 1998.

[96] Ashraf Aziz, "A soft decision fusion approach for multiple sensor distributed binary detection system," *IEEE Transactions on Aerospace and Electronic Systems*, vol. 47, no. 3, pp. 2308–2315, July 2011.

[97] Moshe Kam, Qianc Zhu, and W. Steven Gray, "Optimal data fusion of correlated local decisions in multiple sensor detection systems," *IEEE Transactions on Aerospace and Electronic Systems*, vol. 28, no. 3, pp. 916–920, July 1992.

[98] E. Darkopoulos and C.C. Lee, "Optimum multisensor fusion of correlated local decisions," *IEEE Transactions on Aerospace and Electronic Systems*, vol. 27, no. 4, pp. 593–606, July 1991.

[99] Dan H. Moore, "Evaluation of five discriminant procedures for binary variables," *Journal of American Statistics Association, Theory and methods section*, vol. 68, no. 342, pp. 916–920, July 1973.

[100] Kalyan Veeramachaneni, Lisa Osadciw, Arun Ross, and Nisha Srinivas, "Decision-level fusion strategies for correlated biometric classifiers," *IEEE Computer Society Conference on Computer Vision and Pattern Recognition Workshops, CVPRW '08.*, pp. 1–6, 2008.

[101] Qi Cheng, Pramod K. Varshney, James H. Michels, and Celeste M. Belcastro, "Distributed fault detection with correlated decision fusion," *IEEE Transactions on Aerospace and Electronic Systems*, vol. 45, no. 4, pp. 1448–1465, October 2009.

[102] Chow C. and Liu C., "Approximating discrete probability distributions with dependence trees," *IEEE Transactions on Information Theory, IT*, vol. 14, no. 3, pp. 462–467, 1968.

[103] Guanrong Chen and Trung Tat Pham, *Introduction to Fuzzy Sets, Fuzzy Logic and Fuzzy Control Systems*, CRC Press LLC, Unites States of America, 2001.

[104] Anna Loskiewicz-Buczak and Robert E. Uhrig, "Decision fusion by fuzzy set operation," *Proceedings of the IEEE World Congress on Computational Intelligence*, vol. 2, pp. 1412–1417, June 1994.

Curriculum vitae

Name:	Gebremichael Te-ame
Date of birth:	08.02.1978
Place of birth:	Enticho, Ethiopia
Family status:	Married
Nationality:	Ethiopian

Education

02/2010 – 07/2013	Technische Universität Darmstadt, Germany Information and Communication Engineering (Ph.D)
09/2002 – 06/2005	Addis Ababa University, Ethiopia Faculty of Technology (M.Sc.)
09/1996 – 07/2001	Addis Ababa University, Ethiopia Faculty of Technology, Electrical & Computer Engineering (B.Sc.)
09/1991 – 07/1996	Nigist Saba Comprehensive Secondary School Adwa, Ethiopia (Diploma)

Work experience

11/2001 –	Mekelle University, Electrical and Computer Engineering, Ethiopia Worked as Graduate Assistant II, Lecturer and Assistant Professor